

APPLIED
COMPUTATIONAL
ELECTROMAGNETICS
SOCIETY
JOURNAL

July 1996
Vol. 11 No. 2

ISSN 1054-4887

DISTRIBUTION STATEMENT A

Approved for public release:
Distribution Unlimited

DTIC QUALITY INSPECTED 1

GENERAL PURPOSE AND SCOPE. The Applied Computational Electromagnetics Society Journal hereinafter known as the **ACES Journal** is devoted to the exchange of information in computational electromagnetics, to the advancement of the state-of-the-art, and to the promotion of related technical activities. A primary objective of the information exchange is the elimination of the need to "re-invent the wheel" to solve a previously-solved computational problem in electrical engineering, physics, or related fields of study. The technical activities promoted by this publication include code validation, performance analysis, and input/output standardization; code or technique optimization and error minimization; innovations in solution technique or in data input/output; identification of new applications for electromagnetics modeling codes and techniques; integration of computational electromagnetics techniques with new computer architectures; and correlation of computational parameters with physical mechanisms.

SUBMISSIONS CONTENT. The **ACES Journal** welcomes original, previously unpublished papers, relating to **applied computational electromagnetics**.

Typical papers will represent the computational electromagnetics aspects of research in electrical engineering, physics, or related disciplines. However, papers which represent research in **applied computational electromagnetics** itself are equally acceptable.

For additional details, see "Information for Authors" on the back cover.

SUBSCRIPTIONS. All members of the Applied Computational Electromagnetics Society (**ACES**) who have paid their subscription fees are entitled to receive the **ACES Journal** with a minimum of three issues per calendar year. See page 100 for ACES membership and Newsletter and Journal Subscription form.

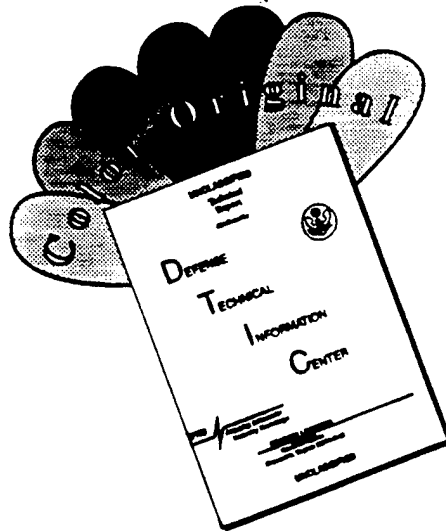
Back issues, when available, are \$15.00 each. Subscriptions to **ACES**, orders for back issues of the **ACES Journal** and changes of addresses should be sent to:

Dr. Richard Adler
ACES Executive Officer
ECE Department, Code ECAB
Naval Postgraduate School
833 Dyer Road, Room 437
Monterey, CA 93943-5121 USA

Allow four week's advance notice for change of address. Claims for missing issues will not be honored because of insufficient notice or address change or loss in mail unless the secretary is notified within 60 days for USA and Canadian subscribers or 90 days for subscribers in other countries, from the last day of the month of publication. For information regarding reprints of individual papers or other materials, see "Information for Authors".

LIABILITY. Neither ACES or the **ACES Journal** editors are responsible for any consequence of misinformation or claims, express or implied, in any published material in an **ACES Journal** issue. This also applies to advertising, for which only camera-ready copies are accepted. Authors are responsible for information contained in their papers. If any material submitted for publication includes material which has already been published elsewhere, it is the author's responsibility to obtain written permission to reproduce such material.

DISCLAIMER NOTICE



THIS DOCUMENT IS BEST QUALITY AVAILABLE. THE COPY FURNISHED TO DTIC CONTAINED A SIGNIFICANT NUMBER OF COLOR PAGES WHICH DO NOT REPRODUCE LEGIBLY ON BLACK AND WHITE MICROFICHE.

APPLIED
COMPUTATIONAL
ELECTROMAGNETICS
SOCIETY
Journal

July 1996
Vol. 11 No. 2

ISSN 1054-4887

The ACES Journal is abstracted in INSPEC, in Engineering Index, and in DTIC.

The second, third, fourth, and fifth illustrations on the front cover have been obtained from Lawrence Livermore National laboratory.

The first illustration on the front cover has been obtained from FLUX2D software, CEDRAT S.S. France, MAGSOFT Corporation, New York.

19960807 060

THE APPLIED COMPUTATIONAL ELECTROMAGNETICS SOCIETY

JOURNAL EDITORS

EDITOR-IN-CHIEF/ACES

W. Perry Wheless, Jr.
University of Alabama, EE Dept.
PO Box 870286
Tuscaloosa, AL 35487-0286 USA

ASSOC. EDITOR-IN-CHIEF/JOURNAL

Adalbert Konrad
University of Toronto
Toronto, ON, CANADA M5S 1A4

Brian A. Austin
University of Liverpool
Liverpool, UK

Fulvio Bessi
Ingegneria dei Sistemi S.p.A.
Pisa, ITALY

Robert Bevensee
Box 812
Alamo, CA, USA

John R. Bowler
University of Surrey
Surrey, UK

Robert T. Brown
Lockheed Aeronautical Sys. Co.
Valencia, CA, USA

Chalmers M. Butler
Clemson University
Clemson, SC, USA

Edgar Coffey
Advanced Electromagnetics
Albuquerque, NM, USA

Tony Fleming
Telecom Australia.
Clayton, Victoria, AUSTRALIA

Pat Foster
Microwave & Antenna Systems
Gt. Malvern, Worc. UK

Gregory R. Haack
DSTO
Salisbury, SA, AUSTRALIA

Christian Hafner
Swiss Federal Inst. of Technology
Zurich, SWITZERLAND

Roger Harrington
Syracuse University
Syracuse, NY, USA

Donald F. Herrick
ERIM
Ann Arbor, MI, USA

Kueichien C. Hill
Wright Laboratory
Wright-Patterson AFB, OH, USA

EDITOR-IN-CHIEF/JOURNAL

Duncan C. Baker
EE Dept. University of Pretoria
0002 Pretoria, SOUTH AFRICA

EDITOR-IN-CHIEF, EMERITUS

Robert M. Bevensee
Box 812
Alamo, CA, 94507-0516 USA

Todd H. Hubing
University of Missouri-Rolla
Rolla, MO, USA

Nathan Ida
University of Akron
Akron, OH, USA

Magdy F. Iskander
University of Utah
Salt Lake City, UT, USA

Kiyohiko Itoh
Hokkaido University
Sapporo, JAPAN

Randy J. Jost
SRI International
Arlington, VA, USA

Linda P.B. Katehi
University of Michigan
Ann Arbor, MI, USA

Peter Krylstedt
National Defence Research Est.
Sundbyberg, SWEDEN

Stanley Kubina
Concordia University
Montreal, Quebec, CANADA

Karl J. Langenberg
Universitat Kasse
Kassel, GERMANY

Ronald Marhefka
Ohio State University
Columbus, OH, USA

Gerald Meunier
NPG/ENSIEG
St. Martin-d'Heres Cedex, FRANCE

Edmund K. Miller
LASL
Santa Fe, NM, USA

Giorgio Molinari
University of Genova
Genova, ITALY

Kenzo Miya
University of Tokyo
Tokyo, JAPAN

MANAGING EDITOR

Richard W. Adler
833 Dyer Rd. Room 437
Naval Postgraduate School Code EC/AB
Monterey, CA 93943-5121 USA

EDITOR-IN-CHIEF, EMERITUS

David E. Stein
USAF Scientific Advisory Board
Washington, DC 20330 USA

Osama A. Mohammed
Florida International Univ.
Miami, FL, USA

Frederic A. Molinet
Societe Mothesim
Plessis-Robinson, FRANCE

Gerrit Mur
Technische Universiteit Delft
Delft, NETHERLANDS

Takayoshi Nakata
Okayama University
Okayama, JAPAN

Andrew F. Peterson
Georgia Institute of Technology
Atlanta, GA, USA

Harold A. Sabbagh
Sabbagh Associates
Bloomington, IN, USA

Chris Smith
Delfin Systems
Santa Clara, CA, USA

David E. Stein
USAF Scientific Advisory Board
Washington, DC, USA

C.W. "Bill" Trowbridge
Vector Fields Limited
Oxford, UK

Jean-Claude Verite
Electricite de France
Clamart, Cedex, FRANCE

John W. Williams
SAIC
Germantown, MD, USA

Frank Walker
Boeing Defence & Space Group
Houston, TX, USA

Keith W. Whites
University of Kentucky
Lexington, KY, USA

Manfred Wurm
FB Technik
Kiel, GERMANY

THE APPLIED COMPUTATIONAL ELECTROMAGNETICS SOCIETY

JOURNAL

TABLE OF CONTENTS

Vol. 11 No. 2

July 1996

"Analysis of the Finite Element Radiation Model Cone for Antenna Modeling" by M.C. Medina, C.A. Balanis, J. Peng, and P.A. Tirkas	4
"Accuracy of the Finite Element Method with Second Order Absorbing Boundary Conditions for the Solution of Aperture Radiation Problems" by J. Silvestro, X. Yuan and Z. Cendes	14
"The FEMAX Finite-Element Package for Computing Three-dimensional Electromagnetic Fields" by G. Mur	24
"A Moment Method Formulation for The Analysis of Wire Antennas Attached to Arbitrary Conducting Bodies Defined by Parametric Surfaces" by F. Rivas, L. Valle and M.F. Catedra	32
"A Posteriori Error Estimates for Two-Dimensional Electromagnetic Field Computations: Boundary Elements and Finite Elements" by F.J.C. Meyer and D.B. Davidson	40
"Modelling of an Arbitrarily-Oriented Mobile Telephone Handset in the Finite-Difference Time-Domain Field Computation Method" by P.S. Excell, P. Olley and N.N. Jackson	55
"A Magnetic Field Iterative Technique for Improving High Frequency Prediction Methods" by D.D. Reuster, G.A. Thiele, and P.W. Elloe	66
"Modeling of Remote Field Eddy Current Transient Phenomena" by M. Raugi and N. Ida	72
Letter From the Editor: Duncan Baker	76
Institutional Membership	77
Announcements:	
Copyright Form	79
Application for ACES Membership and Newsletter and Journal Subscription	81
Advertising Rates	82
Copy Information - Deadline for Submission of Articles	82

ANALYSIS OF THE FINITE ELEMENT RADIATION MODEL CODE FOR ANTENNA MODELING *

Marcos C. Medina, Constantine A. Balanis, Jian Peng and Panayiotis A. Tirkas
Department of Electrical Engineering
Telecommunications Research Center
Arizona State University
Tempe, Arizona 85287-7206

Abstract

The Finite Element Radiation Model (FERM) code is applied to examine radiation patterns and input impedance of various antenna configurations on complex helicopters. This paper addresses the strengths and weaknesses of the FERM code when applied in antenna analysis and is compared with other national codes, such as the Numerical Electromagnetics Code (NEC). In addition, guidelines are outlined for various applications of the code.

I. INTRODUCTION

The Finite Element Radiation Model (FERM) code is based on the Method of Moments and uses triangular surface patches to model the geometry. The triangular patches allow for enormous flexibility in modeling complex, curved three-dimensional geometries, such as helicopters. The basis functions used by the code are in accordance with the Rao *et al.* [1] basis functions. The FERM code was developed in 1987 at the MIT Lincoln Laboratory [2], and is a general purpose code with applications in radar cross section prediction and antenna modeling. A similar code is the Electromagnetic Surface Patch (ESP) code [3], which is based on

quadrilateral patches. Unlike the FERM and ESP codes, the NEC is based on a wire grid model of the geometry. The FERM, ESP and NEC codes have all been applied by the Advanced Helicopter Electromagnetics (AHE) consortium for analysis of antennas on helicopters. In this paper, helicopter antennas are analyzed using the FERM code.

II. CODE MODIFICATIONS

The FERM code is written in a modular structure, allowing it to be highly portable. The more computationally intensive portions of the code can therefore be transported to computers with larger memory. The modular form of the FERM code is a distinct advantage. The code was originally installed on a VAX 3100 workstation. The VAX workstation required too much time to simulate antenna radiation problems related to helicopter applications. In fact, if the number of unknowns reached 1800, the VAX was incapable of completing the computation due to memory limitations. The VAX did not have the memory needed for the segmentation of most geometries required; therefore, the code was transported to an IBM RISC/6000 350 workstation.

At first, the more computationally intensive programs were transported to the IBM RISC workstation. Since antenna radiation studies were the main areas of interest, the programs

*This work was supported by the Advanced Helicopter Electromagnetics (AHE) Program and NASA under Grant NAG-1-1082.

EFIE2, EFIE3, and EFIE4V were the first to be transferred. The program EFIE2 numerically evaluates the EFIE's for the desired geometry and creates the impedance or Z-matrix. The program EFIE3 implements *LU* decomposition to decompose the Z-matrix. EFIE4V solves for the current distribution using the decomposed Z-matrix and the voltage sources stored in the primary data file. The execution of EFIE1, EFIE5V, and EFIE5R remained on the VAX workstation. The program EFIE1 converts the user geometry directives into an internal format for the numerical processing accomplished via EFIE2, EFIE3, and EFIE4V. Eventually, EFIE1 was migrated to the IBM RISC to avoid the problems associated with transferring data from VMS system to a UNIX system. EFIE5V and EFIE5R interface with the graphics package DISSPLA. Since DISSPLA is licensed strictly to the VAX workstation, these two routines must be executed on the VAX. These last two programs output the antenna radiation patterns.

The routines EFIE2, EFIE3, and EFIE4V required minor modifications for execution on the IBM RISC. They consisted of disengaging the subroutine used to calculate the CPU time, modifying the OPEN directives for temporary data files, and altering the format of the data files created by the FERM code. The IBM RISC is capable of listing the real-time and CPU time used during the execution of a program. Therefore, the subroutine CLOCK0, used to determine the execution time of a program on a VAX workstation, was eliminated.

All calls to temporary or scratch files were modified. VAX/VMS Fortran requires that when a SCRATCH file is created or opened the initial size of the file must be specified using the INITIALSIZE specifier [4]. Otherwise, no memory allocation is made. VS Fortran does not recognize the specifier INITIALSIZE and it was deleted from the OPEN statement for use on the IBM RISC [5].

The internally-formatted data files created by the FERM are unformatted and are not readable text files. These files cannot traverse the platform from a VAX workstation to an IBM

workstation. Data was lost during the use of the File Transfer Protocol (FTP) to transport the data from EFIE4V (IBM workstation) to EFIE5R (VAX workstation). To circumvent this problem, the data files written to and read from (STORAGE, RESMAT, and RESULT) by the subprograms had to be formatted and required commas between each piece of data to ensure no data was lost. This involved rewriting all the format statements in EFIE1, EFIE2, EFIE3, and EFIE4V, as well as the subroutines used in these programs such as MISC and EFIE.

DRAW, a graphics package developed at Arizona State University to prepare rectangular and polar plots of radiation patterns, has replaced DISSPLA. DISSPLA is licensed strictly for execution on the VAX 3100 workstation. DRAW is executed on a UNIX workstation. In addition to the ease of interface with the FERM code on the IBM RISC, DRAW produces higher quality rectangular and polar plots than DISSPLA. DISSPLA was also used for the initial viewing of aircraft geometry. On a UNIX based workstation this is now done using GEOMVIEW [9], which is available via an anonymous ftp site.

In addition to eliminating DISSPLA from use as a graphics package, the Pattern Analysis and Database (PAD) was dismantled. PAD is not user-friendly. It is capable of organizing and manipulating data and storing numerous radiation patterns; however, for antenna radiation prediction, all that is needed is the computation and storage of radiation patterns. PAD was replaced by PLOTR, a subroutine created specifically to process radiation pattern computations. PLOTR uses the SPATTERN output data file created by EFIE5R and calculates normalized or absolute antenna gain.

III. GEOM INTERFACE

Super 3D [6] is a popular interactive graphics package capable of constructing solid surface helicopter models. This can be done by employing either a mouse or an input data file. The geometry can be rotated or scaled, thus allow-

ing modifications to be accomplished easily and accurately. Such a graphics package is important in the analysis and design of antennas on helicopters. Super 3D is used for constructing the helicopter geometry and attaching the various antennas to the fuselage. The solid surface geometry is then exported in ASCII format. GEOM, a geometry interface between the Super 3D and the electromagnetics codes, translates the solid surface model to either a wire grid model for NEC or surface patch model for ESP [7], [8].

The GEOM program was originally constructed to allow interaction between the NEC and ESP codes and the Super 3D. However, with the increasing use of the FERM code, by the AHE consortium, for antenna radiation pattern predictions and input impedance studies of HF antennas, a link between the FERM and Super 3D was also necessary. A subroutine, to convert geometry files from the Super 3D format to the FERM format, was also incorporated into the existing GEOM program.

The ESP code is a surface patch code, similar to the FERM. However, the method it employs in modeling geometries is much different. The ESP creates a surface by piecing together three-dimensional patches. Meanwhile, the FERM uses a series of lines to create a two-dimensional polygon representing a cross-section of the geometry. This two-dimensional polygon is then expanded along the third dimension to join with another cross-sectional polygon. The circumference of the polygon may also be scaled as it is stretched to form conical shaped structures. The FERM generates the triangular patches via the combination of the segmentation used between two polygons and the segmentation used for the lines of the polygon.

The FERM's method of constructing geometries is very efficient for rectangular, cylindrical, and spherical structures, but diminishes as the geometries become more irregular in shape. This allows the FERM to be highly suited for modeling aircraft fuselages, but lacking in the construction of the stabilizers and wings.

This modeling technique also eases the burdens encountered during segmentation. As

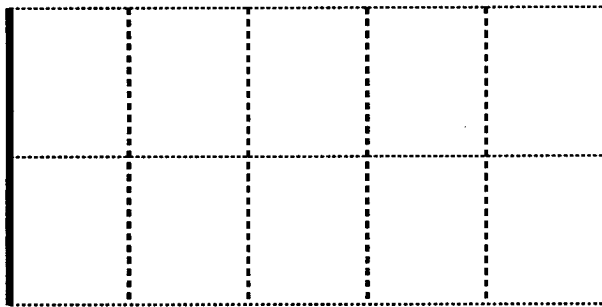
mentioned before, when the FERM segments a surface, it relies upon the number of segments per line comprising the cross-sectional polygon and the number of sections between the polygons. Therefore, the number of patches in one local area can be increased without affecting the segmentation at other areas. For example, the number of patches along the section of the fuselage where the antenna is attached may be increased while the segmentation along nose and tail of the aircraft remains unaffected.

During the conversion of a Super 3D geometry file to a FERM format, sufficient cross-sections of the geometry must be taken to ensure that every contour of the surface is closely followed. The Super 3D cross-section coordinates are read into the FERM and used to construct the lines of the polygon. The number of segments per line is input by the user. After a cross-sectional polygon is built, it is joined to the previous one to build the fuselage. However, care must be taken when joining two polygons. The number of segments per line in a polygon must be identical for two polygons to be attached. Because of this, it was decided that the segmentation of each line, supplied by the user, remain constant throughout the FERM data file. The number of segments per line of a cross-sectional polygon determines the total segmentation around the circumference of the fuselage. Likewise, the total number of sections used between each polygon determines the total segmentation of the fuselage length. If an increase in the segmentation of one area is desired, the number of segments per line in that local area may be easily modified by the user to suit the application.

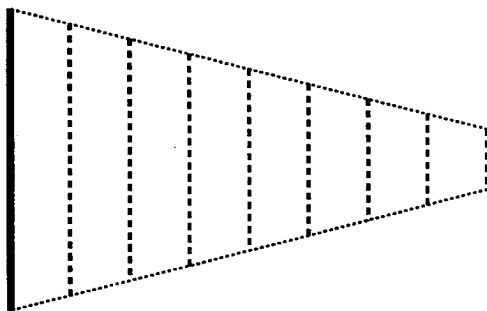
The stabilizers and wings of an aircraft are easily modeled with the ESP; they are simply two-dimensional plates. However, the FERM is mostly suited toward three-dimensional applications. The wings and stabilizers are much more difficult to model than the fuselage. The FERM generates plates in three ways. If the PLATE directive is employed, only two lines with a common end point are needed. The FERM then creates a plate by generating two lines of the same length as the original two lines and plac-

ing them parallel. Thus, the PLATE command is limited to generating squares or rhomboids. If a plate has more than four sides, or has two opposite sides that are not parallel, then this directive cannot be used.

Implementing the TRIA directive rather than the PLATE directive provides a more flexible method. The TRIA (short for triangle) command also requires two lines with a common end point, but generates a triangle rather than a rhombus. Moreover, any two-dimensional plate can be constructed from a collage of triangular patches. Therefore, this method provides the most flexibility in generating arbitrary shapes with minimal difficulty.



(a)



(b)

Figure 1: The use of the PRISM directive to produce (a) a rectangular plate and (b) a tapered wing.

Another technique employed by the FERM to build two-dimensional plates follows along the same lines as the construction of the three-dimensional surfaces. However, it is limited to

working on plates with four sides where at least one pair of opposite sides are parallel. The PRISM directive takes a polygon and deposits copies of it at specified intervals along the direction toward the desired ending point. A line may be redefined as a polygon and used to generate a rectangular plate. In addition, the line's length may be scaled as it is moved from interval to interval so as to make tapered plates. Figure 1(a) exhibits the use of the PRISM command for generating a rectangular plate. The original line, represented by the solid line, is separated into two segments to provide a width of two segments. The dashed lines represent the copies of the original line placed so that they divide the length of the plate into six sections. While the segmentation along the width of the plate is determined by the segmentation of the original line, the segmentation along the length is accomplished via a numerical argument in the PRISM command. The dotted lines represent the two other sides of the plate created by implementing PRISM. In Figure 1(b) a model of a wing is depicted. This structure was also created using the PRISM directive, but the length of the original line was scaled by a value less than unity to produce a narrowing width at each section and yield a tapered shape.

The Super 3D format does not differentiate between patches used for wings or patches used for the fuselage. However, the GEOM subroutine must decide whether the set of data it is given represents a cross-sectional polygon or a two-dimensional plate. If it is a cross-sectional polygon, the lines must be segmented, the polygon must be built and joined to the previous polygon, if one exists. If a two-dimensional plate must be constructed, then the lines building the plate must be segmented and the plate divided into as many triangles as needed to cover the surface area. To differentiate between a cross-sectional polygon and a two-dimensional plate, the Super 3D data file must be modified. The lines of data representing the two-dimensional plate must use a "plate" directive rather than the "polygon" directive normally used. This alteration is a necessity for the GEOM subroutine to perform correctly. If a

line is encountered, separate from other lines or polygons, then it is modeled as a wire monopole antenna.

The completion of the GEOM subroutine to transfer Super 3D data files to FERM data file marks a milestone. Now the identical geometry analyzed by the NEC and ESP can be studied with the FERM without inaccuracies resulting from the reconstruction of the structure.

IV. RESULTS

A. PATTERN PREDICTION

Figures 2 and 3 illustrate the geometry and overall dimensions of the Blackhawk helicopter, and the FERM model used in this analysis, respectively. A loop or towel-bar antenna is mounted beneath the tail of the Blackhawk helicopter. The loop had a length of 3.97 meters and a height of 0.4 meters. Because a strip antenna was implemented, a width of 4.0 cm, equivalent to a wire radius of 1.0 cm, was used [10]. The loop consists of only three strips with the metallic body of the helicopter comprising the fourth side. The antenna is fed along the strip closest to the front of the helicopter.

There are two problems associated with the FERM code in modeling wire loop antennas such as the one illustrated in Figure 3. The first is that two wires must be collinear or connected end-to-end. In generating a loop antenna, the wires cannot be placed end-to-end at the 90° bends. The second problem is that wires cannot be electrically attached to surfaces in the current version of the FERM code. To solve the first problem, the loop is created using a strip equivalent model. The strip can be electrically connected at right angles while the wires cannot. Figure 4 exhibits the differences between the wire and strip models at the corner of the loop antenna. The strip can also be electrically attached to the helicopter fuselage if there are two common nodes between the strip mesh and the fuselage mesh. This was not possible to do for the loop antenna which was modeled as a strip due to the changing size of the helicopter tail, and so the edges of the strip are just placed

near the surface of the helicopter fuselage. This is not expected to influence much the computation of the antenna radiation patterns.

Figure 5 displays the radiation patterns of the loop antenna mounted on the Blackhawk helicopter at 10 MHz. FERM and NEC computed radiation patterns for the co-polarized yaw plane are compared. The patterns obtained by the two codes were normalized to 0 dB based on their individual maxima. The FERM exhibits a magnitude approximately 2 dB greater than that of the NEC around the $\phi = 90^\circ$ and $\phi = 270^\circ$. However, the results from the two codes agree well in the remaining portions of the pattern. In Figure 6, the co-polarized pitch plane radiation patterns are shown. Unlike the yaw plane, the agreement between the NEC and FERM in the pitch plane is not as good. The co-polarized roll plane is shown in Figure 7. The best agreement between the two codes is seen in this plane.

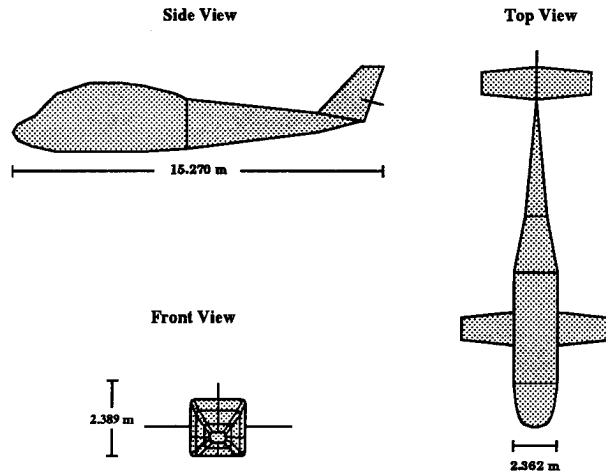


Figure 2: Geometry of the Blackhawk helicopter.

B. INPUT IMPEDANCE PREDICTION

For a strip antenna to be electrically connected to the helicopter fuselage or any other geometry, it must have a common edge with that geometry; i.e., a multiple edge between the strip antenna and the ground plane (or helicopter fuselage) must exist for the two to be electrically

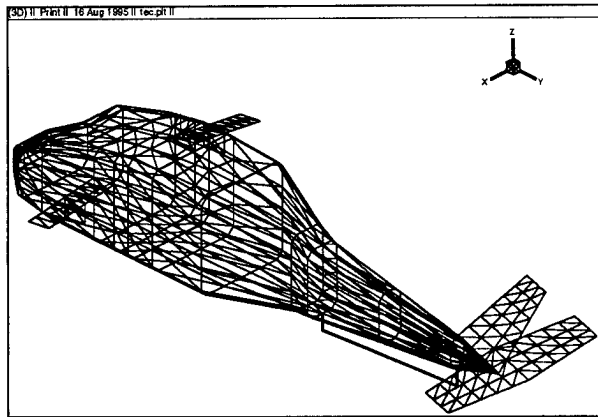


Figure 3: Geometry of the 4.0 m tow-bar antenna mounted on the segmented Blackhawk helicopter.

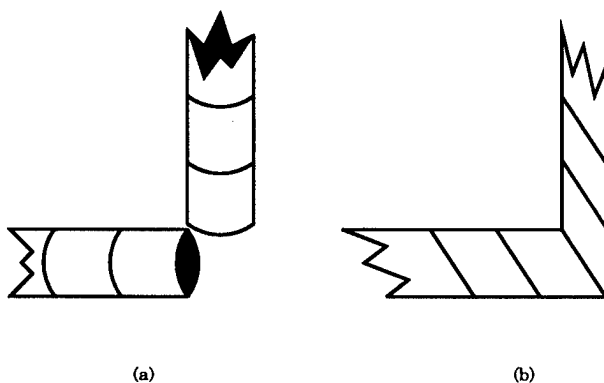


Figure 4: The modeling of a right angle of a loop antenna using (a) wires and (b) strips.

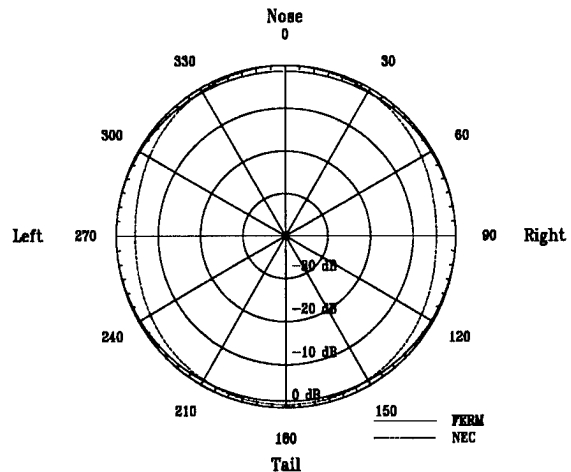


Figure 5: The co-polarized yaw plane radiation pattern of the loop antenna on the Blackhawk helicopter model at 10 MHz. There is no rotor blade structure.

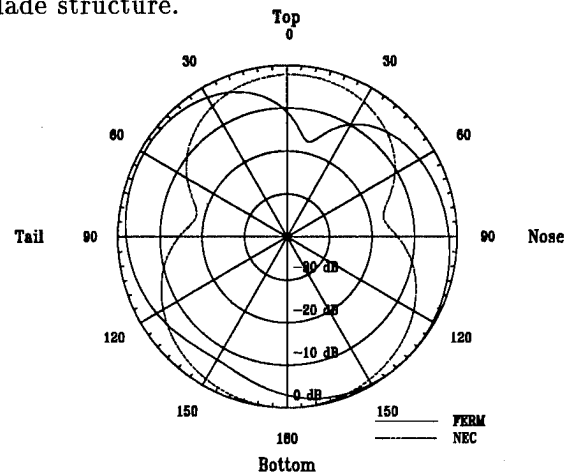


Figure 6: The co-polarized pitch plane radiation pattern of the loop antenna on the Blackhawk helicopter model at 10 MHz. There is no rotor blade structure.

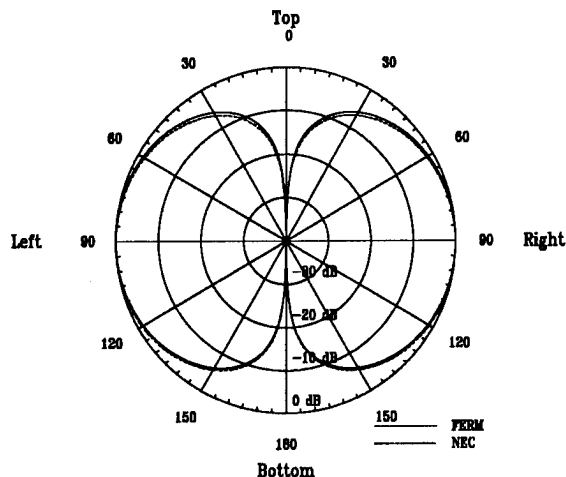


Figure 7: The co-polarized roll plane radiation pattern of the loop antenna on the Blackhawk helicopter model at 10 MHz. There is no rotor blade structure.

connected.

To illustrate how a strip antenna is properly connected to a ground, a simpler geometry is considered. The geometry is that of a $\lambda/4$ monopole on a $1 \times 1\lambda$ square ground plane at 100 MHz. Of interest in this problem is the calculation of the input impedance of the antenna. The geometry of the strip antenna and the way it is properly attached to the ground plate is illustrated in Figure 8. The thickness of the strip was chosen four times the wire radius ($w=20$ mm). To connect the strip to the ground plate the two must have a common edge along a triangular patch. The strip in this case was oriented in the xz -plane, and therefore, the discretization of the plate in the x direction was made nonuniform. This was required because the grid size in the x -direction near the middle of the plate (where the strip is attached) must be equal to the width of the strip. This is illustrated in Figure 8.

Using the simple geometry of the monopole on a square ground plate the input impedance of the antenna was calculated in the frequency range from 10 to 100 MHz. The FERM computed input resistance is compared with similar predictions using the NEC code in Figure 9, and the antenna input reactance in Figure 10. The results of having the strip antenna on top of the

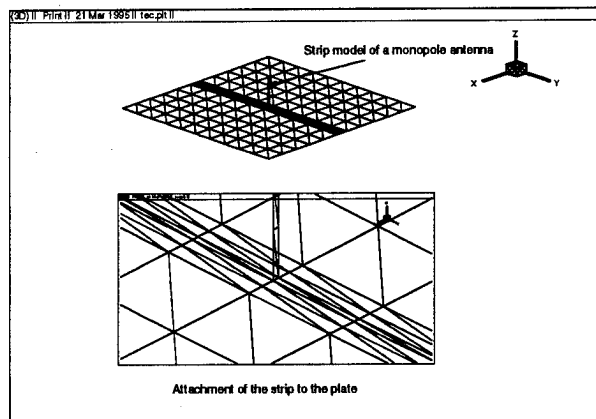


Figure 8: An example of a strip antenna connected to a ground plate for FERM modeling.

plate without being electrically connected to the plate are also included. As illustrated by both figures, there is only a few Ohms difference between the FERM predictions with the properly connected antenna and the NEC results.

It is expected that if the monopole antenna is properly attached to the helicopter fuselage then similar input impedance results will be obtained, especially at HF frequencies. It was previously demonstrated that the current distribution at HF frequencies is localized in the vicinity of the antenna, and that the platform used to mount the antenna is not expected to significantly affect the input impedance calculations [11].

C. EXECUTION TIMES OF THE FERM ON DIFFERENT COMPUTERS

A comparison of the execution times of the FERM code subroutines was accomplished to determine whether the IBM RISC 6000 is more efficient than the VAX 3100. Since the VAX 3100 workstation cannot handle the large scratch files generated for geometries with more than 1500 unknowns, the scope of the comparison was bounded by this upper limit. The four main numerical processing subroutines used in predicting antenna radiation patterns were considered: EFIE1, EFIE2, EFIE3, and EFIE4V. The results of this test are displayed in Table 1.

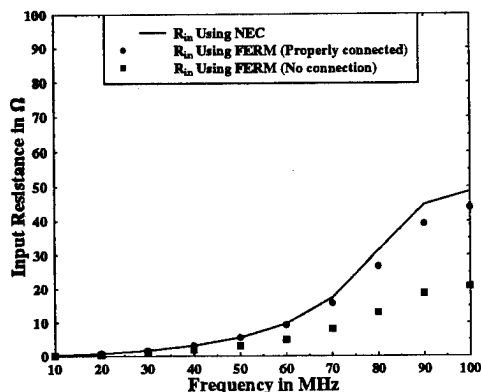


Figure 9: NEC and FERM computed input resistance of a strip antenna on a finite-size conducting ground plate, in the frequency range from 10 to 100 MHz.

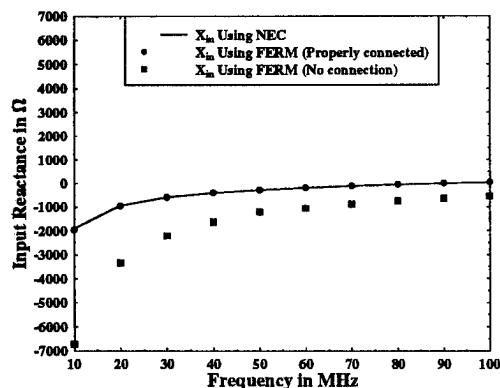


Figure 10: NEC and FERM computed input reactance of a strip antenna on a finite-size conducting ground plate, in the frequency range from 10 to 100 MHz.

Table 1: Execution times for FERM subroutines on various computers.

Comp. Type	No. of Unkn.	Execution Time (seconds)			
		EFIE1	EFIE2	EFIE3	EFIE4V
VAX	299	1.0	209.0	28.0	11.0
IBM	299	0.05	0.72	0.440	3.26
VAX	517	3.0	840.0	103.0	96.0
IBM	517	1.3	150.2	81.6	73.8
VAX	1201	10.0	4570	842	375
IBM	1201	4.7	1661.7	818.1	300.2

For the first two entries in the table, a $\lambda/4$ wire monopole located over a perfectly conducting ground plane was used for comparison. At the test frequency of 50 MHz, the physical length of the antenna was 1.5 meters while the sides of the ground plane were 6.0 meters in length. The diameter of the antenna was 1.5 cm. The gap between the antenna and the ground plane was matched to the diameter of the wire. The plate is segmented into 100 triangular pairs (ten segments per side). The wire antenna is divided into ten segments with the voltage excitation placed between the first and second antenna segments closest to the plate. This configuration spawned 299 unknowns.

There was little difference between execution times on the VAX and the IBM RISC for the first (EFIE1), third (EFIE3), and fourth (EFIE4V) subroutines. The VAX workstation produced results within 30 seconds of the IBM RISC for these subroutines. There was a substantial difference in run times for the second subroutine, EFIE2. This routine evaluates the electric field integral equation for the input geometry, creates an impedance matrix, and writes the matrix to a data file. This computation is of order N^2 , where N is the number of unknowns. The IBM RISC performed this task in under 1 second of CPU time, while the VAX required approximately 200 seconds of CPU time. Since the number of unknowns is relatively small, the amount of time needed to

write to and read from the scratch file TEMP is not significant. Therefore, the difference in execution times for the second subroutine can be attributed to the IBM RISC's more efficient numerical evaluation of the electric field integral equations.

A block helicopter modeled with a strip antenna, shown in Figure 11(b), provided the next set of unknowns for comparison. The test frequency for this geometry was established as 70 MHz. The block helicopter length (4.0 m) was partitioned into 10 segments. The $\lambda/4$ (1.07 m) antenna also had 10 segments with a 1.0 volt excitation located between the first and second segments closest to the fuselage. This geometry yielded 517 unknowns for processing on the two workstations.

This portion of the examination was very similar to the test runs with 299 unknowns. The VAX workstation had execution times 22-23 seconds slower than those of the IBM RISC for the EFIE3 and EFIE4V subroutines. EFIE2 took 5.6 times as long to execute on the VAX as it did on the IBM RISC. This case differed from the first in that EFIE2 had to use disk memory to complete the numerical evaluation on the VAX. This process slows the execution time substantially on the VAX. More on this subject will be seen as the number of unknowns increases towards the upper limit.

The final geometry used for this comparison was a modified version of the Blackhawk helicopter in Figure 3. The segmentation along the length of the helicopter was decreased as was the segmentation in the wings and stabilizers. This was done so that the number of unknowns would remain under 1500. This modified helicopter geometry produced 1201 unknowns.

As the number of unknowns was quadrupled from 299 to 1201, the difference in CPU times for the EFIE3 subroutine remained constant. EFIE3 is the subroutine that implements *LU* decomposition to decompose the impedance matrix created by the EFIE2 subroutine. Similarly, the differences in execution times for the EFIE1 and EFIE4V increased very slightly with the increase in the number of unknowns. The 5.3 second difference between the VAX's run

time and the IBM RISC's run time for the EFIE1 subroutine is insignificant. As the number of unknowns was increased from 517 to 1201, the execution time on the IBM RISC for the second subroutine increased by more than an order of magnitude. Meanwhile, the VAX's execution time for the same subroutine only increased by a factor of five. Clearly, for the case of 1201 unknowns, the difference in CPU time between VAX and IBM RISC increased, but their ratio is decreasing. This suggests that as the number of unknowns increases, the efficiency of the VAX workstation approaches that of the IBM RISC workstation. However, this conclusion cannot be completely verified because of the memory limitations on the VAX 3100 workstation. For geometries with less than 1200 unknowns, the IBM RISC 6000 is a better computer platform for execution of the FERM code because it operates more efficiently. Yet, for geometries with a larger number of unknowns, the IBM RISC 6000 is still better, because of the substantially larger amount of memory required by the temporary scratch files written during the numerical evaluation of the electric field integral equations in the subroutine EFIE2.

V. CONCLUSIONS

The Finite Element Radiation Model code is a Method of Moment solver used primarily for radar cross section prediction and antenna modeling. The code has been applied in this paper to predict the antenna radiation patterns of a loop mounted on the Blackhawk helicopter and the input impedance of a monopole antenna on a ground plate. The results have shown that when modeling a loop or towel-bar antenna with the FERM code, the antenna must be comprised of thin strips rather than wires. This ensures that the corners of the loop are connected both physically and electrically. The width of the strips was taken to be four times the equivalent radius of a wire with circular cross-section [10]. However, there are some difficulties in properly attaching the loop edges to the heli-

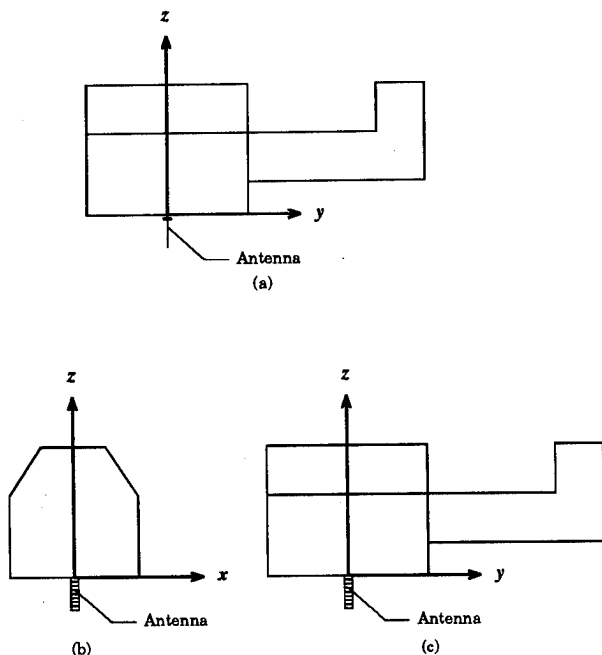


Figure 11: Antenna geometries on the block helicopter model: (a) wire antenna, (b) strip antenna with the width along the x-axis, and (c) strip antenna with the width along the y-axis.

copter surface due to the complexity of the finite element mesh. To alleviate this problem the loop antenna was placed near the helicopter surface. The radiation patterns resulting from this analysis were compared with similar ones obtained using the NEC code. For antenna input impedance calculations a simpler structure was considered, that of a monopole on a ground plate. It is demonstrated that accurate input impedance results can be obtained when the antenna is properly grounded on the plate.

References

- [1] S.M. Rao, D.R. Wilton, and A.W. Glisson, "Electromagnetic scattering by surfaces of arbitrary shape," *IEEE Trans. Antennas Propag.*, AP-30, 409-418, May 1982.
- [2] S. Lee, D.A. Shnidman, and F.A. Lichauco, *Numerical Modeling of RCS and Antenna Problems*, Tech. Report 785, MIT Lincoln Laboratory, Lexington, Massachusetts, Dec. 1987.
- [3] E.H. Newman, *A User's Manual for Electromagnetic Surface Patch Code: ESP Version 4*, The Ohio State University, ElectroScience Lab., Rep. No. 716199-11, Aug. 1988.
- [4] *Guide to Programming on VAX/VMS (FORTRAN edition)*, Fourth Edition, Digital Equipment Corp., Maynard, MA, Sept. 1984.
- [5] *VS FORTRAN Version 2: Language and library Reference*, Third Edition, IBM Corp., San Jose, CA, June 1987.
- [6] Super 3D, copyrighted by Silicon Beach Software, 1986.
- [7] J. Peng, J. Choi, and C.A. Balanis, "Automation of the geometry data for the NEC and ESP using Super 3D," *Proc. 6th Annual Progress Review Appl. Comp. Electromag.*, pp.33-38, Mar. 1990.
- [8] J. Peng, *Guidelines and Automation of Antenna Patterns of Complex Structures*, M.S. Thesis, Arizona State University, Aug. 1992.
- [9] GEOMVIEW, copyrighted by the Geometry Center, University of Minnesota, 1994.
- [10] C.A. Balanis, *Antenna Theory: Analysis and Design*. New York, New York: Harper and Row, 1982.
- [11] W. Andrew, C.A. Balanis, C. Birtcher, P.A. Tirkas, "Finite-difference time domain of HF antennas," *1994 IEEE MIL-COM Conf. Rec.* (Ft. Monmouth, NJ), pp. 7-11, Oct. 1994.

Accuracy of the Finite Element Method with Second Order Absorbing Boundary Conditions for the Solution of Aperture Radiation Problems

John Silvestro, Xingchao Yuan¹ and Zoltan Cendes
Ansoft Corporation
Four Station Square, Suite 660
Pittsburgh, PA 15219

Abstract

The Finite Element Method with second order Absorbing Boundary Condition is a recently developed computational technique that finds use in antenna design and Electromagnetic Compatibility simulation. To determine the accuracy of this new procedure, the problem of aperture radiation was studied. The near zone and aperture fields of a waveguide antenna computed using the Finite Element Method are compared with published data and results found using other simulation techniques. These comparisons show that the new method is accurate even when the ABC boundary conforms to the problem geometry and is placed as near as $\lambda/2\pi$ to the aperture.

Introduction

A central problem in antenna design and Electromagnetic Compatibility (EMC) is computing the radiation from apertures. Apertures represent the key element in many radiating structures including open ended waveguides, flared horns and reflector antennas. In EMC, openings in system cabinets provide a major source of unwanted radiation. This latter application has become increasingly important as the European Economic Community and the FCC tighten their EMC compliance regulations.

Aperture problems have been studied in the past [1 and 2]. Typically the Method of Moments (MOM) is used to solve for the fields in the aperture assuming that the aperture is cut in an infinite ground plane. While this provides an efficient method of solution, the infinite ground plane assumption limits its utility. The resulting model is appropriate for analyzing an array of aperture antennas, but not

for computing the radiation from finite sized enclosures. Real world systems are finite in size and often have irregular openings and other objects, both metal and dielectric, that affect the radiation. For such problems a hybrid approach can be used [3 and 4]. Unfortunately these methods are only appropriate for the specific geometries considered. To solve more general problems, a general purpose computer simulation tool is needed.

A technique that can easily handle complex geometries and provides a general purpose simulation procedure is the Finite Element Method (FEM). The FEM has been used successfully in the past to model closed region problems. In the FEM, the solution space is broken into small elements and the field in each element is calculated directly. The resulting discretization is usually referred to as the finite element mesh. For open region radiation problems, the solution space must be bounded. One way to accomplish this is to place a 377Ω impedance boundary far from the radiating source. However, this approach generates a very large solution region and requires correspondingly large solution times. Recently a new Absorbing Boundary Condition (ABC) has been developed [5 and 10] that can be used to terminate the FEM mesh at boundaries very close to the radiating structure. The smaller solution region with this new absorbing boundary makes the resulting computation more efficient. However, the following question arises: How close can the new ABC be placed to the radiating structure without significant loss of accuracy? To answer this question, a study was undertaken to compare the results from FEM simulations with measured data available from the literature and with data found by using other solution techniques.

While the radiation from an opening in a system cabinet is an important problem, the

¹ Xingchao Yuan is currently employed at Cadence Design Systems, Inc., Chelmsford, MA 01824.

available data is limited. Therefore, the radiation from a waveguide antenna was chosen as the test case for this study. Using a waveguide antenna, it will be shown that this new ABC can be made to conform to the problem geometry and can be placed as close as $\lambda/2\pi$ from the aperture for such geometries. Placing the ABC this close to the radiating source keeps the FEM mesh small and results in an efficient solution.

Accuracy Statement

For the case presented here where the ABC is at $\lambda/2\pi$ the magnitude of the near zone electric field along the aperture center line is accurate to within ± 0.5 dB when compared to measured data. Also the calculation of the amplitude of the dominant mode in the aperture of an X band waveguide for the same ABC spacing is accurate to within 2 % in magnitude and 2° in phase when compared to a method of moments calculation. These numbers were found to be typical for the aperture radiation problems considered here. The apertures considered here have a maximum dimension that is on the order of 1λ . As an example of the resources required for a solution: for the simulation of the unflanged waveguide with the ABC at $\lambda/2\pi$ (data presented in Figure 3) the run time for 3 solution passes was less than one hour on an HP 735 workstation with a 99 MHz. processor and 400 MB memory.

Overview of the FEM

To understand the results presented here it is useful to first review the basics of the FEM. See Reference 7 for more complete details on the FEM. In the FEM, the solution space is broken into small regions called finite elements. The elements used in electromagnetics are often tetrahedral as illustrated in Figure 1. This element has the advantage of being both flexible for modeling shapes and allowing closed form integrations. Since the solution space is split into small elements it is very easy to model geometries that contain different materials. This is most helpful when simulating printed circuit geometries.

The electric field in each element is approximated by using the tangential components along each edge as shown in Figure 1. This choice of approximation functions eliminates the spurious modes that can cause problems in finite element simulations [8]. The tangential electric fields are approximated by polynomials that contain unknown weighting coefficients, E_i . The electric field must satisfy the vector wave equation:

$$\nabla \times \nabla \times \vec{E} = k^2 \vec{E} \quad (1)$$

The vector wave equation leads to the following variational principle:

$$F(\vec{E}) = \int (\nabla \times \vec{E})^2 ds - k^2 \int (\vec{E})^2 ds \quad (2)$$

The polynomial approximation functions are substituted into (2) and the resulting set of equations are minimized with respect to the unknown coefficients by setting the $\partial F / \partial E_i$ equal to 0 for all i . While the resulting matrix is generally large, it is sparse. This matrix equation is solved to find the unknowns, E_i .

In FEM simulation, the size, shape and location of the elements in the mesh is important to the accuracy of the solution. To reduce the possibility of a poor mesh causing inaccuracies, Delaunay tessellation and adaptive mesh refinement [16] was employed. In adaptive mesh refinement, the solution is first computed with a coarse initial mesh. The approximate solution is then substituted into the vector wave equation (1) to determine the error in each element. Next the elements that contain the largest errors are refined. The result is that the elements in those parts of the problem where the errors are the largest are reduced in size. The entire procedure is repeated until the desired accuracy is attained. In the CAE tool used here the user controls the definition of the initial mesh. The user can specify a seed value for various surfaces in the model. This seed value is the spacing of additional points added to the original problem description on a specified surface. These seed points become the vertices of the tetrahedral finite elements.

The Second Order ABC

Absorbing boundary conditions (ABCs) are of two general types. The first is the one derived by Bayliss and Turkel [9] in scalar form and then by Peterson [5] and by Webb and Kanellopoulos [10] in vector form. The basis of the derivation of this ABC is the far field expansion or Wilcox expansion [11]. The first term in this expansion provides a 377Ω impedance boundary that must be placed relatively far from radiating sources. The second type of ABC was derived by Engquist and Majda [12] in scalar form and by Sun and Balanis [13] in vector form. This ABC is derived by splitting the operator into two first-order operators and then approximating these first-order operators. This allows waves to travel in one direction only; hence, they are often called a one-way ABCs.

In this paper the second-order ABC presented in References [5 and 10] is used. It should be noted that although these ABCs are derived in the reference, these papers are purely theoretical and do not provide numerical examples of its accuracy. The purpose of this paper is to provide such examples.

This ABC is computationally efficient for the following reasons. First, it includes higher order terms compared to the first order ABC. Second, the ABC may be applied on a conformal boundary because it absorbs the outgoing wave on a piecewise basis. Finally, the finite element shape functions themselves are second order so that the ABC boundary may be placed very close to the source of the radiation.

The above discussion indicates that the new ABC behaves very much like the absorber used in an anechoic chamber. Therefore, one would expect that the second order ABC can be placed very close to the radiating structure and can be made to conform to the geometry. From antenna theory it can be shown that the near zone of an antenna can be broken into two separate regions: the reactive near zone and the radiating near zone regions [14]. The reactive near zone is the region closest to the geometry where the reactive fields are present. It is the fields in this region that contribute to the imaginary component of the input impedance. Since these are reactive fields one does not want to place an absorber in this region else the

amount of energy stored is affected. On the other hand, this should not be a concern in the radiating near zone. Therefore, one should be able to place the ABC in the radiating near zone of the geometry. Reference [14] states that the boundary between the reactive and radiating near zones may be as small as $\lambda/2\pi$ from the antenna. One would expect then that the lower limit on the ABC placement would be on the order of $\lambda/2\pi$.

Results for an Unflanged Waveguide

The computed data presented here was solved using an initial mesh that was seeded with mesh points every $\lambda/10$ over the aperture opening, over the input port and on the ABC boundary. Adaptive mesh refinement was applied twice to these initial values to perform a total of three solution passes. This was sufficient to ensure that the change in the value of the reflection coefficient from pass 2 to pass 3 was less than 0.02.

A problem with much of the waveguide antenna simulations presented in the literature is that the aperture plane is assumed to be an infinite ground plane corresponding to a waveguide with an infinite flange. While this assumption reduces the complexity of the mathematical model, it does not reflect the situation in the real world. To determine the optimum distance for placement of the ABC, it is important to simulate a geometry that does not have an infinite flange. The authors of Reference 15 considered such a problem: they studied the radiation from an unflanged WR3200 rectangular waveguide. This is the type of antenna used in large anechoic chambers for susceptibility testing. For the case considered in Reference 15 the antenna has a net input power of 44.8 watts at a frequency of 275 MHz. The FEM simulation model that was used is shown in Figure 2. This is a simple unflanged waveguide with an input port at one end. The waveguide is enclosed in a rectangular box on which is placed the ABC. The spacing D was varied and the data compared with the measured values. The results are shown in Figure 3. The data presented is the magnitude of the electric field along the $x=y=0$ line for a variety of values of z in the antenna's near zone. At the frequency

of operation the field points for the smaller spacings are less than 1λ from the opening. It should be noted that these field points are outside of the FEM mesh for the cases presented here. The values of the fields determined on the boundary are used to calculate the fields at points outside of the mesh (see [6] for details). From the data shown in Figure 3, it can be seen that for $D = \lambda/4$ and $\lambda/2\pi$ the differences between measured and computed results are less than ± 0.5 dB. The $\lambda/10$ case, though, is not as accurate. These results are an additional 0.5 dB smaller than the $\lambda/2\pi$ data when compared to the measured. In fact a case could be made that at this spacing the results are still very good. The FEM meshes for the 3 spacings had approximately the same number of unknowns (within $\approx 10\%$ of each other). The main difference between these three simulations was the size of the tetrahedra, not a significant increase in the number.

Another test of the solution procedure was to calculate the gain of the antenna using the far zone fields determined by the FEM/ABC approach. The gain for this antenna calculated using equation (2) in Reference 15 is 6.9 dB and the gain calculated in the simulation with $D = \lambda/2\pi$ is 6.5 dB. While the gain equation given in Reference 15 is approximate, it nevertheless indicates that a $D = \lambda/2\pi$ spacing can be used to accurately model this aperture problem. Thus, the ABC can be made to conform to the shape of the geometry and can be placed as close as $\lambda/2\pi$ from the aperture with accurate results for these geometries. Using $D = \lambda/4$ for the spacing does not significantly increase the accuracy of the results but does require a small increase in mesh size.

As a final note, the data for the $\lambda/2\pi$ and $\lambda/4$ cases appeared to converge to accurate values for the reflection coefficient after only one adaptive mesh refinement, but they were run for a second mesh refinement to be consistent with the other case.

The Aperture Fields for Flanged Waveguide Antennas

As stated in the introduction, the radiation from apertures has been studied in the past using the method of moments (MOM). Thus, the results from a MOM solution can also be used to verify the FEM simulations. Before discussing the specifics of this approach, it should be noted that this MOM procedure is designed to analyze waveguide antennas with infinite flanges only and it is not a general purpose CAE tool. In this simulation, the aperture plane is assumed to be an infinite ground plane and the aperture is closed using the equivalence principle. Equivalent magnetic currents are placed on either side of the short. These magnetic currents are approximated by a finite weighted sum of entire domain basis functions. The unknown weighting coefficients are determined using a Galerkin procedure. Vector potential modal functions were used as basis functions. The field approximation for the aperture shown in Figure 4 is as follows [2]:

$$\vec{E}_a \approx \sum_{n,m} [C_{nm} e_{y,nm} \hat{y} + D_{nm} e_{x,nm} \hat{x}] \quad (3)$$

where:

$$\begin{aligned} e_{y,nm} &= \sqrt{\frac{\epsilon_{0n}\epsilon_{0m}}{ab}} \sin\left(\frac{n\pi x}{a}\right) \cos\left(\frac{m\pi y}{b}\right) \\ e_{x,nm} &= \sqrt{\frac{\epsilon_{0n}\epsilon_{0m}}{ab}} \sin\left(\frac{m\pi y}{b}\right) \cos\left(\frac{n\pi x}{a}\right) \end{aligned} \quad (4)$$

and where ϵ_{0n} is Neumann's number. Since the MOM simulation assumes an infinite flange, a small ground plane was placed around the aperture in the FEM models. The ground plane extends $\lambda/4$ from each edge of the aperture in the $\pm x$ and $\pm y$ directions. The ABC is rectangular in shape. It is located at $D = \lambda/2\pi$ from the aperture and from the edges of the ground. The apertures and the ABC were seeded in the same way as before and a total of 2 passes were run for all of the simulations in this section.

Due to the orthogonality of the basis functions of (4), it is a simple task to calculate the coefficients C_{nm} and D_{nm} from the FEM

data. To compute C_{nm} or D_{nm} , the dot product of the fields in the aperture are taken with $e_{y,nm}\hat{y}$ for C_{nm} or with $e_{x,nm}\hat{x}$ for D_{nm} , and the result is integrated numerically over the aperture. Consider the data presented in Figures 5 and 6. The magnitude and phase of the first 4 modes in an X band waveguide operated at 10 GHz are shown. It was found previously that these four modes are sufficient to accurately model the aperture field in this antenna [2]. As stated previously, the FEM and MOM data for the dominant mode are within 2% in the magnitude and 2° in phase.

To verify that the size of the aperture does not significantly affect the results or require a larger ABC spacing, consider the data shown in Figure 7. This is for a waveguide of twice the dimensions as an X-Band waveguide ($a=1.8"$ and $b=0.8"$). It is operated at 10 GHz., making this antenna twice as large electrically as the one simulated previously. For this case the first 6 modes in the aperture are compared. The ABC was again rectangular and was spaced $\lambda/2\pi$ from the aperture and the edges of the ground. In this case there is also excellent agreement between the two sets of data, the dominant mode amplitudes are different by less than 5%.

As a final test, consider the data presented in Figure 8. For this case, there are two X band waveguide fed apertures (same dimensions as was used for Figures 5 and 6) in the ground plane. The geometry is shown in Figure 8a. The apertures are spaced 0.6" apart. One is driven and the other is connected to a matched load. Due to mutual coupling between the two aperture antennas, there is a non-zero field in the aperture of the undriven guide. The modal amplitudes of the fields in both apertures are shown in Figure 8. The ground plane again extends $\lambda/4$ beyond the apertures and the ABC spacing is $\lambda/2\pi$.

Conclusion

From the data presented here it is concluded that the new second order ABCs can be used very effectively with the finite element method to model aperture radiation problems. The new ABCs can be shaped to conform to the problem geometry and can be placed as close as $\lambda/2\pi$

from the aperture for accurate simulation. Since the finite element method is well suited to modeling real-life structures such as finite flanges and variations in enclosure shapes, it provides a new, powerful tool to analyze radiation problems efficiently.

It should be noted that these results are valid for the types of geometries presented here. It is possible that a complicated radiating geometry can be found where the reactive near zone ends at a distance that is greater than $\lambda/2\pi$. In that case, the ABC should be spaced at least that distance from the geometry for best results.

References

- [1] R. F. Harrington and J. R. Mautz, "A general network formulation for aperture problems," *IEEE Trans. on Ant. and Prop.*, Vol. AP-24, pp. 870-872, Nov. 1970.
- [2] J. W. Silvestro, "Mutual coupling in finite arrays of rectangular apertures," *MS Thesis*, Case Western Reserve U., 1984.
- [3] X. Yuan, D. Lynch and J. Strehbehn, "Coupling of finite element and moment methods for electromagnetic scattering from inhomogeneous objects," *IEEE Trans. on Ant. and Prop.*, Vol. AP-38, pp. 386-393, Mar. 1990.
- [4] J-M Jin and J. L. Volakis, "A finite element-boundary integral formulation for scattering by three dimensional cavity-backed apertures," *IEEE Trans. on Ant. and Prop.*, Vol. AP-39, pp. 97-104, Jan. 1991.
- [5] A. F. Peterson, "Absorbing boundary condition for vector wave equations," *Microwave and Optical Technology Letters*, Vol. 1, pp. 62-64, Apr. 1988.
- [6] *Ansoft's Maxwell SI Eminence: User's Manual*, Ansoft Corp., Pitts., PA, 1994.
- [7] J. Jin, *The Finite Element Method in Electromagnetics*, John Wiley & Sons, New York, 1993.
- [8] Z. J. Cendes, "Vector finite elements for electromagnetic field computation," *IEEE*

Trans. on Magnetism, Vol. MAG-27, pp. 3953-3966, 1991.

[9] A. Bayliss and E. Turkel, "Radiation boundary conditions for wave like equations," *Comm. Pure Appl. Math.*, Vol. 23, pp. 707-725, 1980.

[10] J.P. Weeb and V.N. Kanellopoulos, "Absorbing boundary conditions for the finite element solution of the vector wave equation," *Microwave and Optical Technology Letters*, Vol. 2, pp. 370-372, Apr. 1989.

[11] C.H. Wilcox, "An expansion theorem for electromagnetic fields," *Comm. Pure Appl. Math.*, Vol. 9, pp. 115-134, 1956.

[12] B. Engquist and A. Majda, "Absorbing boundary conditions for the numerical simulations of wave," *Math. Comput.*, Vol. 31, pp. 629-651, July 1977.

[13] W. Sun and C.A. Balanis, "Vector one-way absorbing boundary conditions for FEM applications" *IEEE Trans. on Ant. and Prop.*, Vol. 42, pp. 872-878, June 1994.

[14] A.D. Yaghjian, "An overview of near field antenna measurements," *IEEE Trans. on Ant. and Prop.*, Vol. AP-34, pp. 30-45, Jan. 1986.

[15] D.I. Wu and M. Kanda, "Comparison of theoretical and experimental data for the nearfield of an open ended rectangular waveguide," *IEEE Trans. on EMC.*, Vol. AP-31, pp. 353-358, Nov. 1989.

[16] Z. J. Cendes and D. N. Shenton, "Adaptive mesh refinement in the finite element computation of magnetic fields," *IEEE Trans. on Magnetism*, Vol. MAG-21, pp. 1811-1816, Sept. 1985.

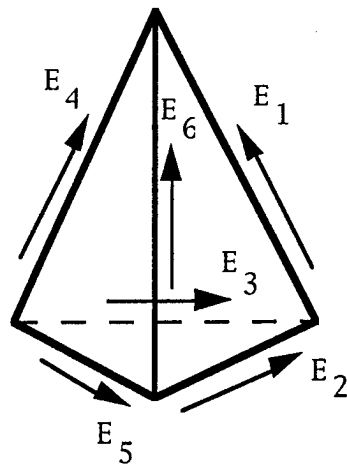


Figure 1 A tetrahedral showing the electric field components of the tangential vector finite element.

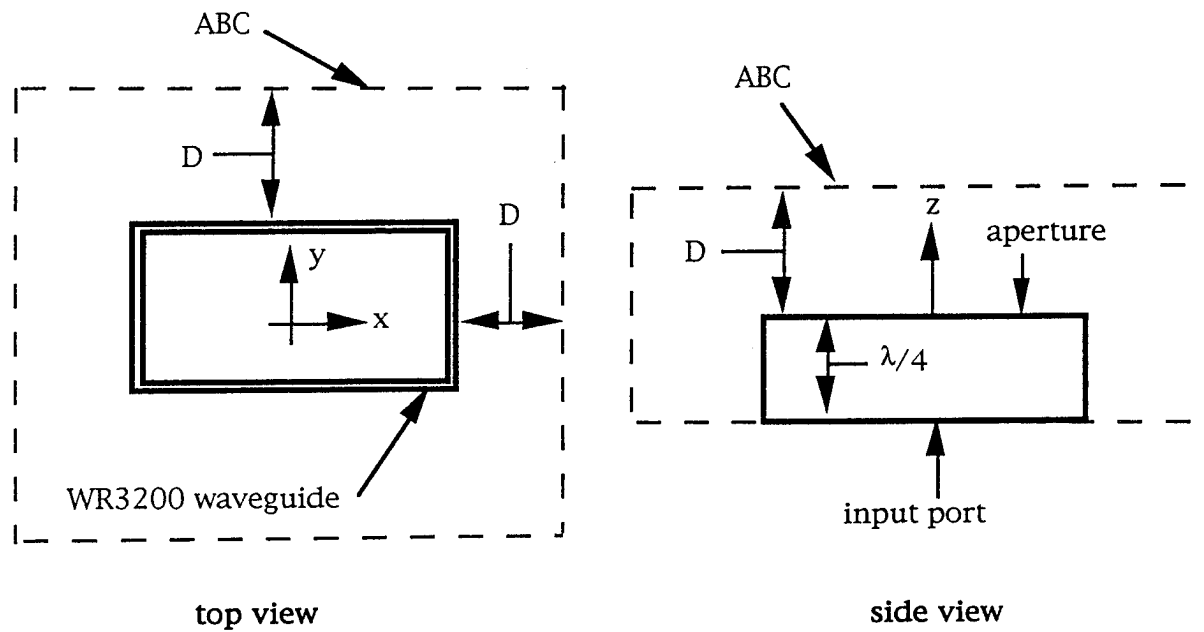


Figure 2 FEM simulation model of the unflanged rectangular waveguide antenna.

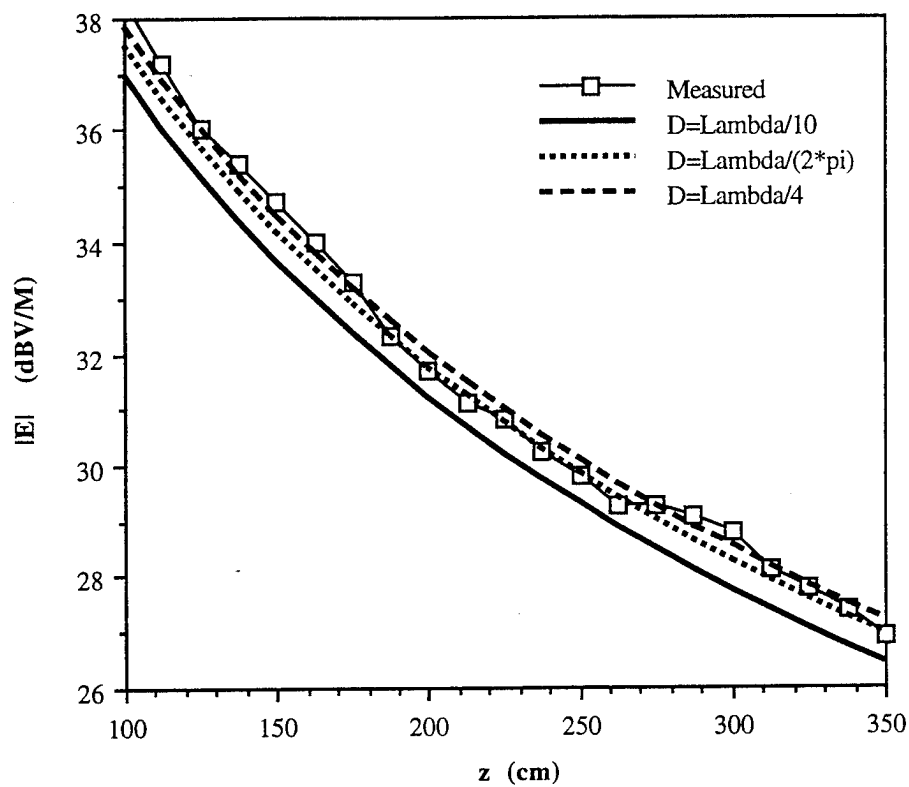
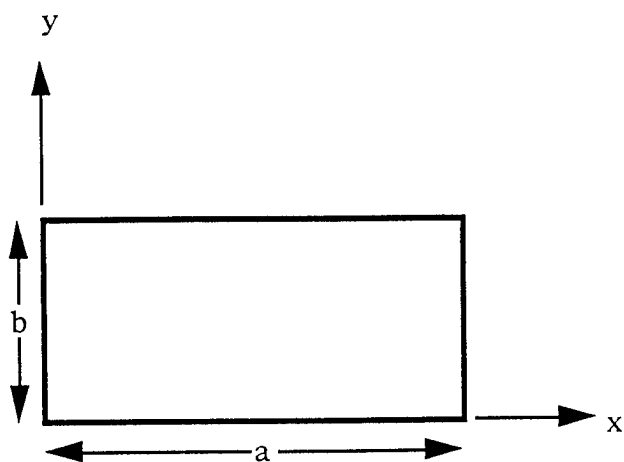


Figure 3 Magnitude of the near zone electric field along the center axis of the aperture. The values are in dBV/M.



infinite ground plane ($z=0$)

Figure 4 The dimensions and coordinate system for the flanged waveguide antenna used in the MOM simulations. For the X band waveguide used here: $a=0.9''$ and $b=0.4''$.

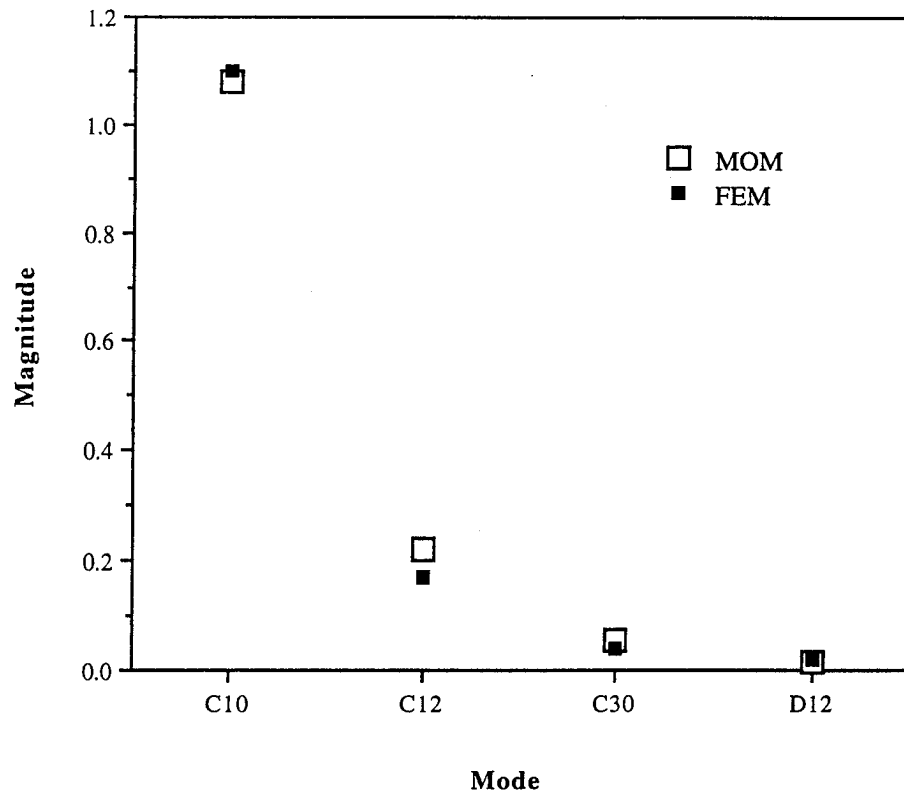


Figure 5 Magnitude of the modal amplitudes for a flanged X band waveguide antenna.

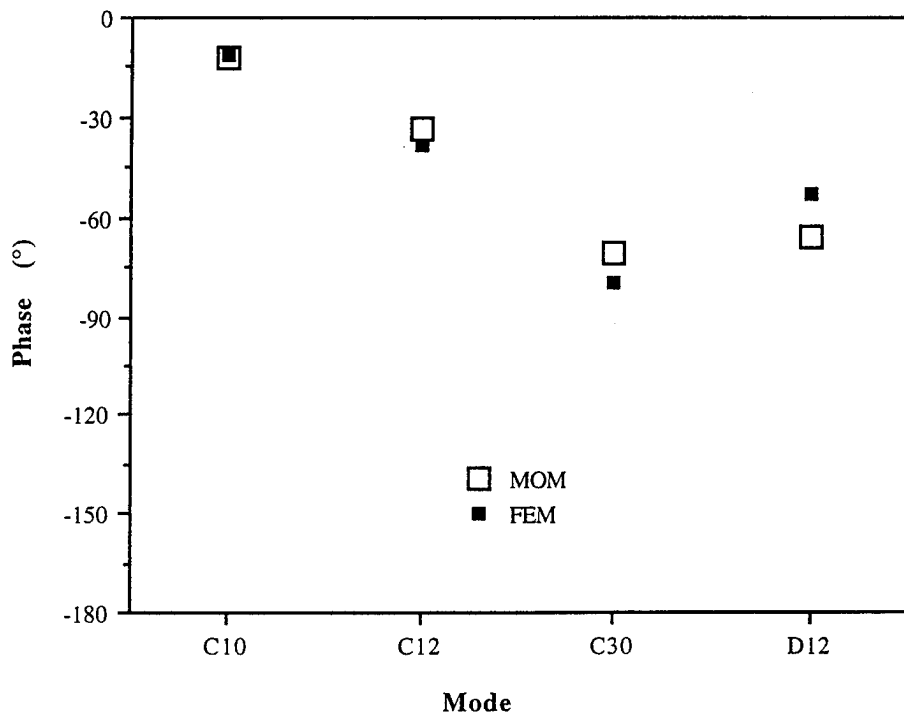


Figure 6 Phase of the modal amplitudes for a flanged X band waveguide.

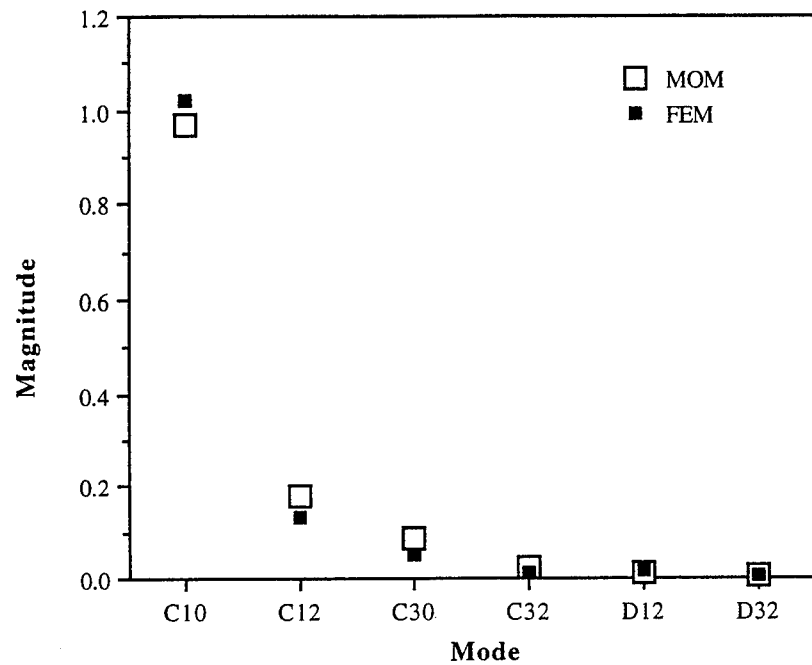
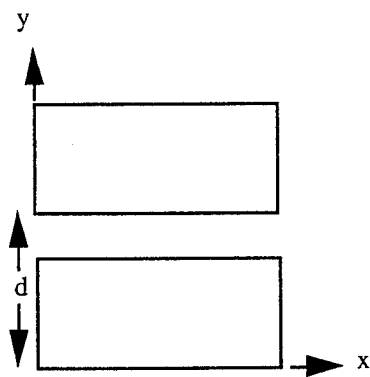
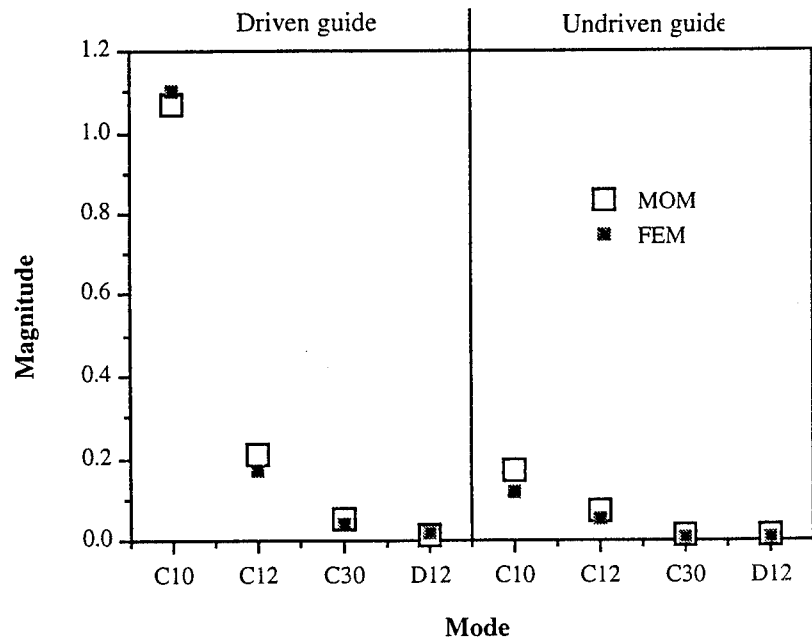


Figure 7 Magnitude of the modal amplitudes for a flanged waveguide antenna that is twice as large as a standard X band waveguide.



(a)



(b)

Figure 8 (a) Two aperture geometry. (b) Magnitude of the modal amplitudes for the case of a X band waveguides with $d=0.6$ ". The data on the left is for the driven guide, and the data on the right is for the undriven guide.

The FEMAX Finite-Element Package for computing three-dimensional electromagnetic fields

Gerrit Mur

Faculty of Electrical Engineering, Center for Technical Geoscience
Delft University of Technology, P.O. Box 5031, 2600 GA Delft, The Netherlands

ABSTRACT. *The structure and the properties of the FEMAX package are discussed. The FEMAX finite-element package is an efficient and highly accurate package especially designed for computing three-dimensional transient as well as time-harmonic electromagnetic fields in arbitrarily inhomogeneous, (an)isotropic media. The most unique features of the FEMAX package are that 1) the electric field strength is computed directly, i.e. without the intermediate use of (vector) potentials, 2) when inhomogeneities are encountered in the domain of computation, the package automatically chooses edge elements to ensure that all local continuity conditions can be met, nodal elements are used elsewhere, and 3) that the electromagnetic compatibility relations are taken into account in the formulation of the finite-element method used, thus avoiding spurious solutions. These features are included in the package in such a way that optimum results are obtained both in regard to computational efficiency (storage and time) and in regard to the desired accuracy.*

1 INTRODUCTION

When solving the electromagnetic field equations in a three-dimensional domain containing inhomogeneous media by using finite elements some important issues should be dealt with that are not often encountered in finite-element methods for other sets of partial differential equations.

The first important difference between the electromagnetic field equations and other sets of partial differential equations is that the field quantities in the former (the electric and the magnetic field strength) show jump discontinuities at interfaces between different media. This makes it necessary to use a computational technique that accounts for the continuity conditions of the fields across interfaces where the constitutive coefficients jump.

The second issue to be resolved lies in the fact that finite-elements methods for electromagnetic field problems often yield unwanted (spurious) solutions. Those

spurious solutions are due to the fact that some of the properties of the electromagnetic field, the electromagnetic compatibility relations [1, 2], are not represented properly in the finite-element method used.

1.1 Interfaces

A popular method to simplify the modeling of the continuity conditions at interfaces is to introduce electric and/or magnetic (vector) potentials [3] that are continuous along those interfaces. When using potentials in a numerical method, the finite-element method for instance, they have the disadvantage of yielding relatively inaccurate results for physical quantities like the electric or magnetic field strength. This is caused by the fact that the latter quantities can only be obtained by performing differentiations on the numerical results for the potentials which causes the loss of one order of accuracy. Obviously, much better convergence properties are obtained when numerical differentiations are avoided by formulating the problem directly in terms of the electric and/or the magnetic field strengths. When doing so, the continuity conditions along interfaces can, in principle, be dealt with by subdividing the problem space into a number of subdomains over which the constitutive coefficients are continuous functions of the spatial coordinates. The boundary conditions at the interfaces between those subdomains are imposed separately [4, 5]. This technique, however, is very difficult to implement for arbitrary configurations and yields conflicting conditions at nodes where the vector normal to the interfaces is not unique. When the electromagnetic field is computed in terms of the electric and/or the magnetic field strength, the problem of modeling fields in inhomogeneous media can be solved at the element level by using edge elements. Edge elements, however, are known to be less efficient than the commonly used nodal elements [6]. In [7] a method is described that virtually eliminates the computational disadvantage of edge elements [6] by using them only for modeling the

field along discontinuities and near reentrant corners, and by using nodal elements everywhere else. With this "mixed" method the corresponding program decides locally, for each combination of two adjacent subdomains in the discretized domain of computation, which type of element will be used. For regions in which the properties of the media are continuous functions of the spatial variables and for regions with "weak" discontinuities (i.e. discontinuities along which ignoring the jump in the normal component of the field strength would not yield unacceptably large errors) in electromagnetic properties between subdomains it will use nodal elements, for "large" differences it will use edge elements. Thus the method of modeling the field is automatically adapted to the problem at hand and all "strong" discontinuities are automatically accounted for. The degree of discontinuity above which edge elements are used is user-defined and has to be chosen in accordance with the final accuracy aimed at. In [8] a finite element code for time-harmonic electromagnetic fields was described that was designed according to the method described above.

1.2 Spurious solutions

Spurious solutions can be eliminated by taking into account all electromagnetic compatibility in the formulation of the finite-element method [1]. In this way the method used will accurately model the electromagnetic field equations, together with all its relevant properties, and spurious solutions are avoided.

In the present paper the version of the FEMAX finite-element code is described that was especially designed for computing transient electric fields in three spatial dimensions. It was developed on the basis of the above ideas.

2 NODAL ELEMENTS AND EDGE ELEMENTS

As was explained above, the FEMAX package uses a combination of nodal and edge elements. For topological reasons [9] the geometrical domain \mathcal{D} , in which the finite-element method is applied, is subdivided into tetrahedra that together span the polyhedron approximating \mathcal{D} . Consequently, the nodal and edge elements to be used will be defined on tetrahedra. The position vectors of the vertices of a particular tetrahedron \mathcal{T} are $\{\mathbf{r}_0, \mathbf{r}_1, \mathbf{r}_2, \mathbf{r}_3\}$, the outwardly directed vectorial areas of the faces of \mathcal{T} are $\{\mathbf{A}_0, \mathbf{A}_1, \mathbf{A}_2, \mathbf{A}_3\}$ and the volume of \mathcal{T} is denoted by V . Let \mathbf{r}_b be the position vector of the barycenter of \mathcal{T} , then the linear functions $\phi_i(\mathbf{r})$ that equal unity when $\mathbf{r} = x\mathbf{i}_1 + y\mathbf{i}_2 + z\mathbf{i}_3 = \mathbf{r}_i$ ($i = 0, 1, 2, 3$) and are zero at the

remaining three vertices of \mathcal{T} can be written as

$$\phi_i(\mathbf{r}) = 1/4 - (\mathbf{r} - \mathbf{r}_b) \cdot \mathbf{A}_i / 3V. \quad (1)$$

For obtaining consistency in the local degree of approximation we use consistently linear expansion functions. Therefore, the local nodal expansion functions $\mathbf{W}_{i,j}^{(N)}(\mathbf{r})$ in \mathcal{T} are taken as

$$\mathbf{W}_{i,j}^{(N)}(\mathbf{r}) = \phi_i(\mathbf{r})\mathbf{i}_j, i = 0, 1, 2, 3 \text{ and } j = 1, 2, 3, \quad (2)$$

and the local edge expansion functions $\mathbf{W}_{i,j}^{(E)}(\mathbf{r})$ in \mathcal{T} are taken as

$$\mathbf{W}_{i,j}^{(E)}(\mathbf{r}) = -\phi_i(\mathbf{r})a_{i,j}\mathbf{A}_j/3V, i, j = 0, 1, 2, 3, i \neq j, \quad (3)$$

where $a_{i,j} = |\mathbf{r}_i - \mathbf{r}_j|$ is used for dimensioning and scaling purposes. When $\mathbf{r} \in \mathcal{T}$, the electric field strength \mathbf{E} is locally expanded in terms of a combination of nodal and edge expansion functions through

$$\mathbf{E}(\mathbf{r}, t) = \sum_{i=0}^3 \sum_j e_{i,j}(t) \mathbf{W}_{i,j}^{(N,E)}(\mathbf{r}), \quad (4)$$

where $e_{i,j}(t)$ are the unknown, time-dependent, field expansion coefficients and where the limits of j depend on the type of expansion used (see (2) and (3)). Note that we have, in each tetrahedron, the possibility to use arbitrary combinations of nodal and edge expansion functions. The actual choice between them is made by the program, it depends on the degree of inhomogeneity in the material properties in the immediate vicinity of \mathcal{T} . Nodal expansion coefficients are the Cartesian components of the field at the vertices of the tetrahedra (the nodes of the mesh). Edge expansion coefficients are the oriented projections of the field at the edges taken near the ends of those edges. We note that (4) always contains 12 terms. For a discussion of the properties of local expansion functions the reader is referred to [6].

We now introduce global expansion functions as the sum of all local expansion functions that are related to the same expansion coefficient. The support of the global nodal expansion functions is the simplicial star [9] of the node to which they are related (the simplicial star of a node is the union of all tetrahedra that have that node in common). The support of the global edge expansion functions is the simplicial star of the edge to which they are related (the simplicial star of an edge is the union of all tetrahedra that have that edge in common). Since the support of global nodal expansion functions is much larger than the support of global edge expansion functions, the former are computationally more efficient than the latter and the former should be used whenever

the use of the latter is not necessary because of the local degree of inhomogeneity. For an illustration the reader is referred to Fig. 2 in [8]. By using the proper combination of nodal and edge expansion functions, optimum results are obtained both in regard to accuracy and in regard to computational efficiency [6, 8].

3 THE FINITE-ELEMENT FORMULATION

3.1 The wave equation

Eliminating the magnetic field strength \mathbf{H} from Maxwell's equations we obtain

$$\begin{aligned} \partial_t^2 \epsilon \cdot \mathbf{E} + \partial_t \sigma \cdot \mathbf{E} + \nabla \times (\mu^{-1} \cdot \nabla \times \mathbf{E}) = \\ -\partial_t \mathbf{J}^{\text{imp}} - \nabla \times (\mu^{-1} \cdot \mathbf{K}^{\text{imp}}), \end{aligned} \quad (5)$$

where $\mathbf{J}^{\text{imp}} = \mathbf{J}^{\text{imp}}(\mathbf{r}, t)$ and $\mathbf{K}^{\text{imp}} = \mathbf{K}^{\text{imp}}(\mathbf{r}, t)$ denote known impressed sources of electrical and magnetic current that are defined inside the domain of computation only, and where $\epsilon = \epsilon(\mathbf{r})$, $\sigma = \sigma(\mathbf{r})$ and $\mu = \mu(\mathbf{r})$ denote the permittivity, the conductivity and the permeability tensor, respectively. The wave equation is supplemented with initial conditions $\mathbf{E}(\mathbf{r}, t_0)$ and $\mathbf{H}(\mathbf{r}, t_0)$. In the package the domain of computation is subdivided in tetrahedra. Now, substituting the expansion (4) for the electric field strength in (5), a system of equations in the expansion coefficients is obtained by applying the method of weighted residuals. The set of weighting functions $\{\mathbf{W}_{p,q}^{(N,E)}(\mathbf{r})\}$ that is used is the same as the set of expansion functions. Using an integration by parts and adding the resulting equations over all tetrahedra, we obtain a system of coupled ordinary differential equations for $\{e_{i,j}(t)\}$ that can be written as

$$\begin{aligned} \sum_{i,j} (\partial_t^2 e_{i,j}) \int_{\mathcal{D}} \mathbf{W}_{p,q} \cdot \epsilon \cdot \mathbf{W}_{i,j} dV \\ + \sum_{i,j} (\partial_t e_{i,j}) \int_{\mathcal{D}} \mathbf{W}_{p,q} \cdot \sigma \cdot \mathbf{W}_{i,j} dV \\ + \sum_{i,j} e_{i,j} \int_{\mathcal{D}} (\nabla \times \mathbf{W}_{p,q}) \cdot \mu^{-1} \cdot (\nabla \times \mathbf{W}_{i,j}) dV = \\ \partial_t \int_{\partial \mathcal{D}_H} \mathbf{W}_{p,q} \cdot (\mathbf{n} \times \mathbf{H}^{\text{ext}}) dA \\ - \int_{\mathcal{D}} \mathbf{W}_{p,q} \cdot \mathbf{J}^{\text{imp}} dV \end{aligned}$$

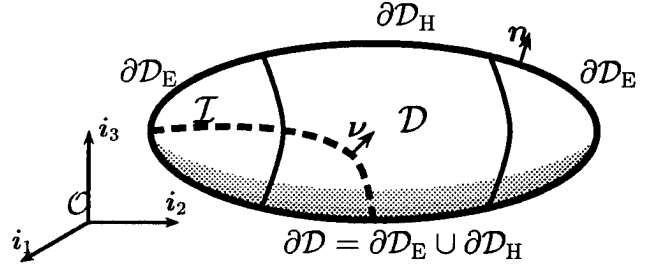


Figure 1: The domain of computation \mathcal{D} .

$$- \int_{\mathcal{D}} (\nabla \times \mathbf{W}_{p,q}) \cdot \mu^{-1} \cdot \mathbf{K}^{\text{imp}} dV \quad \forall p, q, \quad (6)$$

where $\partial \mathcal{D}_H$, see Fig. 1, denotes the part of outer boundary of the domain of computation \mathcal{D} on which the tangential components of the external magnetic field strength $\mathbf{H}^{\text{ext}} = \mathbf{H}^{\text{ext}}(\mathbf{r}, t)$ are prescribed and where \mathbf{n} denotes the unit vector along the outward normal to $\partial \mathcal{D}$. The tangential components of the external electric field strength $\mathbf{E}^{\text{ext}} = \mathbf{E}^{\text{ext}}(\mathbf{r}, t)$ are prescribed on $\partial \mathcal{D}_E$, where $\partial \mathcal{D} = \partial \mathcal{D}_E \cup \partial \mathcal{D}_H$ with $\partial \mathcal{D}_E \cap \partial \mathcal{D}_H = \emptyset$. External fields are defined outside the domain of computation only. For deriving (6) we have used the continuity of the tangential components of the magnetic field strength over all internal interfaces.

3.2 The compatibility relations

For eliminating all spurious solutions (6) must be augmented with the relevant electromagnetic compatibility relations [1]. Compatibility relations are properties of a field that are direct consequences of the field equations and that should be satisfied to allow the equations to have a solution. They were first introduced by Love [10] for elastodynamics and are also known in fluid dynamics [11]. For the electric field strength, which is the fundamental unknown in FEMAX, these compatibility relations are the volume divergence condition

$$\nabla \cdot (\partial_t \epsilon \cdot \mathbf{E} + \sigma \cdot \mathbf{E}) = -\nabla \cdot \mathbf{J}^{\text{imp}}, \quad (7)$$

the surface divergence condition at interfaces

$$\nu \cdot (\partial_t \epsilon \cdot \mathbf{E} + \sigma \cdot \mathbf{E}) + \nu \cdot \mathbf{J}^{\text{imp}} \quad \text{continuous across } \mathcal{I}, \quad (8)$$

where ν denotes the unit vector along the normal to the interface \mathcal{I} , and the condition applying to the normal component of the electric flux density at the outer boundary $\partial \mathcal{D}_H$

$$\mathbf{n} \cdot (\partial_t \epsilon \cdot \mathbf{E} + \sigma \cdot \mathbf{E}) = \mathbf{n} \cdot (\nabla \times \mathbf{H}^{\text{ext}} - \mathbf{J}^{\text{imp}}) \text{ on } \partial \mathcal{D}_H. \quad (9)$$

Each of these equations is added to (6) in a weighted sense. In this way the wave equation, together with its properties, is modelled in a weighted sense and spurious solutions are avoided.

Adding the weighted form of (7)-(9) to (6), a system of coupled ordinary differential equations for $\{e_{i,j}(t)\}$ is obtained that is solved in a standard manner using either single- [12] or two-step [13] integration methods. In practice the use of two-step methods has turned out to be preferable.

4 TIME-HARMONIC FIELDS IN THE TIME DOMAIN

The FEMAX code allows time-harmonic fields to be computed in the time domain. For maximum efficiency a transient is used with a transient period $0 \leq t \leq t_{\text{tr}}$. During this period the known right-hand side vector, representing the time harmonic excitation, is multiplied by a continuous function $f_{\text{tr}}(t)$ that generates a smooth transient from zero to steady state. For f_{tr} we use a function of the type

$$\begin{aligned} &= 0, & -\infty < t < 0, \\ f_{\text{tr}} &= (2 - \sin(\frac{t}{t_{\text{tr}}} \frac{\pi}{2})) \sin(\frac{t}{t_{\text{tr}}} \frac{\pi}{2}), & 0 \leq t \leq t_{\text{tr}}, \quad (10) \\ &= 1, & t_{\text{tr}} < t < \infty, \end{aligned}$$

other transients being available. Using f_{tr} we obtain, at $t = t_{\text{tr}}$, an approximation of the time-harmonic solution with a relatively small error term and steady state is achieved very efficiently. In most cases a value of t_{tr} in the range $5T \leq t_{\text{tr}} \leq 10T$, where T denotes the period in time of the time-harmonic sources, turns out to yield an optimum computational efficiency. Obviously the optimum choice for t_{tr} depends both on the problem at hand (larger domains of computation requiring longer transient times) and on the accuracy requirements. In general it can be said that t_{tr} should preferably be chosen such that the solution at $t = t_{\text{tr}}$ is already accurate enough to be used as a steady state solution and that no subsequent time stepping is required to obtain steady state. For further comments on this procedure the reader is referred to [14].

Computing time-harmonic fields in the time domain is computationally very attractive as compared with using frequency domain methods because of the fact it is usually very difficult to solve the system of equations obtained using the latter method which tends to generate

ill conditioned system matrices that usually are not positive definite. Experimentally we have found that for "large" problems ($>10,000$ unknowns) the time domain approach to solving time-harmonic problems is always more efficient and more accurate than the time-harmonic approach. The advantage of the time-domain, transient, approach over the time-harmonic approach increases with the number of unknowns and with the temporal frequency (for a constant size of the domain of computation).

5 ABSORBING BOUNDARY CONDITIONS

The FEMAX package contains simple local absorbing boundary conditions that model the infinite homogeneous surroundings of the domain of computation. These boundary conditions assume the field locally to consist of a plane wave travelling in a specific direction, usually in the direction that is normal to the outer boundary, out of the domain of computation. Absorbing boundary conditions of this type can be used for problems in which all sources of the electromagnetic field are located inside the domain of computation.

5.1 Inhomogeneous absorbing boundary conditions

In many practical problems, the field is excited by sources that are located outside the domain of computation. As an example one might think of the scattering of a plane wave by an obstacle. In cases like this we have an incident field $\{\mathbf{E}^{\text{inc}}, \mathbf{H}^{\text{inc}}\}$, which is the field in the absence of the scatterer, a total field $\{\mathbf{E}, \mathbf{H}\}$, and a scattered field $\{\mathbf{E}^{\text{scat}}, \mathbf{H}^{\text{scat}}\}$, which is defined as the difference between the total field and the incident field. Absorbing boundary conditions apply to scattered fields, they can be augmented to take into account the incident field in the following manner. Since absorbing boundary conditions are linear expressions in terms of the scattered field they can formally be written as a linear operator of the type

$$R(\mathbf{E}^{\text{scat}}, \mathbf{H}^{\text{scat}}) = 0. \quad (11)$$

Adding the trivial identity

$$R(\mathbf{E}^{\text{inc}}, \mathbf{H}^{\text{inc}}) = R(\mathbf{E}^{\text{inc}}, \mathbf{H}^{\text{inc}}) \quad (12)$$

to (11) we obtain

$$R(\mathbf{E}, \mathbf{H}) = R(\mathbf{E}^{\text{inc}}, \mathbf{H}^{\text{inc}}), \quad (13)$$

which relation is an inhomogeneous absorbing boundary condition that can be applied to the total field inside the domain of computation and that takes into account the

incident field as a contribution to the known excitation vector. Note that (13) applies to all absorbing boundary conditions that can be written as (11), from very simple local conditions to highly sophisticated global ones.

6 THE PROPERTIES OF THE FEMAX PACKAGE

The FEMAX package for computing time-domain electromagnetic fields in three spatial dimensions has the following properties and/or options:

- The electric field strength is used as the fundamental unknown quantity that will be approximated using consistently linear expansion functions.
- Because of including all relevant electromagnetic compatibility relations in the formulation, the results are free of spurious solutions.
- In the interior of the domain of computation, the user can specify arbitrary distributions of electromagnetic medium properties (permittivity, conductivity and permeability), the media may be anisotropic. It is also possible to specify specific density distributions for use in SAR computations.
- The package uses edge elements along discontinuities and nodal elements in regions with continuously varying medium properties. The contrast in properties of the media in two adjacent domains below which the medium is treated as having continuously varying properties is specified by the user.
- For a given distribution of medium properties and a given finite-element mesh, which has to be chosen fine enough to satisfy the accuracy requirements, the package automatically determines the numerically optimum distribution of the expansion functions that allow the solution to satisfy the user-defined local accuracy requirements.
- In the interior of the domain of computation, the user can prescribe arbitrary initial value distributions of the field strength as well as arbitrary time-dependent volume source distributions of imposed electric and/or magnetic current.
- The distributions of the medium properties as well as the volume source distributions can be specified either by supplying user-written subroutines for generating those quantities (in FORTRAN-77) or, much simpler, by using members of the collection of standard subdomains with standard distributions that are available in the package.

- At the outer boundary of the domain of computation, the user can prescribe arbitrary distributions of external electromagnetic fields. Local impedance boundary conditions for modeling lossy boundaries and (in)homogeneous absorbing boundary conditions for modeling radiation into an unbounded homogeneous medium surrounding the domain of computation are also available.

- Efficient sparse-matrix methods and different types of preconditioning are available for solving the system of algebraic equations.
- Field values and derived quantities can be computed at arbitrary collections of user-specified points in the configuration and as a function of time.
- FEMAX uses the SEPRAN finite-element package [18] for a number of general finite-element tasks like the generation of the mesh and the assembly of the system matrix from the FEMAX elements.

A number of programs is available for post-processing data prepared in FEMAX. They can be used interactively for previewing and for making contour plots (FEMAXPT and FEMAXPF) of field values, and of quantities that can be expressed in terms of the field values and material properties. FEMAXH is used for making plots of the evolution in time of fields values at specified locations. Use is made of either the NAG Graphics Library [15] or MATLAB [16].

7 NUMERICAL RESULTS AND COMPUTATIONAL REQUIREMENTS

Early results obtained by using the FEMAX package have been presented in [14, 17]. The results presented in those papers mainly served to illustrate the accuracy and the convergence properties of the package on a simple model problem. As a more practical example we shall now compute the specific absorption rate of a field in a mathematical model of a human head (a numerical phantom). The field is generated by a dipole antenna that is located near this phantom. A quarter part of the configuration is depicted in Fig. 2. The frequency is taken as $f=900\text{MHz}$, which is inside the frequency range used for the European GSM (Global System for Mobile Communication) network range. The phantom has a cubic shape, it consists of a cubic region $-0.095\text{m} \leq x, y, z \leq 0.095\text{m}$ filled with brain tissue ($\epsilon_r=43$, $\sigma=0.83\text{S/m}$, $\rho=1050\text{kg/m}^3$). The region outside the above region, but inside the cube $-0.1\text{m} \leq x, y, z \leq 0.1\text{m}$ has properties for modelling the skull ($\epsilon_r=17$, $\sigma=0.25\text{S/m}$, $\rho=1200\text{kg/m}^3$). Outside this region the properties of vacuum are assumed.

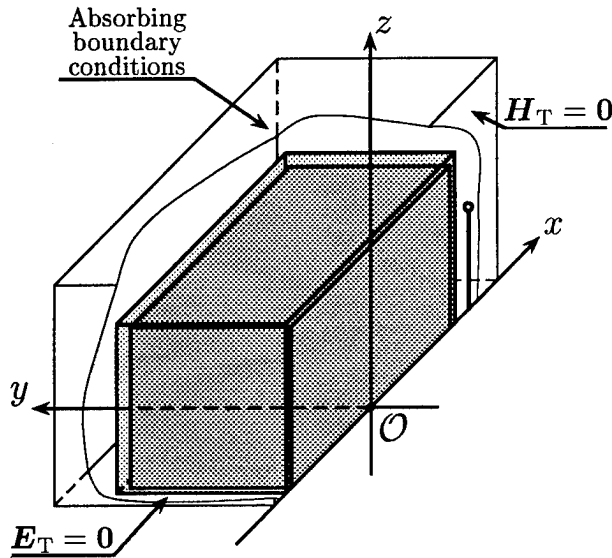


Figure 2: The numerical phantom

The antenna is modelled by a $\lambda/2$ dipole of length 0.166m, having its center at $(x, y, z) = (0.115, 0, 0)$ and its orientation parallel to the z -axis.

The problem was solved under the condition that edge elements are used when the relative contrast C_r in the numerical values of $\sigma(\mathbf{r}) + j\omega\epsilon_r(\mathbf{r})\epsilon_0$ in two adjacent tetrahedra exceeds 0.1 (with this choice, edge elements are used along all interfaces between the different domains), nodal elements are used otherwise. By using the symmetry of the configuration with respect to the planes $y = 0$ and $z = 0$ we can solve the problem for positive y and z values only, using the condition $\mathbf{E}_T(\mathbf{r}, t) = \mathbf{i}_3 \times \mathbf{E}(\mathbf{r}, t) = 0$ (the subscript T refers to the tangential components) at the plane $z = 0$ and the condition $\mathbf{H}_T(\mathbf{r}, t) = \mathbf{i}_2 \times \mathbf{H}(\mathbf{r}, t) = 0$ at the plane $y = 0$. The domain of computation $-0.11 \leq x \leq 0.2, 0 \leq y \leq 0.16, 0 \leq z \leq 0.16$ is surrounded by a mathematical boundary on which absorbing boundary conditions are applied. For the problem at hand the solution is expected to have a "singularity" in the immediate vicinity of the dipole antenna. Therefore we have used a non-uniform mesh that has its highest density near this antenna. A side view of this mesh, consisting of 144000 tetrahedra, is given in Fig. 3. Note that the mesh is such that the interfaces between different media coincide with interfaces between tetrahedra, in this way we have avoided staircasing in the modeling of the material properties.

For this configuration the Specific Absorption Rate

(SAR in W/kg) is required. In Fig. 4 the normalized SAR distribution is depicted for a cross-section in the plane $y=0$. The normalization was carried out such that the maximum SAR value anywhere in the configuration was set to 0dB. In Fig. 5 the SAR distribution is depicted along the line $(-0.1 \leq x \leq 0.1, y = 0, z = 0)$, the same normalization was used. The almost linear decay of the SAR (dB) values with decreasing x -values reflects the exponential decay of the field in the highly lossy tissues. The "roughness" of the result in Fig. 5 is due to the fact that a relatively coarse mesh had to be used away from the antenna. For $x \leq 0.05$ about 5 elements per wavelength were used, near the antenna a much denser mesh was used and, consequently, much smoother results were obtained for $x > 0.05$.

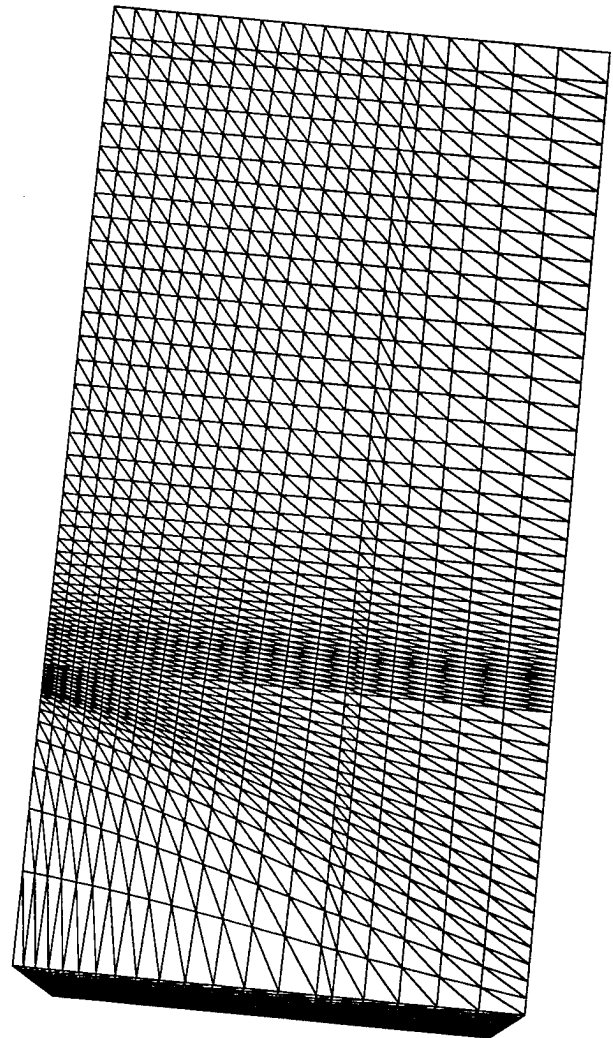


Fig. 3. The mesh used

The computational effort for solving a problem follows from the effort required for generating the system matrices, the effort for solving the equations each time step and the number of time steps. Since the matrices are stored in compact mode (ignoring all zero's) the solution of the system of equations can be obtained only by using iterative methods because of which the solution time depends on the number of iterations required. The actual number of iterations for solving a problem iteratively each time step is relatively small and depends on the type of preconditioning available for the problem at hand. Typically 2 - 20 iterations are required for solving a system of equations with 100,000 unknowns. The computational effort increases only slightly faster than linear with the number of unknowns and linear with the number of time steps required. For large problems with many time steps the computational effort for generating the system matrices is negligible in comparison to the computational effort required for the integration of the system of differential equations along the time axis.

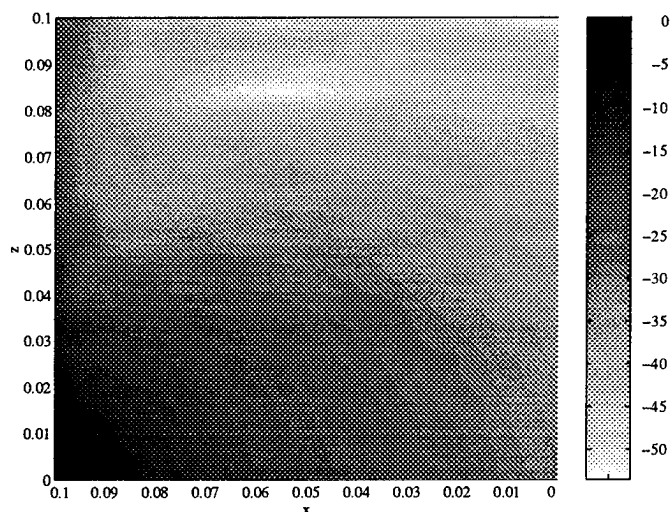


Fig. 4. The normalized SAR distribution in the plane $y = 0$ in dB.

For the problem at hand the total number of unknowns amounted to 114085, 3082 of them being prescribed through essential boundary conditions. Each of the three matrices contained 4116764 non-zero elements. The time-harmonic problem was solved with a transient of 10 periods in time, with 20 time steps on each period a total of 1055 iterations were required to solve the problem. All computations were carried out on a HP 9000-735/125 workstation, with 400Mbyte main memory space. The total computation time for obtaining the solution amounted to about 100 min.

8 THE PACKAGE

The FEMAX finite-element package consists of approximately 250 subroutines. It uses the SEPRAN [18] finite element package as a general finite-element background package that carries out tasks like the generation of the mesh, the assembly of the matrices and vectors, the solution of the systems of algebraic equations and the data management. Either the NAG Graphics Library [15] or MATLAB [16] is used for postprocessing. The storage requirements for the executable are 6.5Mbytes. FEMAX runs on both VAX-VMS and UNIX platforms. The FEMAX source code, together with an extensive User's Guide, are commercially available. The SEPRAN source code should be acquired separately.

The time-harmonic version of the FEMAX packages [8] is also commercially available. A FEMAX package for static and stationary electric or magnetic fields based on the theory presented in [2] is presently under development [19].

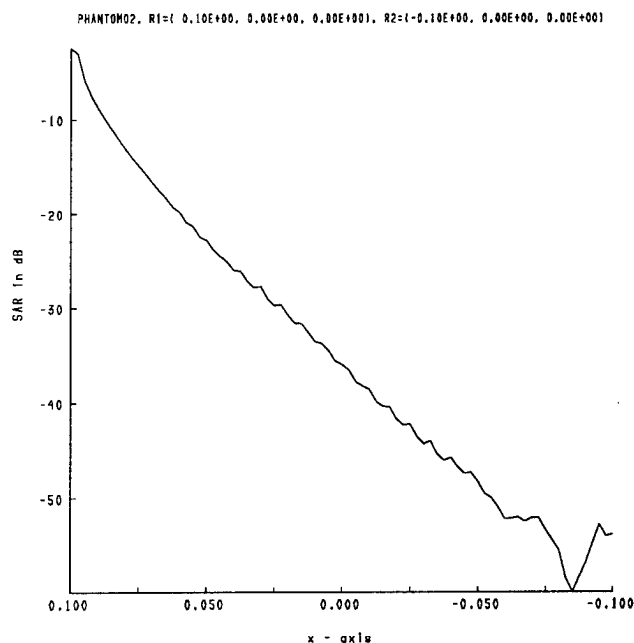


Fig. 5. The normalized SAR distribution along the line $y = 0, z = 0$ in dB.

9 CONCLUSION

The FEMAX finite-element package was described. This package was especially designed for computing transient as well as time-harmonic electromagnetic fields in three-

dimensional configurations containing inhomogeneous and (an)isotropic media. Because of formulating the problem in terms of the electric field strength directly, all problems that are inherent to potential formulations are avoided. The modeling of the conditions along internal interfaces in the configuration is performed automatically by the package, and the user can influence this process by prescribing the minimum degree of discontinuity C_r for which the discontinuity in the medium properties should be modelled to obtain the required accuracy.

10 ACKNOWLEDGEMENT

The development of the finite-element package described in this paper was financially supported through research grants from the Stichting Fund for Science, Technology and Research (a companion organization to the Schlumberger Foundation in the U.S.A.), from Schlumberger-Doll Research, Ridgefield, CT, U.S.A..

References

- [1] G. Mur, Compatibility relations and the finite-element formulation of electromagnetic field problems, *IEEE Transactions on Magnetics*, MAG-30, No. 5, pp. 2972-2975, 1994.
- [2] I. E. Lager and G. Mur, Compatibility relations for time-domain and static electromagnetic field problems, *ACES Journal*, Vol. 9, pp. 25 - 29, 1994.
- [3] O. Bíró and K. Preis, Finite-element analysis of 3-D eddy currents, *IEEE Transactions on Magnetics*, MAG-26, pp. 418-423, 1990.
- [4] M. Koshiba, K. Hayata and M. Suzuki, Finite-element formulation of the electric-field vector for electromagnetic waveguide problems, *IEEE Trans. Microwave Theory Techn.*, Vol. MTT-33, pp. 900-905, November 1985.
- [5] D. R. Lynch and K. D. Paulsen, Time-Domain Integration of the Maxwell Equations on Finite Elements, *IEEE Trans. Antennas Propagat.*, Vol. MTT-38, pp. 1933-1942, December 1990.
- [6] G. Mur, Edge elements, their advantages and their disadvantages, *IEEE Transactions on Magnetics*, MAG-30, No. 5, pp. 3552-3557, 1994.
- [7] G. Mur, Optimum choice of finite elements for computing three-dimensional electromagnetic fields in inhomogeneous media, *IEEE Transactions on Magnetics*, MAG-24, pp. 330-333, 1988.
- [8] G. Mur, The FEMAX finite-element package for computing three-dimensional electromagnetic fields in strongly inhomogeneous media, *Electrosoft*, Vol. 2, No. 6, pp. 261 - 270, 1991.
- [9] G. L. Naber, 'Topological methods in Euclidean space,' Cambridge: Cambridge University Press, 1980, p. 62.
- [10] A. E. H. Love, 'A Treatise on the Mathematical Theory of Elasticity', The Syndics of the Cambridge University Press, London, 1959, p. 49.
- [11] B.-N. Jiang and L. A. Povinelli, Optimal least-squares finite element method for elliptic problems, *Computer Methods in Applied Mechanics and Engineering*, Vol. 102, pp. 199-212, 1993.
- [12] O. C. Zienkiewicz, W. L. Wood, N. W. Hine and R. L. Taylor, A unified set of single step algorithms, Part 1: General Formulation and Application, *Int. J. Numer. Methods Eng.*, Vol. 20, 1529-1552 (1984).
- [13] O. C. Zienkiewicz, Finite elements in the time domain, Chapter 13 in: 'State of the art surveys on finite element technology,' pp. 405-449, Eds. A. K. Noor and W. D. Pilkey, American Society of Mechanical Engineers, Applied Mechanics Division, 1983.
- [14] G. Mur, The finite-element modeling of three-dimensional electromagnetic fields using edge and nodal elements, *IEEE Trans. Antennas and Propagat.*, AP-41, No. 7, pp. 948 - 953, 1993.
- [15] The NAG Graphics Library Reference Manual - Mark 4, NAG Ltd, Oxford, United Kingdom, 1990.
- [16] MATLAB, User's Guide, The MathWorks, Inc., Natick, Mass., USA, 1992.
- [17] G. Mur, The finite-element modeling of three-dimensional time-domain electromagnetic fields in strongly inhomogeneous media, *IEEE Transactions on Magnetics*, MAG-28, pp. 1130-1133, 1992.
- [18] A. Segal, 'SEPRAN, Sepra Analysis, User Manual,' Sepra, Leidschendam, The Netherlands, 1984.
- [19] I. E. Lager and G. Mur, The finite element modeling of static and stationary electric and magnetic fields, Accepted for publication in: *IEEE Transactions on Magnetics*, MAG-32, May, 1996.

A MOMENT METHOD FORMULATION FOR THE ANALYSIS OF WIRE ANTENNAS ATTACHED TO ARBITRARY CONDUCTING BODIES DEFINED BY PARAMETRIC SURFACES

F. Rivas, L. Valle and M.F. Cátedra

Departamento de Ingeniería de Comunicaciones, Universidad de Cantabria,
Avda. Los Castros s/n. 39005 Santander, Cantabria, SPAIN

ABSTRACT. A Moment Method (MM) technique for the analysis of wire antennas on board resonant-sized bodies modelled with parametric surfaces is presented. The approach may have useful applications for the study of the behaviour of wire antennas on board complex conducting structures like aircrafts. The current is represented by curved rooftop functions on the body, piecewise linear functions on the wires and a new junction function in the attachment region between the body and the antenna. The bodies are precisely defined by means of a small number of NURBS surfaces (Non Uniform Rational B-Splines) and Bézier patches (BP). In addition the new junction function that can be defined over any BP allows the antenna to be attached to any part of the body. Radiation patterns and input impedance calculations for several geometries are presented to show the accuracy of the method. The results are successfully validated when comparisons with measurements or results from other methods are carried out.

1 INTRODUCTION

The MM [1] is one of the most popular techniques for the analysis of electromagnetic scattering of arbitrary bodies of small or resonant size. The method gives good results when analyzing wire antennas and can be used to obtain the scattering field by surfaces represented by wire grid models [2]. However, the wire grid modelling does not work properly when near-field parameters such as input impedances or current distributions are calculated. Subsequently, a surface representation of the conducting bodies must be introduced.

A representation of the bodies by flat triangular or rectangular patches provides excellent results of near and far-field parameters for many problems, however it presents the disadvantage that high amounts of memory and CPU-times are needed when the geometry is electrically large. These problems can be substantially reduced by defining the MM basis functions directly over the models of the bodies based on meshes of NURBS surfaces and BP [3] because fewer number of patches are needed to represent the body accurately.

NURBS surfaces are B-Spline elements formed by a set of patches defined by polynomials, [3]. The coefficients of

these polynomials depend on merely a few control points (see Fig.1). A body that is quite complex, for instance a complete aircraft, can be modelled with nearly all its details by only a few hundred NURBS. Any NURBS can be expressed in terms of BP. NURBS surfaces are more efficient for representing and storing the information necessary for describing a geometry however BP are more suitable for the numerical computation of parameters associated with the local behaviour of a surface like curvatures, derivatives, etc. It is a fast and easy process to obtain the BP from a NURBS representation by applying the Cox-de Boor transformation algorithm [4].

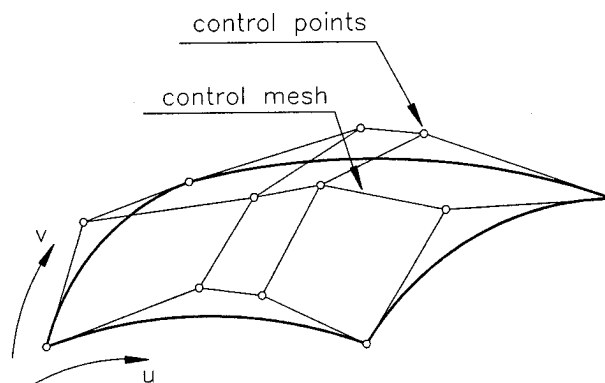


Figure 1. NURBS surface and its associated control points

In a previous paper [5] the authors presented a MM technique using NURBS surfaces and BP to represent the geometry of arbitrarily shaped scatterers. Modelling using that method implies that fewer basis functions are needed to obtain a precise representation of complex bodies. In that approach a new basis function associated with each boundary line between pairs of adjacent BP was introduced. These basis functions can be considered a generalization of the planar rooftop functions introduced by Glisson [6]. Curved "razor-blade" functions were considered as testing functions. This method was successfully validated when RCS values of several objects were obtained and compared with available data from other methods.

The purpose of this paper is to present an extension of the method mentioned above in order to analyze antennas

mounted over conducting surfaces. By establishing continuity of current at the wire-surface junction, a new special basis function (attachment or junction subdomain) has been introduced. This junction subdomain extends over a BP of the model and a segment of the attached wire antenna. This new subdomain presents an added advantage compared with previous works that can be attached to any of the BP of the body model. As the BP can be of complex shape it is possible to connect the antenna to any part of the body. Moreover the wire attachment itself need not be taken into account when the body is modelled. Therefore our formulation derived from the use of NURBS and BP allows us to consider more complex bodies and attachment points than in previously published works, [7-9].

This paper is organized as follows: Part 2 presents the description of the proposed MM scheme, giving an overview of the basis and testing functions used, the junction subdomain, the electrical fed model and the computation of the MM matrix terms; Part 3 presents the radiation patterns and input impedances for several canonical objects including comparisons with results obtained by other methods or measurements; the conclusions are outlined in Part IV.

2 FORMULATION

The electric current is represented by three kinds of basis functions depending on the part of the geometry considered: generalized curved rooftops over the BP that describe the body surface, piecewise triangular functions on the wire antennas and junction subdomains in the wire-surface attachment area.

2.1 Generalized curved rooftops

The body is modelled by means of meshes of NURBS surfaces that are subdivided into BP. A basis function is assigned to each one of the boundary lines between pairs of adjacent BP; each basis function extends only over the pair of patches that share a common boundary line. A constant charge density is imposed on the BP, [5]. Curved razor-blade functions, defined over the isoparametric lines which join the centres of the pair of BP associated with each basis function have been considered as testing functions.

2.2 Wire antennas

A thin wire approximation has been used, assuming that the radius of the antennas is much smaller than the length. Although the wires can be arbitrarily curved, a piecewise linear approximation is made by connecting straight cylindrical sections as can be seen in Fig.2. Triangle and pulse functions have been chosen as basis and testing functions, respectively. A procedure which bears a

considerable resemblance to that proposed in [6] has been considered for the numerical treatment of the MM terms.

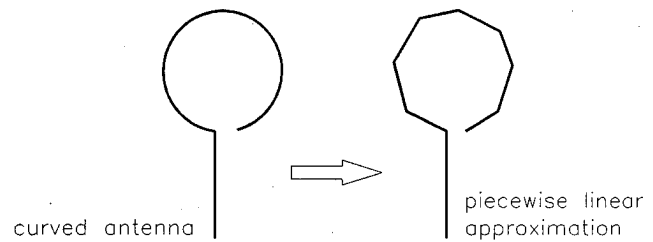


Figure 2. Curved antennas subdivided into a set of cylindrical straight segments

2.3 Attachment subdomain

This new subdomain extends over a wire segment and over a BP, as can be seen in Fig.3. The wire segment is assumed electrically short (e.g. $\lambda/36$ long) and normal to the surface (the other wire segments can be arbitrarily oriented). The current associated with the junction subdomain is a piecewise linear function (semi-triangle) on the wire and it is assumed that the current flows approximately radially from the attachment point on the BP. A total charge of $-1/j\omega$ on the wire (where ω is the radian frequency) and a charge of $1/j\omega$ on the patch are imposed. The charge continuity equation ($I = -j\omega q$) tells us that the total current of the junction subdomain is 1 Ampere. The charge density is assumed to be constant in both wire segment and surface patch. The exact shape of the current density on the BP of the junction subdomain is neither defined nor computed. The only imposition is that the charge density should be a constant function with a total charge of $1/j\omega$. As we will see below it is not necessary to know the exact shape of the current on the BP of the junction subdomain.

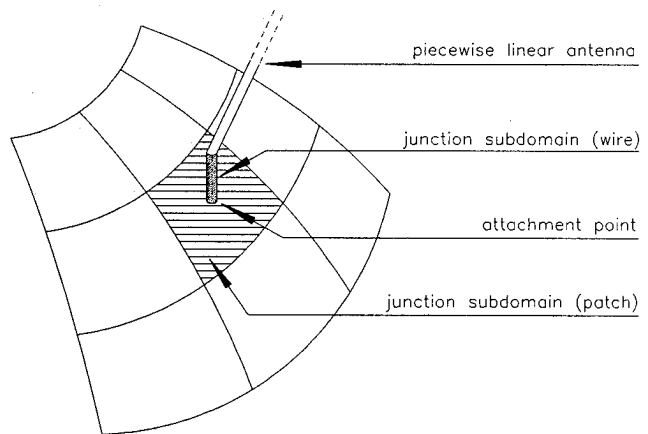


Figure 3. The junction subdomain formed by a wire segment and a Bézier patch

Fig.4 shows the shape of the testing function for the junction subdomain. A pulse function is defined as a testing function solely on the wire part of the junction subdomain. No testing is made in the patch surface of the junction subdomain because this patch is a part of the body geometry. It has been tested by the weighting functions associated with the generalized rooftop functions employed for the body, [5].

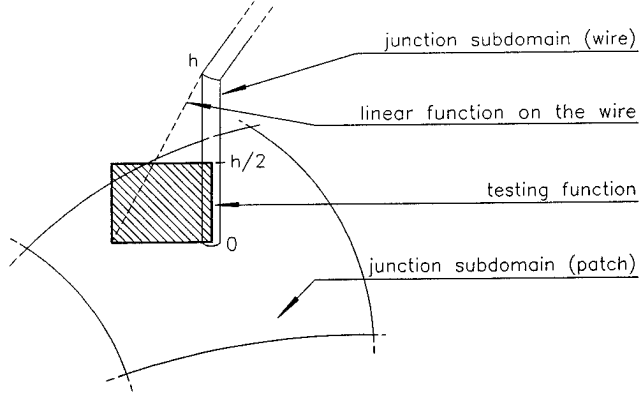


Figure 4. Testing functions for the junction subdomain

It is important to note that since one part of the junction subdomain is one patch of the NURBS meshing (not an additional disc or a flat patch), the connection of an antenna to the body does not imply any restriction or modification in the NURBS meshing. The sole restriction for the attachment points is that they should be positioned in or near the centre of a BP. This is not an important limitation because the junction patches are or can be made electrically small (typically a body is modelled using four to six patches per wavelength in its curved areas or eight to ten in its flat parts). In fact, this restriction is inherent to the discretization process of the problem that appears when using a numerical method like MM. In other words we must accept a quantization effect for the possible position where the wire can be placed. When attaching a wire antenna to a patch model of a body, two points on its surface are considered different only if they do not belong to the same BP.

2.4 MM coupling matrix

The objective is to solve the electric field integral equation (EFIE). To do that, the current density \vec{J} is expressed as a sum of the current density on each subdomain as:

$$\vec{J}(\vec{r}) = \sum_{i=1}^B \vec{J}_i^b(\vec{r}) + \sum_{i=1}^W \vec{J}_i^w(\vec{r}) + \sum_{i=1}^U \vec{J}_i^u(\vec{r}) \quad (1)$$

where B is the number of subdomains over the patches of the geometry modelled with NURBS surfaces, W is the number of subdomains defined on all the wire antennas of the problem and U is the number of junction subdomains. Then, the EFIE for this problem takes the form:

$$\hat{n} \times \vec{E}^{inc}(\vec{r}) = \hat{n} \times \sum_{i=1}^B \mathcal{L}[\vec{J}_i^b(\vec{r})] + \hat{n} \times \sum_{i=1}^W \mathcal{L}[\vec{J}_i^w(\vec{r})] + \hat{n} \times \sum_{i=1}^U \mathcal{L}[\vec{J}_i^u(\vec{r})] \quad (2)$$

where $\vec{E}^{inc}(\vec{r})$ represents the impressed electric field, \hat{n} is the normal vector and the integro-differential operator $\mathcal{L}[\vec{J}_i(\vec{r})]$ is defined by:

$$\mathcal{L}[\vec{J}_i(\vec{r})] = \frac{j\omega\mu}{4\pi} \int_S \vec{J}_i(\vec{r}') G(\vec{r}, \vec{r}') dS' - \frac{1}{j\omega 4\pi\epsilon} \nabla \nabla_s \cdot \vec{J}_i(\vec{r}') G(\vec{r}, \vec{r}') dS' \quad (3)$$

Equation (2) is converted into an equivalent set of linear equations. The coefficients of this system form the MM impedance matrix that can be grouped in nine boxes:

$$\begin{pmatrix} Z^{uu} & Z^{uw} & Z^{ub} \\ Z^{wu} & Z^{ww} & Z^{wb} \\ Z^{bu} & Z^{bw} & Z^{bb} \end{pmatrix}$$

where u denotes a junction subdomain, w a subdomain on a wire and b a subdomain on the body.

Since the objective of this paper is to introduce the connection between wires and surfaces, only the terms related with junction subdomains will be addressed in detail. The matrix terms related to the wire antennas have been treated by other authors, for instance [7-9] and those related to the subdomains over BP were introduced in [5].

If we consider the coupling between the i and the j -junction subdomains, we are referring to one of the terms of the Z^{uu} box of the MM matrix. This term is obtained by evaluating the expression:

$$Z^{uu}(i, j) = \langle T_i^u, \mathcal{L}[\vec{J}_j^u] \rangle \quad (4)$$

where T_i^u is the testing function associated with the i -junction subdomain (see Fig.4). This last expression can be computed as a sum of one inductive and one capacitive term depending on the potential vector and potential scalar of the j -subdomain, respectively.

The inductive term of (4) is given by the expression:

$$Z_{ind}^{uu}(i,j) = \frac{j\omega\mu}{4\pi} \int_0^{h_i^u/2} \left[\int_{S_{w_j}^u} J_w(\vec{r}') G(\vec{r}, \vec{r}') dS' + \int_{S_{s_j}^u} J_s(\vec{r}') G(\vec{r}, \vec{r}') dS' \right] d\vec{l} \quad (5)$$

where the current densities on the junction subdomain j have been separated into two parts depending on which part of this subdomain we are considering: $J_w(\vec{r}')$ on the surface of the wire segment ($S_{w_j}^u$) and $J_s(\vec{r}')$ on the surface of the BP ($S_{s_j}^u$). The inductive term defined in (5) can be largely simplified: a) if we neglect the contribution of the BP current because as J_s is approximately radial its equivalent momentum vanishes; b) if we approximate the current J_w by a pulse function that extends over the first half of the segment of the junction subdomain j and c) if we consider the inductive field to be constant along the wire segment over which the testing function of the i subdomain extends. The simplified expression as follows:

$$Z_{ind}^{uu}(i,j) \approx \frac{j\omega\mu}{4\pi} \frac{h_i^u}{2} \hat{d}l_i \cdot \int_0^{h_i^u/2} G(\vec{r}_{hi}, \vec{r}') d\vec{l}' \quad (6)$$

where \vec{r}_{hi} is the centre point of the wire segment corresponding to the i -junction subdomain. On the other hand, the capacitive term of (4) can be obtained as:

$$Z_{cap}^{uu}(i,j) = \frac{1}{4\pi\epsilon} \int_0^{h_i^u/2} \nabla \left[\int_{S_{w_j}^u} \rho(\vec{r}') G(\vec{r}, \vec{r}') dS' + \int_{S_{s_j}^u} \sigma(\vec{r}') G(\vec{r}, \vec{r}') dS' \right] d\vec{l} \quad (7)$$

where $\rho(\vec{r}')$ and $\sigma(\vec{r}')$ are the charge densities on the wire segment and on the BP surface of the junction

subdomain j , respectively. Taking into account the fact that these densities are constant and that the total charge in the surfaces is equal to $1/j\omega$ we have:

$$Z_{cap}^{uu}(i,j) = \frac{-1}{4\pi\epsilon j\omega} \int_0^{h_i^u/2} \nabla \left[\frac{1}{h_j^u} \int_0^{h_j^u} G(\vec{r}, \vec{r}') dl' - \frac{1}{S_{s_j}^u} \int_{S_{s_j}^u} G(\vec{r}, \vec{r}') dS' \right] d\vec{l} \quad (8)$$

Taking into account that:

$$\int_a^b \nabla f(r) dr = f(b) - f(a) \quad (9)$$

expression (8) can be re-written as:

$$Z_{cap}^{uu}(i,j) = \frac{-1}{4\pi\epsilon j\omega} [f(h_i^u/2) - f(0)] \quad (10)$$

where the function f is defined as:

$$f(l) = \frac{1}{h_j^u} \int_0^{h_j^u} G(\vec{r}, \vec{r}') dl' \bigg|_{r=l} - \frac{1}{S_{s_j}^u} \int_{S_{s_j}^u} G(\vec{r}, \vec{r}') dS' \bigg|_{r=l} \quad (11)$$

Similar expressions for the rest of terms of the MM matrix can be obtained considering the domain and the limits of integration in each case. Thus, the capacitive and inductive term of the coefficient $Z^{uw}(i,j)$ are expressed as:

$$Z_{ind}^{uw}(i,j) = \frac{j\omega\mu}{4\pi} \int_0^{h_i/2} \left[\int_{l_j} J_a(\vec{r}') G(\vec{r}, \vec{r}') dl' \right] d\vec{l} \quad (12a)$$

$$Z_{cap}^{uw}(i,j) = \frac{-1}{4\pi\epsilon j\omega} \int_0^{h_i/2} \nabla \left[\int_{l_j} \nabla J_a(\vec{r}') G(\vec{r}, \vec{r}') dl' \right] d\vec{l} \quad (12b)$$

where l_j is the wire segment of the j -antenna subdomain and J_a represents the current on that subdomain.

If it is assumed that the j subdomain of the body is shared by the Bézier's patches A and B , being J_b^A and J_b^B the current of the basis function on both patches respectively, the coefficient $Z^{ub}(i,j)$ is defined as:

$$Z_{ind}^{ub}(i,j) = \frac{j\omega\mu}{4\pi} \int_0^{h_i/2} \left[\int_{S_A} J_b^A(\vec{r}') G(\vec{r}, \vec{r}') dS' + \int_{S_B} J_b^B(\vec{r}') G(\vec{r}, \vec{r}') dS' \right] d\vec{l} \quad (13a)$$

$$Z_{cap}^{ub}(i,j) = \frac{-1}{4\pi\epsilon j\omega} \int_0^{h_i/2} \left[\nabla \left[\int_{S_B} G(\vec{r}, \vec{r}') dS' - \int_{S_A} G(\vec{r}, \vec{r}') dS' \right] d\vec{l} \right] \quad (13b)$$

where S_A and S_B are the areas of the patches A and B .

Finally, all the integral involved in the expressions for the coupling impedances are carried out numerically by means of the Gauss' Quadrature Method. This algorithm avoids the singularity of the Green's function which occurs when the points \vec{r} and \vec{r}' coincides. Because of this, the expressions developed above hold for the self-terms.

In the study presented in this paper the magnetic current frill model is used to feed the antennas. For this purpose, a voltage of 1 volt is distributed among the subdomains which share the BP where the wire is attached, as shown in Fig.5. This figure shows the digitized impressed voltage which is associated to each one of these subdomains to approximately model the magnetic current frill.

3 RESULTS

Several geometries have been analyzed in order to validate the method presented. The results include examples of monopole antennas attached to perfectly conducting bodies such as spheres, cylinders and other ground planes. Radiation patterns and input impedance values have been obtained and compared with measurements or results from other methods.

3.1 Monopole on conducting sphere

Figs.6-7 shows a quarterwave monopole antenna on a conducting sphere. Computed results for $a=\lambda/4$ and $a=\lambda/8$, are presented (solid line) and compared with those taken

from [10]. The sphere has been modelled by a mesh of BP that form 4 meridians and 9 parallel lines (76 basis functions on the sphere). Good agreement is observed in both cases. It is important to notice that, since the sphere is a body of revolution, the patches on the poles are triangular and considerably smaller than the remaining patches but no special treatment of the current has been applied.

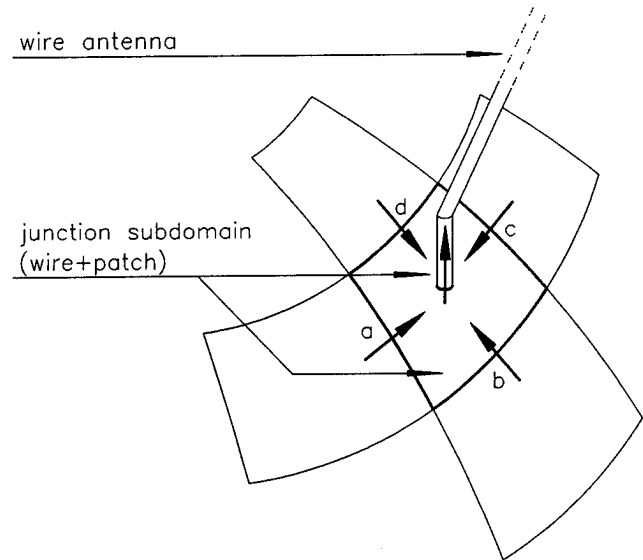


Figure 5. Feeding model for the attached antenna. An impressed voltage of 0.5 Volts is imposed on the junction subdomain and on the regular surface subdomain a , b , c and d that surrounds the antenna

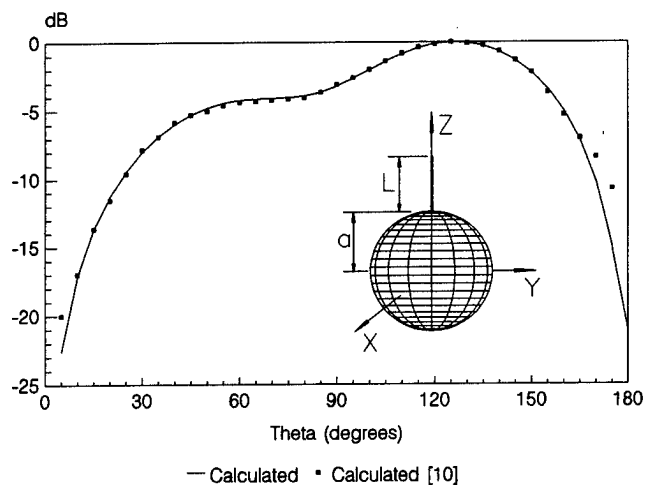


Figure 6. Radiation pattern of an $\lambda/4$ monopole on a $\lambda/4$ sphere

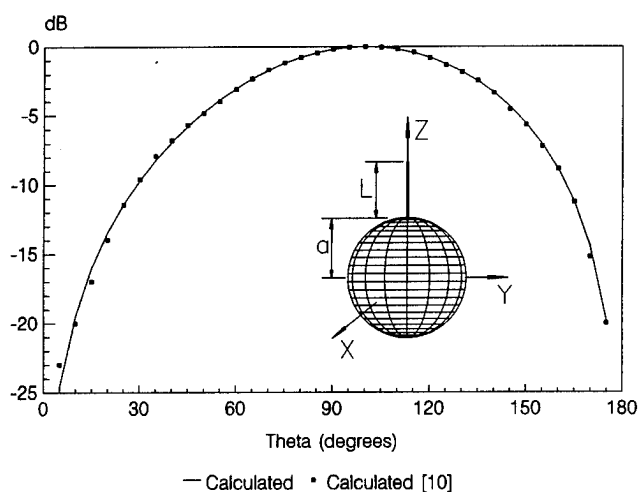


Figure 7. Radiation pattern of an $\lambda/4$ monopole on a $\lambda/8$ sphere

3.2 Monopole on a conducting cylinder

Fig.8 shows the configuration of a monopole antenna (A) diametrically opposite a passive boom (B) on the surface of a cylinder of height and diameter $0.22m$ and $0.20m$ respectively. The wavelength is $0.36m$. Computed values (solid line) for the $\phi=0^\circ$ cut are compared in Fig.8 with measured data (points) taken from [8] for a monopole length $= 0.08m$ and a boom length $= 0.44m$. Assuming that the z -axis coincides with the cylinder axis, the mesh of BP of the cylinder is defined by 12 equidistant meridian lines (ϕ -constant curves) and 5 parallel lines (z -constant curves).

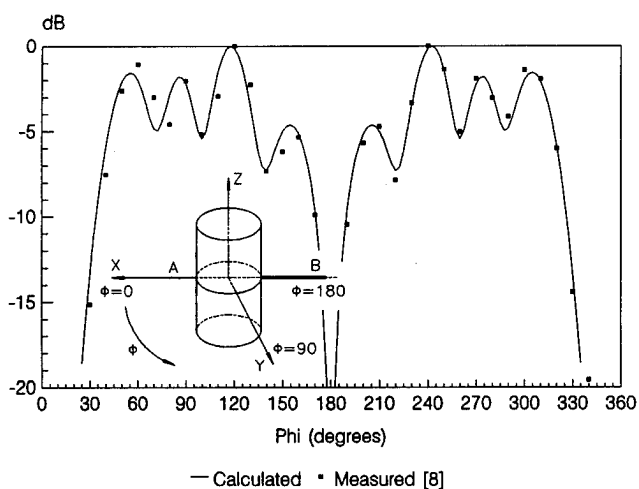


Figure 8. Radiation pattern of a monopole antenna (A) diametrically opposite a passive boom (B)

3.3 Monopole on an polihedral conducting body

A very special conducting box is shown in Fig.9. A quarterwave monopole antenna is mounted on the top plate of the box (the most narrow). The same figure also includes a sketch of the mesh considered for the box (eight patches per wavelength, the frequency is 317 MHz). The total number of rooftops on the body is 1504 . Figs.10-11 illustrate computed (solid line) and measured (dashed line) values respectively for the $\phi=0^\circ$ and $\phi=90^\circ$ cuts, respectively of the radiation patterns. It is important to notice that, although the antenna is very close to the edges of the model the agreement between computed and measured values is relatively good.

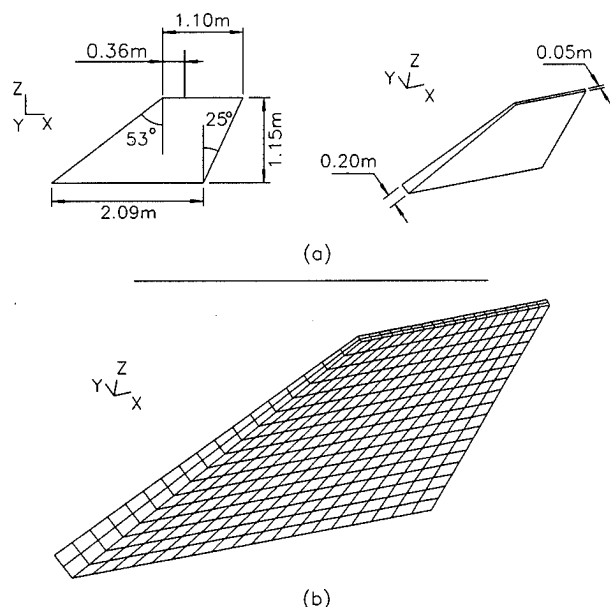


Figure 9. (a) Conducting box with flat sides; (b) Mesh of BP used to model the box

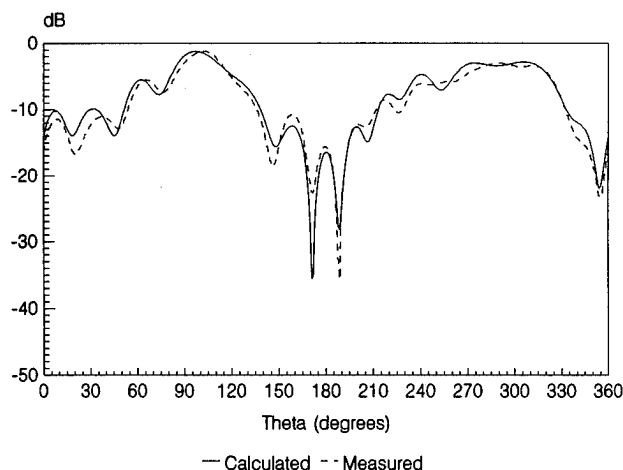


Figure 10. Radiation pattern of a monopole antenna on the top side of the box of Fig. 9 (cut $\phi=0^\circ$)

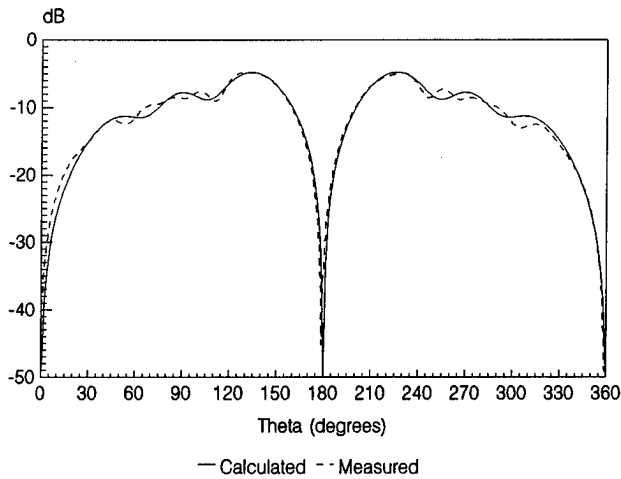


Figure 11. Radiation pattern of a monopole antenna on the top side of the box of Fig. 9 (cut $\phi=90^\circ$)

3.4 Input impedance of a monopole on a box

Fig.12 shows a monopole antenna centred on the top plate of a conducting box. The computed results for the input impedance of this antenna are compared with measurements taken from [11]. Several densities for the mesh of the conducting box have been considered depending on the range of frequencies considered (a number of ten patches per wavelength is always guaranteed). A sketch of the mesh for the frequency band 1.75 to 4.0 GHz is included in the figure. The monopole has been modelled considering 20 subdomains for all the frequency band. A good agreement between calculated and measured data is also observed.

3.5 Input admittance of a monopole on a plane with attached reflected plate

Finally, Fig.13 shows a monopole antenna centred on a conducting flat plate with a reflected plate attached to one side of the ground plane. The mesh considered for all the frequency band is included in the same figure. As in the previous case the monopole has been modelled also by 20 subdomains. The radius of the monopole is $0.0008m$. The computed results for the input admittance of this antenna are compared with measurements taken from [7]. The density for the mesh of the conducting plates that has been considered for all the range of frequencies analyzed is shown in the same figure (a number of ten patches per wavelength is always guaranteed). Good agreement between computed and measured data is observed.

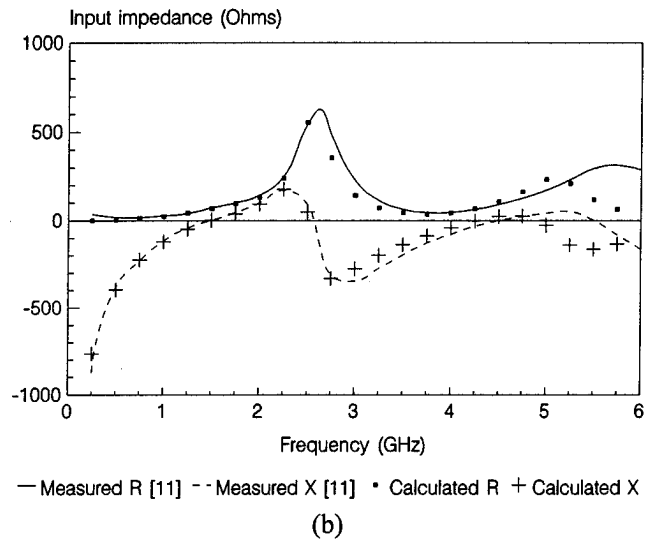
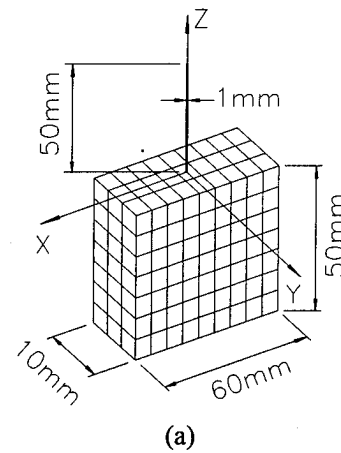
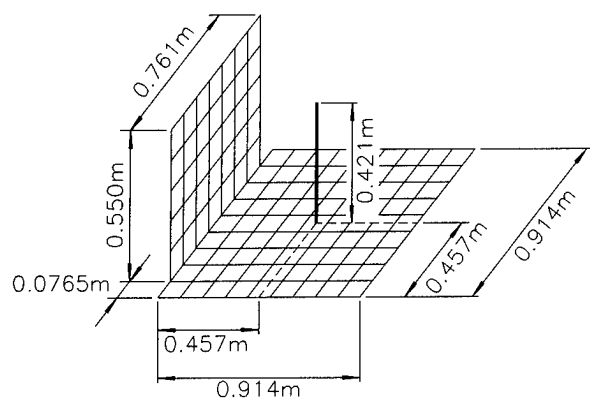


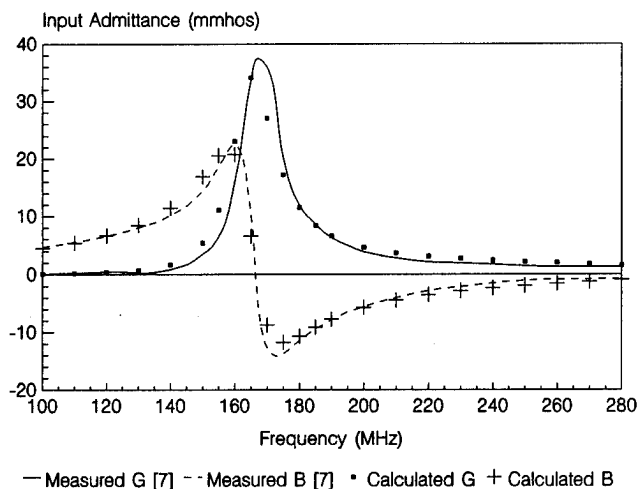
Figure 12. Monopole antenna on a conducting parallelepiped; (a) meshing of BP for the frequency band 1.75 to 4.0 GHz; (b) results for the input impedance

4 CONCLUSIONS

A new technique based on the MM to analyze antennas on board conducting surfaces has been presented. The scheme makes use of modern computational geometry tools to model the scatterers and the simplicity of wires to model the on-board antennas. This theory has been implemented in a computer code in order to obtain radiation patterns or input impedances of several canonical structures. The wire can be attached to any patch of the body meshing without requiring any special attention. Comparisons between numerical data and measurements show that the method is accurate and efficient for radiation patterns analyses. For input impedance the approach gives reasonably accurate results.



(a)



(b)

Figure 13. Monopole antenna on a flat ground plane with attached reflected plate; (a) meshing of BP for all the frequency range; (b) results for the input admittance

ACKNOWLEDGEMENTS

This work was sponsored by CASA and CICYT (Projects No TIC:93-0671- CO6-01, ESP91-0248). Measurements of Figs.10-11 were carried out by INTA.

REFERENCES

- [1] R.F. Harrington, "Field Computation by Moment Methods", New York, McMillan, 1968.
- [2] J.H. Richmond, "A Wire Grid Model for Scattering by Conducting Bodies", IEEE Transactions on Antennas and Propagation, Vol. AP-14, No. 6, pp. 782-786, November 1966.
- [3] G. Farin, "Curves and Surfaces for Computer Aided Geometric Design", Academic Press, INC, 1988.
- [4] C. de Boor, "A Practical Guide to Splines", Springer, 1978.
- [5] L. Valle, F. Rivas and M.F. Cátedra, "Combining the Moment Method with Geometrical Modelling by NURBS Surfaces and Bézier Patches", IEEE Transactions on Antennas and Propagation, Vol. 42, No. 3, pp. 373-381, March 1994.
- [6] A.W. Glisson and D.R. Wilton, "Simple and Efficient Numerical Methods for Problems of Electromagnetic Radiation and Scattering from Surfaces", IEEE Transactions on Antennas and Propagation, Vol. AP-28, No. 5, pp. 593-603, September 1980.
- [7] E.H. Newman and D.M. Pozar, "Electromagnetic Modelling of Composite Wire and Surface Geometries", IEEE Transactions on Antennas and Propagation, Vol. AP-26, No. 6, pp. 784-789, November 1978.
- [8] N.C. Albertsen, J.E. Hansen and N.E. Jensen, "Computation of Radiation from Wire Antennas on Conducting Bodies", IEEE Transactions on Antennas and Propagation, Vol. AP-22, No. 2, pp. 200-206, March 1974.
- [9] J.F. Shaeffer and L.N. Medgyesi-Mitschang, "Radiation from Wire Antennas Attached to Bodies of Revolution: the Junction Problem", IEEE Transactions on Antennas and Propagation, Vol. AP-29, No. 3, pp. 479-487, May 1981.
- [10] F.M. Tesche and A.R. Neureuther, "Radiation Patterns for Two Monopoles on a Perfectly Conducting Sphere", IEEE Transactions on Antennas and Propagation, Vol. AP-18, No. 5, pp. 692-694, September 1970.
- [11] R. Luebbers, L. Chen, T. Uno and S. Adachi, "Calculation of Radiation Patterns, Impedance and Gain for a Monopole Antenna on a Conducting Box", IEEE Transactions on Antennas and Propagation, Vol. 40, No. 12, pp. 1577-1583, December 1992.

A Posteriori Error Estimates for Two-Dimensional Electromagnetic Field Computations: Boundary Elements and Finite Elements

F.J.C. MEYER and D.B. DAVIDSON

Department of Electrical and Electronic Engineering
University of Stellenbosch, Stellenbosch 7600 South Africa
fjcmeyer@firga.sun.ac.za davidson@firga.sun.ac.za

Abstract

A brief summary of the variational boundary-value problem formulation of the 2D finite element/boundary element (FE/BE) method is presented. From this *a posteriori* error estimates and error indicators for the FE/BE method are developed and applied to electromagnetic scattering and radiation problems. The results obtained indicate that these error estimates and indicators can be obtained within negligible computational times and can be used successfully to obtain valuable *a posteriori* accuracy and convergence information regarding the reliability of the FE/BE method solutions.

1 Introduction

The 2D finite element/boundary element (FE/BE) method¹ has been used extensively over the past few years for solving electromagnetic problems numerically [1, 2, 3, 4, 5]. The method has proved to be highly successful and applicable to specifically scattering and radiation problems concerning inhomogeneous, arbitrarily shaped objects. However, the solution time and memory requirements of the method become impractical when electromagnetically large problems are considered. These limitations of the FE/BE method are obviously dependent on the computational hardware available.

A FE/BE method solution results in approximated field values in the regions under consideration. The accuracy of these solutions is dependent on the specific problem at hand as well as the approximation functions used with the FE/BE method. *A priori* knowledge of the accuracy and reliability of the FE/BE method is obviously an important consideration which has been investigated by a number of researchers [6, 1, 7]. Another

important consideration would be an *a posteriori* error estimate of FEM or FE/BE method solutions. Reliable *a posteriori* error estimates could serve as criteria for required accuracies as well as convergence checks for the FE/BE method solutions obtained. *A posteriori* error estimates for the FEM as well as the BEM have been under investigation for the past few years and have been applied successfully to a number of general engineering problems [8, 9, 10]. However, very little has been published on this topic in the computational electromagnetic literature and only recently has work started appearing, for example [11, 12]. A recent special issue of this journal contained several papers on error estimation, none specifically on FEM error estimates although the paper by Hsiao and Kleinman considers boundary integral error control [13]. Some commercial FEM programs include error estimates and adaptive meshes, but the algorithms are often proprietary.

In this paper, a brief summary of the FE/BE method formulation will be presented (section 2). A number of *a posteriori* error estimates and error indicators for FE/BE method solutions of electromagnetic problems will be formulated in section 3. These include local (in each finite element) and global Element Residual Method (ERM) error estimates [8, 9, 10], L^2 -norm boundary field and boundary field derivative error estimates [14, 15], a L^2 -norm Neumann boundary condition error indicator and a radar width error indicator. It will be shown that these are highly efficient error estimates with negligible computational times compared to the solution times of FE/BE method solutions. The *a posteriori* error estimates and error indicators developed will be applied to a number of FE/BE method solutions of electromagnetic scattering problems. The results obtained will be used to investigate the accuracy, reliability and applicability of the different error estimates and error indicators when applied to FE/BE method solutions of 2D electromagnetic problems.

In section 4 general conclusions on the work presented in this paper will be drawn and further research that needs to be done will be discussed.

¹The technique is also referred to as the finite element/moment method or finite element/integral equation method in the literature; there are sometimes differences in detail but the basic concepts are the same.

2 The 2D FE/BE Method

In this section the 2D FE/BE method formulation will be presented². The development of this formulation is not new, but the specific notation used is crucial for the development of the FE/BE method error estimates. A thorough understanding of the mathematics behind the FE/BE method is essential for the development of any kind of error analysis associated with the method. A rather *informal* discussion of the functional analysis formulation of the FE/BE method will be presented in this paper. This discussion is sufficient to prepare the reader for the development of the error estimates. (Details of the formal functional analysis formulation of the FE/BE method can be found in reference [16].)

The formulation will be presented for 2D Transverse Magnetic (TM_z) polarized scattering problems.³ The TM_z scattering formulation is a special case of the more general 2D scalar Helmholtz equation formulation. This equation serves as the governing equation for a variety of 2D electromagnetic problems, including static electric and magnetic problems⁴, as well as closed and open boundary electromagnetic problems for TM_z and TE_z polarization. The FE/BE method and the *a posteriori* error estimate methods considered in this paper are applicable to all the above mentioned electromagnetic problems.

2.1 Variational boundary-value problem formulation of the FEM

Consider figure 1. For 2D scattering problems involving a TM_z polarization incident field, the 2D electromagnetic field equation can be written as a boundary value problem [6, pp.185] [1, pp.72-73]. (Throughout this paper the electric field component associated with the TM_z polarized field, E_z , will be denoted by E):

$$\nabla \cdot \frac{1}{\mu_r} \nabla E + \epsilon_r k_0^2 E = 0 \quad \text{in } \Omega \quad (1)$$

²Only two-dimensional problems will be considered in this paper. Variation in the 2D $x - y$ plane will be assumed (for all fields and structures) with no variation in the z -direction (extending to infinity).

³The convention for polarization in a 2D plane which will be used throughout this paper is as follows: For TM_z polarization the magnetic field vector has only x and y components, thus \vec{H} is always transverse to the z plane. In this case \vec{E} has only a z component. For TE_z polarization the electric field vector has only x and y components, thus \vec{E} is always transverse to the z plane. In this case \vec{H} has only a z component.

⁴In these cases, the 2D scalar Helmholtz equation reduces to the 2D Laplace or Poisson equations.

with Dirichlet boundary condition on a perfectly conducting region

$$E = 0 \quad \text{on } \Gamma^{D_0} \quad (2)$$

and Neumann boundary condition on the fictitious boundary

$$\frac{\partial E}{\partial n} = g_1 \quad \text{on } \Gamma^{N_1} \quad (3)$$

where g_1 are the prescribed values for $\frac{\partial E}{\partial n}$ on Γ^{N_1} . The boundary-value problem of equations 1 to 3 can be written as a variational boundary-value problem [6, pp.219]:

$$\int_{\Omega} \left(\nabla E \cdot \frac{1}{\mu_r} \nabla v - \epsilon_r k_0^2 E v \right) d\Omega = - \int_{\Gamma^{N_1}} g_1 v d\Gamma^{N_1} \quad (4)$$

with v an arbitrary weighting or testing function on Ω . Using conventional finite element procedures [17][16, pp.14], equation 4 can be written in matrix form:

$$[S][E] + [T]\left[\frac{\partial E}{\partial n}\right] = 0 \quad (5)$$

with $[S]$ the FEM system matrix, $[E]$ the unknown field coefficient column matrix, $[T]$ the FEM boundary condition system matrix and $\left[\frac{\partial E}{\partial n}\right]$ the field derivative column matrix. Equation 5 is the FEM matrix equation for TM_z polarized, 2D electromagnetic problems. The solution of the FEM matrix equation 5 yields the approximated field solution, E , if g_1 of equation 3 is known and used to construct the column matrix $\left[\frac{\partial E}{\partial n}\right]$.

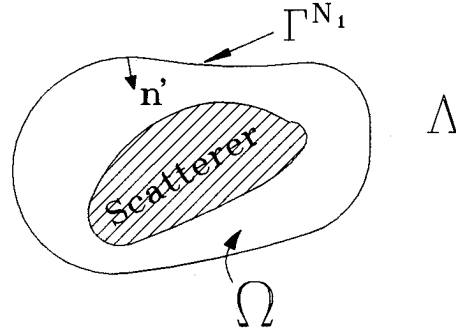


Figure 1: Finite region, Ω , in which the FEM will be applied, enclosed by boundary, Γ^{N_1} . Λ is an exterior free-space region extending to infinity.

2.2 The boundary element method

Many practical electromagnetic field problems, such as scattering and radiation problems, are open boundary problems. The domain of these problems extends to infinity, making the finite element method unsuitable for

the solution of such problems. One way to overcome this problem is to couple the finite element method with an unbounded region method such as the boundary element method. In this way, the advantages of both the FEM and BEM are exploited [1][5].

A fictitious boundary denoted by Γ^{N_1} can be defined around the structure under consideration dividing the solution region into an interior region, Ω , and an exterior region, Λ (see figure 1). A BEM solution of the normal field derivatives on Γ^{N_1} can be used as Neumann boundary condition for the boundary value field problem in Ω . The FEM can thus be applied to the field problem in Ω with appropriate boundary conditions (obtained with the BEM solution) on Γ^{N_1} .

Consider the exterior region Λ bounded by Γ^{N_1} and infinity. For electromagnetic field problems, the homogeneous free-space Helmholtz equation must be satisfied in this region. The variational form of the boundary element method integral equation [1, pp.299][14, pp.41][16, pp.17] can be written in the BEM matrix equation form [16, pp.19]:

$$[H][\tilde{E}] - [G] \left[\frac{\partial \tilde{E}}{\partial n'} \right] = [F^{inc}] \quad (6)$$

The matrix elements of $[H]$, $[G]$ and $[F^{inc}]$ can be calculated using the boundary element integral equation [16, pp.17] and the matrix elements of $[\tilde{E}]$ and $\left[\frac{\partial \tilde{E}}{\partial n'} \right]$ are unknown field coefficient values which can be obtained with the BEM solution. The elements of matrix $[F^{inc}]$ contain external source information. In the rest of this paper, E represents the FEM and \tilde{E} the BEM computed solution.

2.3 Coupling the FEM and BEM

For a closed region, Ω , a FEM solution is obtainable if certain boundary conditions are known. These could be Dirichlet and/or Neumann boundary conditions. For open boundary problems one can use the fictitious boundary (discussed in the previous sections) as closure of the finite, interior region, Ω , with inhomogeneous Neumann boundary conditions specified on the fictitious boundary Γ^{N_1} . By using $\frac{\partial \tilde{E}}{\partial n'}$ of equation 6 as the Neumann boundary condition on Γ^{N_1} , a solution of the FEM in Ω is obtainable. That is, g_1 of equation 3 can be set equal to $\frac{\partial \tilde{E}}{\partial n'}$ of equation 6 on Γ^{N_1} . (The minus sign is due to the direction of the normal n' — see figure 1):

$$g_1 = -\frac{\partial \tilde{E}}{\partial n'} \quad \text{on } \Gamma^{N_1} \quad (7)$$

Using the above equation together with equations 4 and 5 leads to a modified FEM matrix equation

$$[S][E] - [T] \left[\frac{\partial \tilde{E}}{\partial n'} \right] = 0 \quad (8)$$

Setting E of equation 5 equal to \tilde{E} of equation 6 on Γ^{N_1} and coupling the two matrix equations 6 and 8 (each containing *two* unknown coefficient column matrices) is thus equivalent to solving the FEM matrix equation of equation 5 with the Neumann boundary condition of equation 7 on Γ^{N_1} .

3 A Posterior Error Estimates

A reliable *a posteriori* error estimate for a FE/BE method solution would enable one to obtain valuable convergence information without having to solve the same problem, using a *larger* number of unknowns. The error estimate can thus be used as a convergence check for practical electromagnetic problems for which no analytical solution exists. This would be especially advantageous when electromagnetically large problems, reaching the practical solution time and memory limits of the computer at hand, are considered. This is true regardless of the computational power available.

Local and global finite element method error estimates have been under investigation for the past decade [8, 9, 10]. Of these, the Element Residual error estimate Method (ERM) seems to be the most reliable and the easiest implementable method. Applications of this FEM error estimate method were directed mainly at mechanical and fluid-dynamical problems although the method is applicable to a wide variety of *positive definite* FEM type problems [18]. The governing equation for static electric field problems (Laplace's or Poisson's equation) is positive definite, and the successful application of the ERM to such problems has recently been published [19]. The ERM applied to wave equation type problems, of which electromagnetic scattering and radiation problems are examples, will be considered in this section. Although the FEM system equations for such problems are not necessarily positive definite, an element residual type error estimate method will be introduced, which is applicable to such problems.

A L^2 -norm boundary **field** error estimate, which has been applied to linear acoustic problems [14, 15], and a L^2 -norm boundary **field derivative** error estimate have been investigated and will be modified for application to the BEM part of the FE/BE method solution. A L^2 -norm **Neumann boundary condition** error indicator

for the FE/BE method will also be introduced. The L^2 -norm error estimates and error indicator will be used to develop far-field error indicators for FE/BE method solutions of electromagnetic problems. These far-field error indicators are especially important when considering electromagnetic problems concerning radar-width and radiation intensity results, obtained with the FE/BE method solution.

The mathematical development of the error estimates and error indicators presented in this section, is based on the functional analysis formulation of the FE/BE method, presented in section 2 and, in more detail, in reference [16].

3.1 Error Estimates for the FEM

The Element Residual error estimate Method (ERM) for FE/BE method solutions of electromagnetic scattering problems will be formulated in this section. This is an *a posteriori* error estimate method, and can be applied after a FE/BE method solution has been obtained. Let us denote a "first" approximated electric field solution obtained in $\bar{\Omega}$ as E^1 and a "second" (higher order) field solution as E^2 . (Note that $\bar{\Omega}$ is the closure of Ω , i.e. the domain Ω and its boundary Γ^{N_1}). The ERM will be applied after solution E^1 has been calculated and yields an estimate of the **relative** FE/BEM electric field error:

$$E^{12} = E^2 - E^1 \quad (9)$$

The above mentioned error will be quantified in terms of a norm (as required by the ERM). For static electric field problems an appropriate norm is the energy norm [19] which yields a quantitative error value of the stored energy in the region under consideration. For electromagnetic problems a similar norm *associated* [16, pp.248] with the stored electric and magnetic energy in the closed region $\bar{\Omega}$ will be employed. This norm will be called the electromagnetic energy norm (EM-norm) and is given by [16, pp.249]:

$$(\|E^{12}\|_{\bar{\Omega}}^{EM})^2 = \sum_{k=1}^M (\|E^{12}\|_{\Omega_k}^{EM})^2 \quad (10)$$

with M the number of finite elements and

$$(\|E^{12}\|_{\Omega_k}^{EM})^2 = \int_{\Omega_k} \left(\text{Re}\left\{\frac{1}{\mu_r}\right\} |\nabla E^{12}|^2 + \text{Re}\{\epsilon_r k_0\} |E^{12}|^2 \right) d\Omega_k \quad (11)$$

the local EM-norm associated with finite element Ω_k .

The ERM will thus yield a quantitative error estimate of the stored electric and magnetic energy in the region

$\bar{\Omega}$. This error estimate will be denoted by $(\|\Phi^{12}\|_{\bar{\Omega}}^{EM})^2$. The EM-norm satisfies the requirements for a norm generated by an inner product [16, pp.246] and is **not** unique for ERM error estimates applied to electromagnetic problems. Other norms could be developed and might lead to improved error estimate results. It will however be shown that the EM-norm introduced here results in reliable ERM error estimates for FE/BE method solutions of general (2D) electromagnetic problems (including problems involving lossy materials).

3.1.1 Local ERM error estimates

An estimate, $(\|\Phi^{12}\|_{\Omega_k}^{EM})^2$, of the **actual** error $(\|E^{12}\|_{\Omega_k}^{EM})^2$ in each finite element, Ω_k , can be obtained by solving the following local problem [10, pp.129][20][16], related to the EM-norm (a sub- or superscript k denotes that a quantity is associated with finite element Ω_k):

$$\begin{aligned} \int_{\Omega_k} \left(\text{Re}\left\{\frac{1}{\mu_r^k}\right\} \nabla \Phi_k^{12} \cdot \nabla v^{12} + \text{Re}\{\epsilon_r^k k_0\} \Phi_k^{12} v^{12} \right) d\Omega_k = \\ \int_{\Omega_k} r_k^1 v^{12} d\Omega_k + \frac{1}{2} \sum_{l=1}^3 \int_{\Upsilon_{k(l)}} \left\{ \frac{\partial E_k^1}{\partial n_{k(l)}} \right\} v^{12} d\Upsilon_{k(l)} + \\ \int_{\Upsilon_k \cap \Gamma^{N_1}} \left(g_1 - \frac{\partial E_k^1}{\partial n_k} \right) v^{12} d\Upsilon_k \quad \text{for all } v_k^{12} \end{aligned} \quad (12)$$

In this equation v_k^{12} is the weighting functions on Ω present in the FE/BEM solution E^2 but not in the solution E^1 . $\Upsilon_{k(l)}$ is the side of the triangular finite element Ω_k connecting Ω_k with its l^{th} neighboring element $\Omega_{k(l)}$. Also, r_k^1 is the local element residual of the governing equation (equation 1) associated with E^1 , with

$$r_k^1 = -\nabla \cdot \frac{1}{\mu_r^k} \nabla E_k^1 - \epsilon_r^k k_0^2 E_k^1 \quad (13)$$

$\left\{ \frac{\partial E_k^1}{\partial n_{k(l)}} \right\}$ is the jump in normal derivative between element Ω_k and its neighboring element, element $\Omega_{k(l)}$, with

$$\left\{ \frac{\partial E_k^1}{\partial n_{k(l)}} \right\} = \left(\frac{1}{\mu_r^{k(l)}} \frac{\partial E_{k(l)}^1}{\partial n_{k(l)}} - \frac{1}{\mu_r^k} \frac{\partial E_k^1}{\partial n_{k(l)}} \right) \quad (14)$$

Equation 12 appears formidable but can be written in the following matrix form for each finite element, Ω_k [16, pp.103]:

$$[S^{k(12)}][\Psi^{k(12)}] = [F^{k(12)}] \quad (15)$$

with $[S^{k(12)}]$ a square matrix with matrix elements which can be calculated using the integral on the left hand side

of equation 12; $[\Psi^{k(12)}]$ is a column matrix with matrix elements the unknown local error estimate coefficients; $[F^{k(12)}]$ is a column matrix with matrix elements which can be calculated using the integrals on the right hand side of equation 12. The elements of $[S^{k(12)}]$ can be computed rapidly using tables for the result of integration over a prototypical element along the lines of [17, Chapter 4]. (Details are given in [16, Appendix F]). Solving the local matrix equation, equation 15, is equivalent to solving the local element residual error estimate equation, equation 12, yielding Φ_k^{12} and thus the local error estimate $(\|\Phi^{12}\|_{\Omega_k}^{EM})^2$. Note that equation 15 is a very "small" matrix equation involving only one finite element (at a time). This equation can thus be solved within negligible computational time.

The specific form of equation 12 is important to ensure the following relation between the global error estimate, Φ^{12} , and actual global error in the EM-norm [20][10, pp.126,pp128]:

$$\|\bar{E}^{12}\|_{\Omega}^{EM} \leq C^{12} \|\Phi^{12}\|_{\Omega}^{EM} \quad (16)$$

with C^{12} the global error estimate inequality constant for the error estimate Φ^{12} in the EM-norm. It is obvious that the accuracy of the global error estimate depends on the value of the constant C^{12} in equation 16. C^{12} is dependent on the order of the basis functions used as well as the shape of the finite elements. In practice $C^{12} = 1$ is assumed with all error estimates. A better approximation of C^{12} would, however, improve the accuracy of the error estimates [10, pp.129][8].

A discussion of the contribution of each term of equation 12 to the error estimate will now follow. This should give a qualitative understanding of the ERM and specifically its application to EM problems.

The weighted residual integral term

The first term on the right hand side of equation 12 is a weighted residual term. The "first" solution E^1 results in a field solution E_k^1 in element Ω_k . The residual r_k^1 will be zero everywhere in Ω_k , if E^1 is the true (or exact) field solution. This is due to the fact that equation 13, with $r_k^1 = 0$, is a form of the governing equation which will be satisfied by the true field solution. If E^1 is an approximate finite element solution the residual r_k^1 will be non-zero and can, in general, vary in numerical value over the finite element Ω_k . The numerical value of the weighting functions, v_k^{12} , on Ω_k is zero at all nodal points on Ω_k associated with the basis functions of the solution E^1 . The numerical value of v_k^{12} on Ω_k is one at all the nodal points on Ω_k associated with the solution E^2 , but not with the solution in E^1 . At non-nodal points v_k^{12} is a value between zero and one varying to the order

of the basis functions used with E^2 . Multiplication of the residual r_k^1 with v_k^{12} and integration over Ω_k is thus equivalent to weighting the residual with v_k^{12} over Ω_k . This weighted term will thus have a relatively large numerical value if the residual is, on average, large in the regions where the "new" nodal points, corresponding to the "new" basis functions of E^2 on Ω_k , will be situated. The weighted term will have a small numerical value if the residual is, on average, small in the regions where the "new" nodal points, corresponding to the "new" basis functions of E^2 on Ω_k , will be situated.

Weighted normal derivative continuity integral term

The second integral term on the right hand side of equation 12 is a weighted normal derivative continuity term on $\Upsilon_{k(l)}$. If E^1 is the true field solution, continuity between the terms $\frac{1}{\mu_k^{(l)}} \frac{\partial E_k^1(l)}{\partial n_{k(l)}}$ and $\frac{1}{\mu_k^*} \frac{\partial E_k^1}{\partial n_{k(l)}}$ of equation 14 must hold on $\Upsilon_{k(l)}$. This continuity requirement is related to the zero divergence requirement [21, pp.127]. This means that $\left\{ \frac{\partial E_k^1}{\partial n_{k(l)}} \right\}$ of equation 14 must be zero for E^1 a true field solution. The different local basis functions (or approximation functions) in each finite element Ω_k result in discontinuities on $\Upsilon_{k(l)}$ for E^1 an approximate finite element solution. In the integral of equation 12, $\left\{ \frac{\partial E_k^1}{\partial n_{k(l)}} \right\}$ can, in general, vary on $\Upsilon_{k(l)}$. The term $\left\{ \frac{\partial E_k^1}{\partial n_{k(l)}} \right\}$ is weighted by the restriction of the v_k^{12} to $\Upsilon_{k(l)}$.

Weighted Neumann boundary condition integral term

The third integral on the right hand side of equation 12 is a weighted Neumann boundary condition integral on $\Upsilon_k \cap \Gamma^{N_1}$. The Neumann boundary condition will be satisfied exactly with E^1 the true field solution, making the quantity $\left(g_1 - \frac{\partial E_k^1}{\partial n_k} \right) \Big|_{\Upsilon_k \cap \Gamma^{N_1}}$ zero. If E^1 is an approximate finite element solution, the Neumann boundary condition on $\Upsilon_k \cap \Gamma^{N_1}$ will be satisfied approximately and the term $\left(g_1 - \frac{\partial E_k^1}{\partial n_k} \right) \Big|_{\Upsilon_k \cap \Gamma^{N_1}}$ will be non-zero. In the integral of equation 12, $\left(g_1 - \frac{\partial E_k^1}{\partial n_k} \right) \Big|_{\Upsilon_k \cap \Gamma^{N_1}}$ can, in general, vary on $\Upsilon_k \cap \Gamma^{N_1}$. The term $\left(g_1 - \frac{\partial E_k^1}{\partial n_k} \right) \Big|_{\Upsilon_k \cap \Gamma^{N_1}}$ is weighted with the restriction of v_k^{12} to $\Upsilon_k \cap \Gamma^{N_1}$.

3.2 Error Estimates for the BEM

In this section, two L^2 -norm [6, pp.50,72] error estimates for the FE/BE method solution, E^1 , will be introduced. Both error estimates are associated with the accuracy

of the field solution on Γ^{N_1} , and are related to **global** field and field derivative errors on Γ^{N_1} . These error estimates are estimates of the “true” errors; that is the errors in E^1 relative to the true field solution [14, 15]. Boundary errors appear to have been seldom used in computational electromagnetics as a measure of solution accuracy; the only example we are aware of is [22], which includes plots of the tangential electric (error) field along a wire antenna.

3.2.1 The boundary field L^2 -norm residual error estimate

The first L^2 -norm error estimate is associated with the accuracy with which the boundary element approximation functions can approximate the actual fields on the boundary Γ^{N_1} . The FE/BE method solution yields field and field derivative coefficients which, together with the boundary element basis functions, can be used to approximate the fields and field derivatives on Γ^{N_1} . These field approximations can be used to calculate the fields at any point in the exterior region Λ , using a numerical approximation of Huygens’ principle [16, pp.57]. The field approximations can also be used to calculate the fields on Γ^{N_1} using the following equation [14, pp.40]:

$$\begin{aligned} \bar{E}^1(\vec{r}_o) = & 2 \int_{\Gamma^{N_1}(\vec{r}_s)} \left[E^1(\vec{r}_s) \frac{\partial \Psi(\vec{r}_o, \vec{r}_s)}{\partial n'(\vec{r}_s)} \right. \\ & \left. - \frac{\partial \bar{E}^1(\vec{r}_s)}{\partial n'(\vec{r}_s)} \Psi(\vec{r}_o, \vec{r}_s) \right] d\Gamma^{N_1}(\vec{r}_s) \\ & + 2E^{inc}(\vec{r}_o) \end{aligned} \quad (17)$$

On the boundary, the FE/BE formulation ensures that $\bar{E}^1(\vec{r}_s) = E^1(\vec{r}_s)$ and they can be used interchangeably here. The quantities \vec{r}_o and \vec{r}_s are the BEM observation and source points on Γ^{N_1} , $\Psi(\vec{r}_o, \vec{r}_s)$ is the 2D homogeneous Green’s function and $E^{inc}(\vec{r}_o)$ is the incident electromagnetic field value at \vec{r}_o . $\bar{E}^1(\vec{r}_o)$ is the approximated field on Γ^{N_1} calculated using equation 17.

A boundary field residual can now be defined as⁵:

$$\bar{R}_{\Gamma^{N_1}}^1(\vec{r}_o) = E^1(\vec{r}_o) - \bar{E}^1(\vec{r}_o) \quad (18)$$

with $\bar{R}_{\Gamma^{N_1}}^1(\vec{r}_o)$ the BEM residual for the FE/BE method field solution, $E^1(\vec{r}_o)$, at \vec{r}_o , on Γ^{N_1} .

⁵Note that $E^1(\vec{r}_o)$ is the approximate field solution (at \vec{r}_o on Γ^{N_1}) obtained with the “first” FE/BE solution. The function $E^1(\vec{r}_o)$ is thus of order equal to the order of the FEM and BEM basis functions. The function $\bar{E}^1(\vec{r}_o)$ is also an approximated field solution (at \vec{r}_o on Γ^{N_1}) obtained with equation 17 (and thus indirectly from the “first” FE/BE method solution). The function $\bar{E}^1(\vec{r}_o)$ is of much higher order than $E^1(\vec{r}_o)$ due to the presence of the Green’s function, $\Psi(\vec{r}_o, \vec{r}_s)$, and the incident field function, $E^{inc}(\vec{r}_o)$, in equation 17.

A global boundary field L^2 -norm residual error estimate can be obtained using equation 18:

$$\|\bar{\Theta}_{\Gamma^{N_1}}^1\|_{L^2}^2 = \int_{\Gamma^{N_1}} |\bar{R}_{\Gamma^{N_1}}^1(\vec{r}_o)|^2 d\Gamma^{N_1} \quad (19)$$

It is evident that the residual $\bar{R}_{\Gamma^{N_1}}^1(\vec{r}_o)$ will be zero if E^1 is the true field solution and $\frac{\partial \bar{E}^1(\vec{r}_s)}{\partial n'(\vec{r}_s)}$ is the true field derivative solution on Γ^{N_1} , for then the approximate fields, $E^1(\vec{r}_o)$ and $\bar{E}^1(\vec{r}_o)$ will both be equal to the true field solution at \vec{r}_o . From equation 19 it is also evident that the boundary field error estimate, $\|\bar{\Theta}_{\Gamma^{N_1}}^1\|_{L^2}^2$, will be zero if E^1 is the true solution. Asymptotic exactness and upper and lower bounds for the error estimate $\|\bar{\Theta}_{\Gamma^{N_1}}^1\|_{L^2}^2$ have not yet been obtained for general FE/BE method solutions (although this has been done for some special cases [14, pp.56]) mainly due to the difficulties arising from the non-local nature of the BEM when applied to general electromagnetic problems.

Typically, this error estimate, which indicates the degree of accuracy of the BEM part of the solution, converges more rapidly than the FEM error estimates, as will be seen in the examples given in §3.4. However, it remains a useful estimate and is required for the far-field error indicators to be developed in §3.3.

3.2.2 The boundary field derivative L^2 -norm residual error estimates

Procedures similar to those described in the previous subsection can be followed to obtain a BEM residual for the FE/BE method field derivative solution [16, pp.106]:

$$\bar{R}_{\Gamma^{N_1}}^1(\vec{r}_o) = \frac{\partial \bar{E}^1(\vec{r}_o)}{\partial n'(\vec{r}_o)} - \frac{\partial \bar{E}^1(\vec{r}_o)}{\partial n'(\vec{r}_o)} \quad (20)$$

$\frac{\partial \bar{E}^1(\vec{r}_o)}{\partial n'(\vec{r}_o)}$ is the normal derivative of $\bar{E}^1(\vec{r}_o)$ of equation 17. The first term on the right of equation 20 is the field derivative computed using the BEM part of the solution (and has the same order of accuracy as the FEM part, since the BEM expands both the field and field derivative to the same order); the second term is computed numerically using the Green’s function of equation 17.

A residual for the FE/BE method **Neumann boundary condition** is [16, pp.108]:

$$\bar{R}_{\Gamma^{N_1}}^1(\vec{r}_o) = \frac{\partial E^1(\vec{r}_o)}{\partial n'(\vec{r}_o)} - \frac{\partial \bar{E}^1(\vec{r}_o)}{\partial n'(\vec{r}_o)} \quad (21)$$

This estimate differs subtly from that in equation 20, in that the residual $\tilde{R}_{\Gamma^{N_1}}^1(\vec{r}_o)$ is the difference (at \vec{r}_o , and on Γ^{N_1}) between the normal field derivative of $E^1(\vec{r}_o)$, obtained by numerically differentiating the FEM part of the solution, and the normal field derivative obtained explicitly from the BEM part of the solution (whereas the estimate of equation 20 is the difference between the solution obtained directly with the BEM and that obtained indirectly from the BEM via the Green's function integral of equation 17). The terms in equation 21 differ due to the indirect enforcement of the Neumann boundary conditions — see section 2.3 — and the different orders of approximation functions (the field derivative solution computed with the FEM is of one order less than that computed with the BEM).

Explicit numerical results for these estimates will not be given in this paper, but these estimates are used in §3.3 and implicitly contained in the results presented in §3.4 and have thus been defined here.

3.3 Far-field error indicators

The FE/BE method solution results in approximate values for the field and field derivatives on the boundary Γ^{N_1} . From this one can calculate the field value at any point (in the near, intermediate or far-field) in the exterior region, Λ , using a numerical approximation of Huygens' principle [16, pp.57] (the exterior BEM equation).

A far-field residual quantity can be defined as:

$$R^1(\vec{r}_o) = \int_{\Gamma^{N_1}(\vec{r}_s)} \left[\tilde{R}_{\Gamma^{N_1}}^1(\vec{r}_s) \frac{\partial \Psi(\vec{r}_o, \vec{r}_s)}{\partial n'(\vec{r}_s)} - \tilde{R}_{\Gamma^{N_1}}^1(\vec{r}_s) \Psi(\vec{r}_o, \vec{r}_s) \right] d\Gamma^{N_1}(\vec{r}_s) \quad (22)$$

where the residuals of equations 18 and 21 have been substituted into the BEM equation in the place of $E^1(\vec{r}_s)$ and $\frac{\partial E^1(\vec{r}_s)}{\partial n'(\vec{r}_s)}$, respectively. $\tilde{R}_{\Gamma^{N_1}}^1(\vec{r}_s)$ of equation 20 can be used instead of $\tilde{R}_{\Gamma^{N_1}}^1(\vec{r}_s)$, but the indicator would then be related to the accuracy of only the BEM part of the FE/BE method solution.

The far-field residual $R^1(\vec{r}_o)$ will be zero if E^1 is the true solution, for then both residuals, $\tilde{R}_{\Gamma^{N_1}}^1(\vec{r}_s)$ and $\tilde{R}_{\Gamma^{N_1}}^1(\vec{r}_s)$, used in the above equation, will be zero.

A radar-width error indicator can now be calculated using the far-field residual, $R^1(\vec{r}_o)$, in the radar-width equation [16, pp.57] instead of $E^{1(sca)}(\vec{r}_o)$:

$$\check{\gamma}(\phi) = 2\pi |\vec{r}_o| \left| \frac{R^1(\vec{r}_o)}{E^{inc}} \right|^2 \quad (23)$$

A radiation intensity error indicator can also be calculated using the far-field residual, $R^1(\vec{r}_o)$, in the radiation intensity equation [16, pp.109] instead of $E^{1(rad)}(\vec{r}_o)$:

$$\check{K}(\phi) = 2\pi |\vec{r}_o| |R^1(\vec{r}_o)|^2 \quad (24)$$

These error indicators estimate the possible error in the radar-width and radiation intensity due to the errors in the approximate FE/BE method field, E^1 , and field derivative solution. Both these error indicators will be zero if E^1 is the true field solution.

3.4 Numerical Results

The error estimates and error indicators formulated in the previous sections have been applied to a variety of electromagnetic problems, with promising success [16]. Two examples will be considered in this section. It will be shown that a combination of the different error estimates and indicators can be used as a reliable *a posteriori* estimate of the accuracy and convergence of FE/BE method solutions.

3.4.1 A Scattering Example

The first numerical example which will be considered is for electromagnetic scattering from the lossy (using practical material parameters) dielectric right-circular cylinder of figure 2 excited by a TE_z polarized, plane incident field at a frequency of 2 GHz. (The TE_z error estimates are analogous to the TM_z estimates given in the preceding sections). Local error estimates and actual errors are compared with each other in figures 4 and 5⁶. In table 1 percentage global estimated errors (in the appropriate norms) are compared to actual percentage errors. Note that in tables 1 and 3, percentage estimated and actual errors of more than 100% are denoted by >100%. Percentage error estimates are, in general, not much larger than 100%, even if the actual percentage error is much larger than 100%. A percentage error near 100% does, however, indicate that the solution at hand is not at all close to the true, or converged, solution. It is evident that the global EM-norm error estimate is a good estimate of the actual error. The global percentage error estimates compare reasonably well with the actual global percentage errors. Important to note is that the

⁶The finite element numbers in all the "local EM-norm error comparison" figures in this section have been arranged in such a way that the corresponding actual EM-norm error values are presented in increasing order. The error estimate values plotted are local EM-norm error estimate values in the corresponding finite elements.

global EM-norm error estimate clearly identifies the solutions which are not at all close to convergence, and gives a reasonably accurate estimate of the percentage errors for the solutions which are close to convergence or have converged to the true solution.

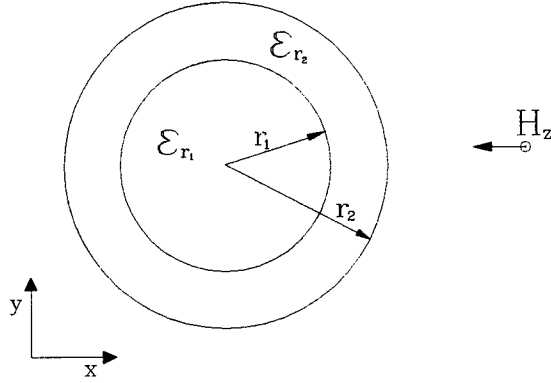


Figure 2: Double dielectric right-circular cylinder ($\epsilon_{r1} = 1.2 + j1.5$, $\epsilon_{r2} = 1.5 + j2$, $r_1 = 0.2m$, $r_2 = 0.3m$). The cylinder is excited by a plane wave incident field with TE_z polarization. (Note that the time convention is $e^{-j\omega t}$.)

A “dB” error margin can be defined as:

$$\Delta\check{\gamma}(\phi) = 10|\log\{\gamma(\phi)\} - \log\{\gamma(\phi) - \check{\gamma}(\phi)\}| \quad (25)$$

where $\gamma(\phi)$ is the radar-width calculated using the FE/BE method and $\check{\gamma}(\phi)$ is the far-field error indicator of equation 23. Notice that $\check{\gamma}(\phi)$ and thus $\Delta\check{\gamma}(\phi)$ will be zero if E^1 is the true field solution.

The “dB” error margin for the first and second order FE/BE method solutions of the radar-width of the scattering problem under consideration are shown in figure 6. The first and second FE/BE method solution as well as the analytical solution of the radar-width are also shown.

All error estimates and error indicators indicate that the second order basis function FE/BE method solution for $M = 1502$ ($M/\lambda^2 = 67$) and $M_b = 90$ ($M_b/\lambda = 5.4$) has converged to an acceptably accurate solution (a maximum field error in the FEM region of around 5% and in the radar-width of 0.1dB). This is confirmed by the actual errors and the radar-width results presented. These error estimates and error indicators have been obtained within negligible computational times (see table 2) compared to the computationally expensive FE/BE method solutions. This is especially true for the FE/BE method

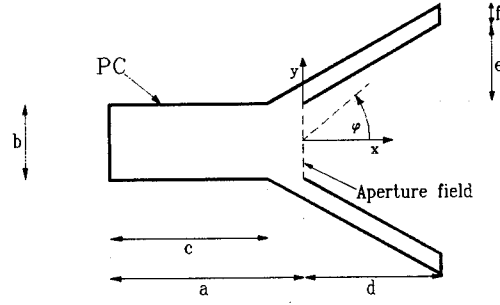


Figure 3: Radiating 2D horn antenna, with $a = 0.55m$, $b = 0.2m$, $c = 0.45m$, $d = 0.35m$, $e = 0.2m$ and $f = 0.05m$.

solutions concerning second and third order basis functions and relatively large numbers of finite and boundary elements.

3.4.2 A Radiation Example

The second numerical example which will be considered is for electromagnetic radiation from the 2D horn antenna of figure 3. The horn antenna is excited by the TE_1 mode aperture field (frequency: 750 MHz):

$$E_z = E_0 \cos\left(\frac{\pi y}{b}\right) \quad (26)$$

Local error estimates and actual errors are compared with each other in figures 7 and 8 and it is again evident that these local error estimates clearly identify the regions where the largest EM-norm errors occur. In table 3, percentage estimated errors (in the appropriate norms) are compared to actual percentage errors. The L^2 -norm boundary field error estimates indicate that enough boundary elements are used to approximate the fields on the boundary for all values of M_b considered. This is even true for $M_b = 35$ ($M_b/\lambda = 4.5$) with first order boundary element basis functions. (Note that in this case the error estimates show that enough boundary elements were used. The actual errors are quite large due to the fact that too few finite elements were used). The EM-norm ERM error estimates indicate that the second order basis function FE/BE method solution for $M = 859$ ($M/\lambda = 145$) and $M_b = 76$ ($M_b/\lambda = 9.8$) has

converged to a satisfactorily accurate FE/BE method solution. (This corresponds to around 100 elements per square wavelength). This is confirmed by the actual EM-norm errors.

A “dB” error margin for the FE/BE method solution of the radiation intensity can be obtained using the radiation intensity error indicator of equation 24. This error margin, denoted by $\Delta\check{K}(\phi)$, can be calculated as (this is similar to the radar-width error margin of equation 25):

$$\Delta\check{K}(\phi) = 10|\log\{K(\phi)\} - \log\{K(\phi) - \check{K}(\phi)\}| \quad (27)$$

Note that $\check{K}(\phi)$ and thus $\Delta\check{K}(\phi)$ will again be zero if E^1 is the true field solution. The “dB” error margins for the second and third order FE/BE method solutions of the radiation intensity of the problem under consideration are shown in figure 9. The second and third order FE/BE method solutions, as well as the converged solution of the radiation intensity are also shown.

It should be kept in mind that the local error estimates, obtained with equation 12, are dependent on: the frequency and polarization of the incident electromagnetic field; the field values in the finite element under consideration; the order of the approximation functions in the finite element under consideration; the shape of the finite element under consideration; the accuracy of the “first” FE/BE method solution E^1 ; and finally, the accuracy with which the fields on the boundary Γ^{N_1} are approximated by the BEM part of the FE/BE method solution E^1 . The global error estimate is dependent on all local error estimates and the size of the finite element region under consideration.

Bearing all this in mind it is evident that the local and global ERM error estimates are, in general, acceptably accurate estimates of the actual local and global errors. Some of these above mentioned factors can be taken into account to improve the local and global error estimates [16, pp.143] [10, pp.129][8]

The results also indicate that the boundary field L^2 -norm residual error estimate, $\|\hat{\Theta}_{\Gamma^{N_1}}^1\|_{L^2}^2$ is not a good quantitative estimate of the boundary field error. This is due to the fact that this error estimate is a measure of the error in the boundary field for the BEM part of the FE/BE method solution, without consideration of the actual coupling to the FEM part of the solution. The **actual** boundary field error is, however, dependent on the FEM and BEM part of the FE/BE method solution. *As such, the boundary error estimates must be used in conjunction with the FEM error estimates.*

Only when the FEM part of the solution is of accept-

able accuracy and the BEM part is highly inaccurate is this L^2 -norm error estimate an accurate quantitative estimates of the boundary field error. This would occur if enough finite element basis functions but insufficient boundary element basis functions had been used — this has not occurred in the examples given in this paper.

It is evident from the far-field error indicator results (figures 6 and 9) that, *used together*, the error margins and error indicators can be very useful in determining the accuracy of FE/BE method radar-width or radiation intensity solutions.

4 Conclusions

The variational boundary-value problem formulation of the coupled FE/BE method for application to general 2D open boundary electromagnetic problems has been presented. This formulation has been developed over the past few decades and has been used successfully by engineers for numerically solving previously intractable electromagnetic problems. (This work is not new but was required as a basis for the rest of the paper.)

ERM local and global error estimates, L^2 -norm boundary field error estimates and far-field error indicators have been developed and investigated. This was done for 2D FE/BE method solutions of electromagnetic scattering as well as radiation problems. The global EM-norm ERM error estimate results obtained for electromagnetic scattering and radiation problems were not as accurate as the ERM energy norm error estimates for static electric field problems [19] [16, pp.126]. This is due to a number of factors, including the dependency of the EM-norm error estimates on the frequency of the electromagnetic field, the dependency on the accuracy of the coupling of the BEM with the FEM, and the non-local nature of electromagnetic fields. It was, however, shown that the EM-norm error estimates provide valuable post-processed information regarding the accuracy and convergence of the FE/BE method solutions. This was shown to be true for electromagnetic radiating as well as scattering problems of arbitrary shaped (lossy and lossless) objects [16]. The local EM-norm ERM error estimate results obtained show that the estimated error distributions in the FEM region compared satisfactorily with the actual error distributions. Further investigation could lead to improvement of the local as well as global EM-norm ERM error estimates. (Improved element residual error estimate methods, for non-electromagnetic problems, have already been developed [9, 20] and seem to work well).

Results presented have show that the boundary **field**

L^2 -norm error estimate is not a quantitatively accurate boundary field error estimate for the FE/BE method solution, in particular when the FEM part of the solution is considerably in error. This is because the BEM part of the solution may be accurately matching an inaccurate FEM solution at the boundary. The boundary error estimate must not be considered in isolation, but with due cognisance of the FEM error as well.

The radar-width and radiation intensity error indicators, developed for the FE/BE method solutions, were used to obtain "dB" error margins which proved to provide exceptionally useful post-processed radar-width and radiation intensity error information. (These do incorporate, via the boundary field derivative error estimates, information about the accuracy of the FEM part of the solution as well). We should comment that Lee in particular has recently emphasized the role of "global" errors, caused by dispersion error: we have not considered this here [23].

It was also shown that all these error estimates and indicators can be obtained within negligible computational times compared to the computational times of the FE/BE method solutions. This is due to the nature of the error estimate and error indicator methods as well as the highly efficient algorithms employed [16].

Adaptive finite element methods are closely linked to *a posteriori* error estimates and could be used to improve the efficiency of general FEM solutions. The *a posteriori* error estimate methods can be used to identify the regions where the fields need to be approximated more accurately (for example where the fields vary more rapidly), and the finite element mesh can thus be adapted to ensure superior basis function distributions in these regions [10]. Although not shown in this paper, the authors have also worked on this topic [16, pp.168].

In conclusion: the *a posteriori* error estimates and indicators show great promise, but can still be improved upon. It can also be extended to *a posteriori* error estimates for 3D FE/BE method solutions. The use of edge-based elements for 3D formulations would not pose special problems as far as error estimation is concerned, although hierarchical edge-based elements may prove more formidable than the nodal based equivalents if the error estimator is used to drive an adaptive meshing algorithm.

Ultimately one would like to develop a FE/BE method solver with error estimates and indicators which clearly identify the different inaccuracies in the solution at hand and use this information to automatically adapt itself accordingly. Such a solver should provide accuracy and

convergence information to the user providing him with a very useful and reliable tool for solving practical electromagnetic engineering problems. That this problem remains a very pressing one, and in particular that ad-hoc estimates leave much to be desired, is clear from recent work [24]. It is hoped that the more rigorous estimate formulations presented in this paper will contribute to progress in this field.

References

- [1] J. Jin, **The Finite Element Method in Electromagnetics**, John Wiley & Sons, Inc., New York, USA, 1993.
- [2] J. D'Angelo, "Finite Element/Boundary Element Analysis of Electromagnetic Fields," **AP-S Workshop on Differential Equation-Based Finite Methods**, IEEE AP-S Symposium, Syracuse, New-York, June 1988.
- [3] K.L. Wu, G.Y. Delisle, D.G. Fang and M.Lecours, "Coupled Finite Element and Boundary Element Scattering," **Finite Element and Finite Difference Methods in Electromagnetic Scattering, PIER2**, pp.113-132. New York: Elsevier Science Publishing Co., 1990.
- [4] G.Y. Delisle K.L. Wu, J. Litva, "Coupled Finite Element and Boundary Element Method in Electromagnetics," **Computer Physics Communications**, North-Holland, No. 68, pp.255-278, 1991.
- [5] F.J.C. Meyer, **A Hybrid Finite Element/Boundary Element Solutions of General Two Dimensional Electromagnetic Scattering Problems**. Thesis accepted for the degree M.Eng., University of Stellenbosch, 1991.
- [6] B.D. Reddy, **Functional Analysis and Boundary-value Problems: an Introductory Treatment**, Longman Scientific & Technical, Essex, England 1986.
- [7] A.C. Cangellaris, R. Lee, "On the Accuracy of Numerical Wave Simulations Based on Finite Methods," **Journal of electromagnetic waves and applications**, Vol 6, pp.1635-1653, 1992.
- [8] R.E. Bank and A. Weiser, "Some A Posteriori Error Estimators for Elliptic Partial Differential Equations," **Mathematics of Computation**, vol. 44, No. 170, pp. 283-301, April 1985.
- [9] M. Ainsworth and J.T. Oden, "A Unified Approach to A Posteriori Error Estimation using Element Residual Methods," **Numerische Mathematik**, No. 65, pp.23-50, 1993.
- [10] J.T. Oden, L. Demkowicz, W. Rachowicz and T.A. Westermann "Towards a universal h-p adaptive finite element strategy," Part 1, 2 and 3, **Computer methods in applied mechanics and engineering**, North-Holland, No. 77, pp.79-212, 1989.

- [11] Ü. Pekel, R. Lee, "An *A Posteriori* error reduction scheme for the three-dimensional finite element solution of Maxwell's equations" **IEEE Trans. Microwave Theory and Techniques** Vol. 43, No. 2, pp.421-428, February 1995.
- [12] T. Cwik, V. Jamnejad, C. Zuffada, "Comparison of electric and magnetic field formulations in finite element modelling", **Proceedings of 1994 URSI Radio Science Meeting**, Seattle, WA, June 1994, p.406.
- [13] G.C.Hsiao, R.E.Kleinman, "Error control in numerical solution of boundary integral equations", **Applied Computational Electromagnetics Society Journal**, Vol 11, No. 1, pp.32-36, 1996.
- [14] L. Demkowicz, J.T Oden, M. Ainsworth and P. Geng, "Solution of elastic scattering problems in linear acoustics using h-p boundary element methods," **Journal of Computational and Applied Mathematics**, North-Holland, No. 36, pp.29-63, 1991.
- [15] A. Karafiat, J.T Oden, P. Geng, "Variational Formulations and hp-Boundary Element Approximations for Hypersingular Integral Equations for Helmholtz Exterior Boundary-Value Problems in Two Dimensions," **Ticom Report 92-01**, April 1992.
- [16] F.J.C. Meyer, **The Two-Dimensional Finite Element/Boundary Element Method in Electromagnetics: Formulation, Applications, Error Estimates and Mesh Adaptive Procedures**. Thesis accepted for the degree of Doctor of Philosophy in Engineering, University of Stellenbosch, December 1994.
- [17] P.P. Silvester and R.L. Ferrari, **Finite Elements for Electrical Engineers, Second Edition**, *Cambridge University Press*, Cambridge, 1990.
- [18] J.T. Oden, L. Demkowicz, W. Rachowicz and T.A. Westermann "A Posteriori Error Analysis in Finite Elements: The Element Residual Method for Symmetrizable Problems with Applications to Compressible Euler and Navier-Stokes Equations," **Computer methods in applied mechanics and engineering**, North-Holland, No. 82, pp.183-203, 1990.
- [19] F.J.C. Meyer and D.B. Davidson, "Error Estimates and Adaptive Procedures for the Two-Dimensional Finite Element Method", **Electronics Letters**, Vol. 30, No. 12, pp.936-938, June 1994.
- [20] M. Ainsworth and J.T. Oden, "A Procedure for a posteriori error estimation for h-p finite element methods," **Computer Methods in Applied Mechanics and Engineering**, North-Holland, No. 101, pp.73-96, 1992.
- [21] S. Ramo, J.R. Whinnery, T. Van Duzer, **Fields and Waves in Communication Electronics**, second edition. *New York: John Wiley & Sons*, 1984.
- [22] E. K. Miller and F. J. Deadrick, "Some Computational Aspects of Thin-Wire Modeling" in **Topics in Applied Physics, Volume 3: Numerical and Asymptotic Techniques in Electromagnetics**, editor R.Mittra. *New York: Springer-Verlag*, 1975.

$M : M_b$	Field error (estimated & actual)		Boundary field error (estimated & actual)	
	$\frac{\ \Phi^{12}\ ^{EM}}{\ E^1\ ^{EM}}$	$\frac{\ E^{12}\ ^{EM}}{\ E^1\ ^{EM}}$	$\frac{\ \hat{\Phi}_{\Gamma N_1}^1\ _{L_2}^2}{\ E_{\Gamma N_1}^1\ _{L_2}^2}$	$\frac{\ E_{\Gamma N_1}^{12}\ _{L_2}^2}{\ E_{\Gamma N_1}^1\ _{L_2}^2}$
	(%)	(%)	(%)	(%)
E^1 first order approximation functions and E^2 second order approximation functions				
170:24	79.99	>100	>100	51.11
501:43	74.38	79.30	9.39	31.41
977:73	51.42	51.17	0.73	12.49
1502:90	44.09	35.61	0.16	2.99
E^1 second order approximation functions and E^2 third order approximation functions				
170:24	47.99	74.48	2.37	17.50
501:43	11.34	13.38	0.07	0.39
977:73	7.04	7.35	0.01	0.05
1502:90	5.52	4.24	0.00	0.03

Table 1: Percentage error estimates compared to actual errors. This is for scattering from the lossy dielectric right-circular cylinder of figure 2 excited by a TE_z polarized, plane incident field (frequency: 2 GHz). M is the number of finite elements and M_b the number of boundary element used.

- [23] Z. Chen, R. Lee, "Adaptive mesh refinement concepts for electromagnetics" **Proceedings of the 12th Annual Review of Progress in Applied Computational Electromagnetics**, Monterey, CA, p.932-938.
- [24] A.F.Peterson, "Non-rigorous CEM error estimates and their limitations" **Proceedings of the 12th Annual Review of Progress in Applied Computational Electromagnetics**, Monterey, CA, p.1116-1121.

E^1 first order approximation functions and E^2 second order approximation functions

M	Computational time (hours:min:sec)		
	FE/BE method solution		Error estimates
	E^1	E^2	
170	00:00:02	00:00:10	00:00:05
501	00:00:06	00:01:33	00:00:10
977	00:00:23	00:08:59	00:00:21
1502	00:00:42	00:18:28	00:00:29

E^1 second order approximation functions and E^2 third order approximation functions

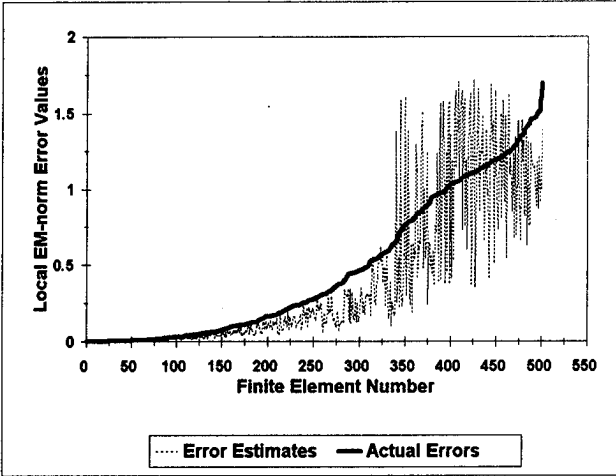
M	Computational time (hours:min:sec)		
	FE/BE method solution		Error estimates
	E^1	E^2	
170	00:00:10	00:01:25	00:00:07
501	00:01:33	00:12:27	00:00:14
977	00:08:59	01:28:58	00:00:29
1502	00:18:28	02:27:31	00:00:40

Table 2: Computational times (on a HP-720 work station) for the FE/BE method solution and error estimates (all error estimates and error indicators combined) for the scattering problem concerning the right circular cylinder in figure 2. M is the number of finite element used.

$M : M_b$	Field error		Boundary field error	
	$\frac{\ \Phi^{12}\ ^{EM}}{\ E^1\ ^{EM}}$	$\frac{\ E^{12}\ ^{EM}}{\ E^1\ ^{EM}}$	$\frac{\ \hat{\Theta}_{\Gamma N_1}^1\ _{L_2}^2}{\ E_{\Gamma N_1}^1\ _{L_2}^2}$	$\frac{\ E_{\Gamma N_1}^{12}\ _{L_2}^2}{\ E_{\Gamma N_1}^1\ _{L_2}^2}$
	(%)	(%)	(%)	(%)
E^1 first order approximation functions and E^2 second order approximation functions				
112:35	79.90	>100	0.04	>100
182:35	68.57	>100	0.05	>100
450:57	52.64	51.76	0.01	42.56
859:76	40.73	36.79	0.00	16.70
E^1 second order approximation functions and E^2 third order approximation functions				
112:35	16.03	57.55	0.00	3.40
182:35	11.74	15.78	0.00	1.78
450:57	10.16	9.63	0.00	0.35
859:76	6.25	5.92	0.00	0.16

Table 3: Percentage error estimates compared to actual errors. This is for the electromagnetic radiation problem concerning the horn antenna of figure 3. Frequency: 750 MHz, Polarization: TE_1 mode aperture source field. M is the number of finite elements and M_b the number of boundary element used.

E^1 first order approximation functions and E^2 second order approximation functions



E^1 second order approximation functions and E^2 third order approximation functions

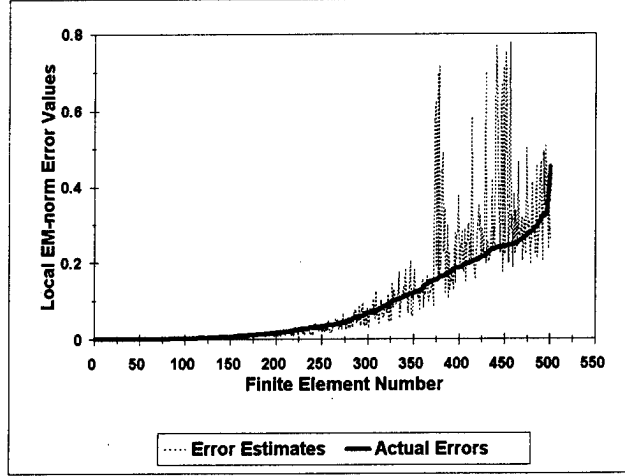
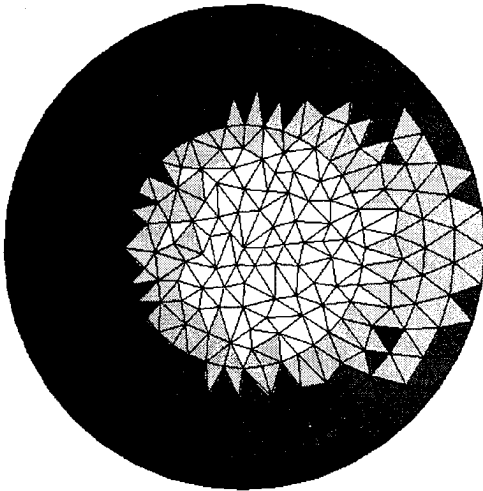


Figure 4: Comparison of estimated and actual local EM-norm error values for the FE/BE method solution of the electromagnetic scattering problem concerning the right circular cylinder of figure 2. The incident electromagnetic field is TE_z polarized at frequency 2 GHz. $M = 501$ is the number of finite elements used.

Estimated Error Distribution



Actual Error Distribution

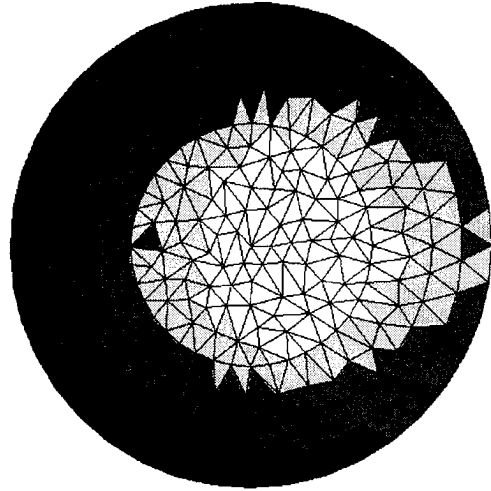


Figure 5: Comparison of estimated and actual local EM-norm error distributions for the FE/BE method solution of the fields in and around the right circular cylinder of figure 2. The incident electromagnetic field is TE_z polarized at frequency 2 GHz. Dark elements indicate high error values and light elements indicate low error values. This is for E^1 second order approximation functions and E^2 third order approximation functions.

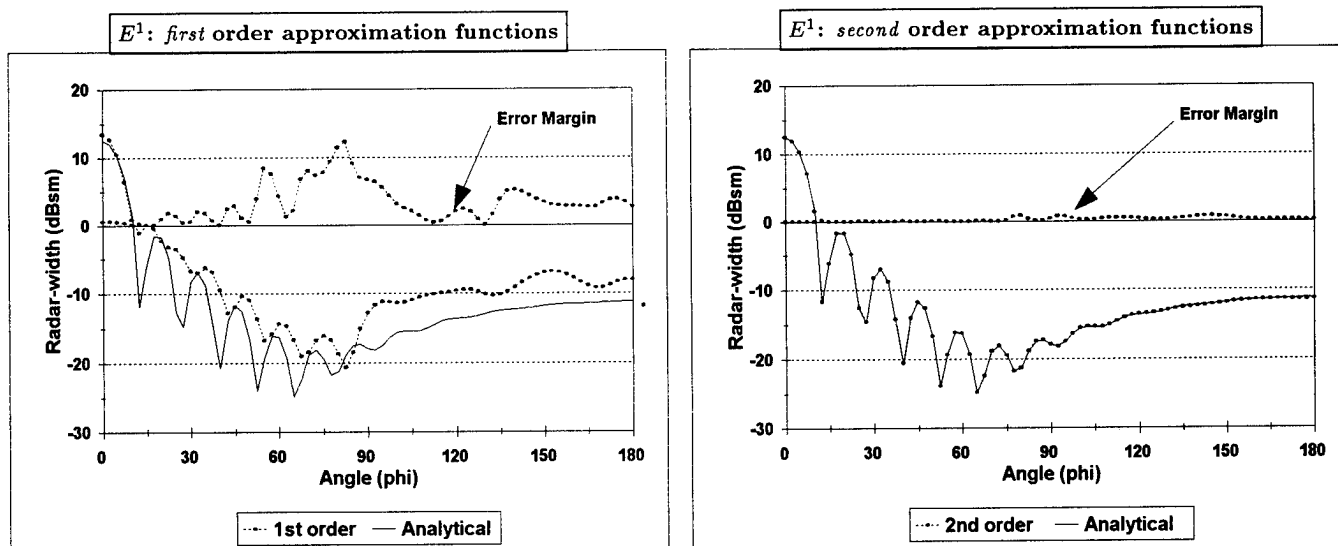
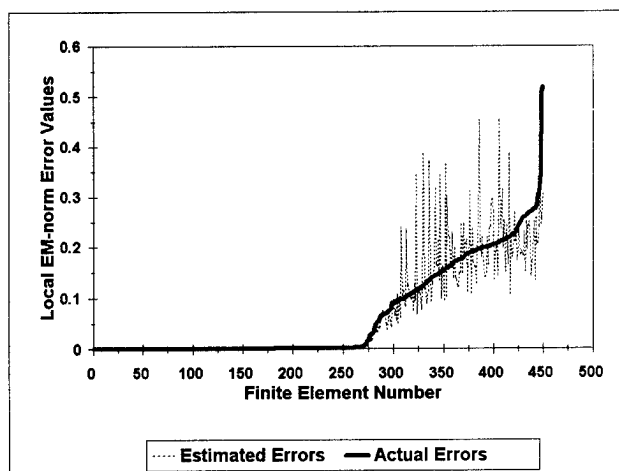


Figure 6: Comparison of the radar-width values, obtained analytically and numerically (FE/BE method solution), for the scattering problem concerning the right circular cylinder in figure 2. The “dB” error margins, $\Delta\gamma(\phi)$, are also shown for first and second order FE/BE solutions. Frequency: 2 GHz. Polarization: TE_z . Number of finite elements used: $M = 1502$. Number of boundary elements used: $M_b = 90$.

E^1 first order approximation functions and E^2 second order approximation functions



E^1 second order approximation functions and E^2 third order approximation functions

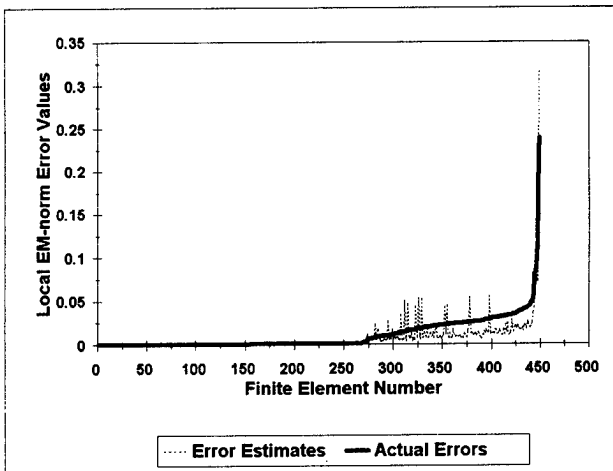


Figure 7: Comparison of estimated and actual local EM-norm error values for the FE/BE method solution of the electromagnetic radiation problem concerning the horn antenna of figure 3. Frequency: 750 MHz, Polarization: TE_1 mode aperture source field. $M = 450$ is the number of finite elements used.

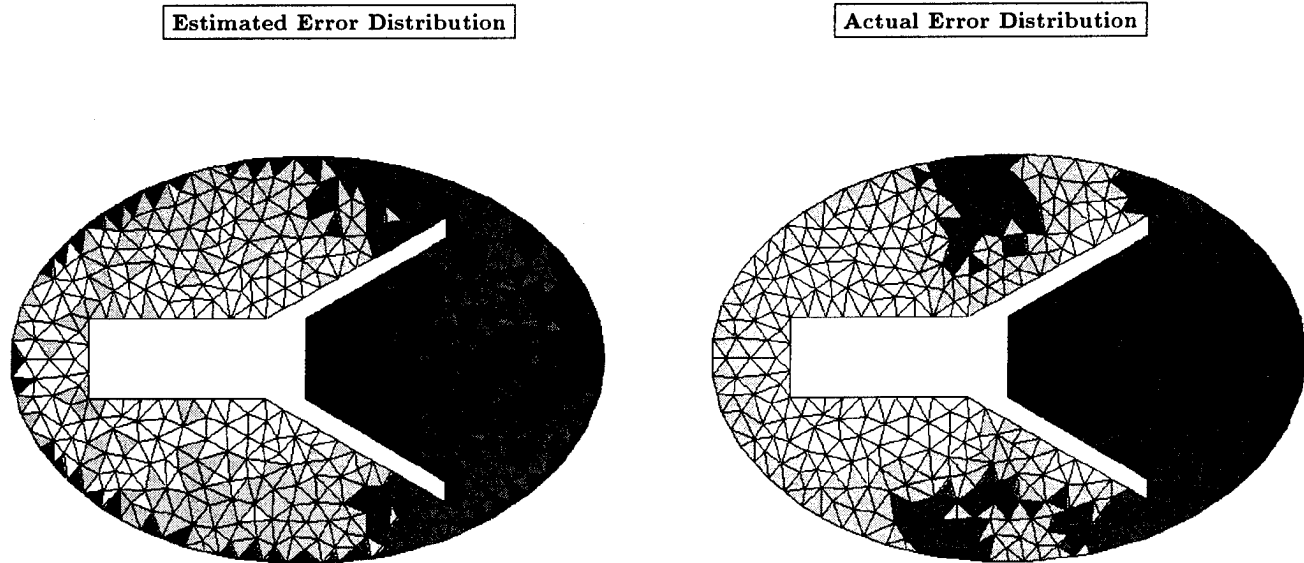


Figure 8: Comparison of estimated and actual local EM-norm error distributions for the FE/BE method solution of the electromagnetic radiation problem concerning the horn antenna of figure 3. Frequency: 750 MHz, Polarization: TE_1 mode aperture source field. Dark elements indicate high error values and light elements indicate low error values. This is for E^1 second order approximation functions and E^2 third order approximation functions.

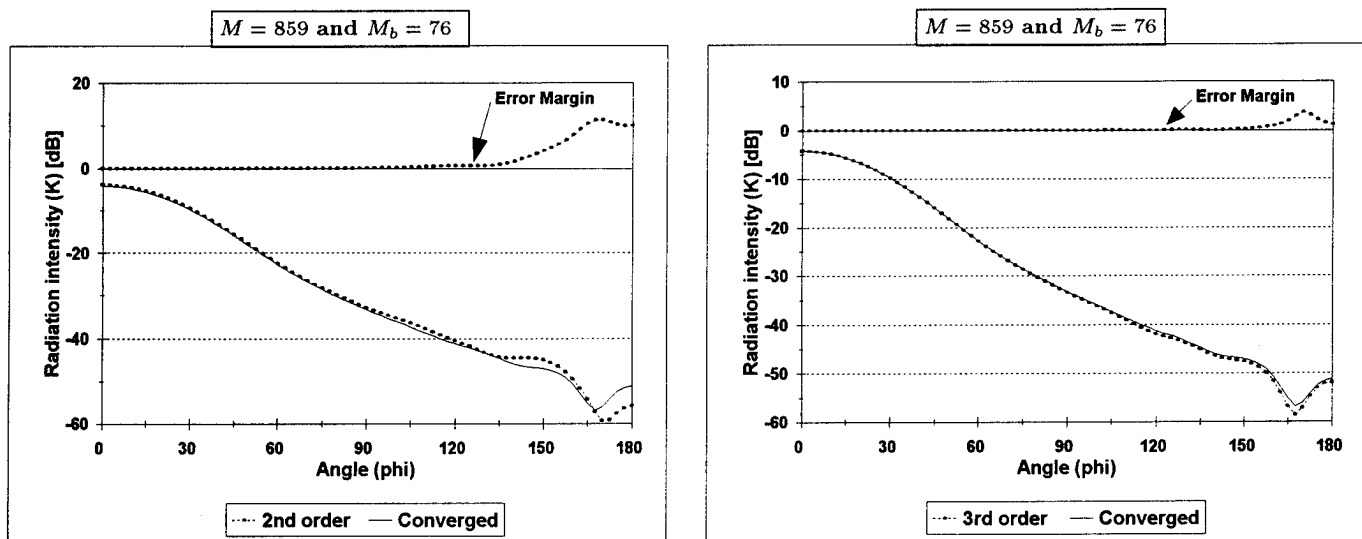


Figure 9: Comparison of the radiation intensity values, obtained numerically (FE/BE method solution), for the radiation problem concerning the horn antenna of figure 3. Second and third order basis function solutions, the converged solution and the “dB” error margins, $\Delta K(\phi)$, are shown. Frequency: 750 MHz, Polarization: TE_1 mode aperture source field. M and M_b are the number of finite elements and boundary elements used respectively.

Modelling of an Arbitrarily-Oriented Mobile Telephone Handset in the Finite-Difference Time-Domain Field Computation Method

P.S. Excell, P. Olley¹ and N.N. Jackson²

Department of Electronic and Electrical Engineering, University of Bradford, U.K.

(¹Now with Department of Mechanical Engineering, University of Bradford. ²Now with School of Electrical Engineering & Science, Cranfield University, Royal Military College of Science, Shrivenham, UK)

ABSTRACT

The implementation of a generic mobile telephone handset model in the Finite Difference Time Domain (FDTD) method for computation of electromagnetic field distributions is described. The handset can be rotated about the principal FDTD axes to achieve any orientation. The 'thin wire' technique is used to model the antenna in a way that ensures that its correct electrical length is maintained despite the 'staircasing' effect of the FDTD grid. Computed predictions from the model agree with near-field measurements on a physical realisation of the handset, and accurate near and far fields are calculated for arbitrary orientations of the handset. It is concluded that this wire rotation technique has broad application to problems involving components that are required to move in relation to fixed structures.

1. INTRODUCTION

Computer modelling of the deposition of electromagnetic energy in the human head offers the opportunity to predict compliance of radiofrequency equipment with safety guidelines. Datasets representing heads, classified into regions with significantly different dielectric properties, have been modelled under irradiation by plane waves and dipoles [1,2] or mobile telephone handsets in simple orientations [3], and solid spheres have been irradiated by handsets [4] and plane waves [5,6]. Work specifically on the incorporation of handsets into FDTD software has been performed by Luebbers et al [7], Toftgard et al [4] and Jensen and Rahmat-Samii [8]. With dipole or handset irradiation, the antenna has almost invariably been oriented parallel to one of the principal FDTD axes, so that its wire (assumed straight) can be correctly represented in the FDTD mesh. However, the standard FDTD methods for representation of wires lead to errors if the antenna is not parallel to a principal axis as the resulting electrical length of the antenna is the sum of a sequence of orthogonal steps along FDTD cells (staircase approximation). In contrast, the physical length of the antenna is the linear distance between the initial and final cells: in general this will be significantly shorter than the FDTD discretised version.

A major consequence of this will be that the resonant frequency of the antenna will tend to be artificially depressed, and orientation-dependent, in the FDTD representation. The technique described below overcomes this limitation, allowing a handset to be located in a realistic orientation near a human head. This capability is vital for determination of the interaction of handsets with human tissue in realistic usage. In particular, realistic handset orientation is necessary to assess the Specific Absorption Rate (SAR) in the human head due to mobile telephones. (It may be noted that Jensen and Rahmat-Samii [8] allowed rotation of the handset relative to the head, but this was done by rotating the head rather than the handset: compensation for variation of the apparent length of resonant conductors was thus avoided).

A discussion of the accuracy that is estimated for the results presented below is given in Appendix 1.

2. THE THIN WIRE METHOD IN FDTD

The established method for representation of thin wires in an FDTD simulation is that suggested by Holland and Simpson [9]. In this technique each element of the antenna runs along an electric field component in a Yee cell [10] to form a continuous path from start to finish of the antenna. At each time step the driven point of the antenna is injected with a current, and the current on the tip of the antenna is maintained at zero.

The time-advance equation for an arbitrary element 'm' of the thin wire, located in cell (x,y,z)=(i,j,k) and pointing along the x-axis, is given by [9]:

$$I(m)^n = I(m)^{n-1} + \Delta t \left\{ \frac{E_x(i, j, k)^{n-1/2}}{L} - \frac{Q(m+1)^{n-1/2} - Q(m)^{n-1/2}}{\epsilon_0 \mu_0 \Delta x_{tw}} \right\} \quad (1)$$

where: $I(m)^n$ = current in wire element m
and $Q(m)^n$ = charge per unit length on wire element m

$E_x(i,j,k)^n$ = x component of electric field in cell (i,j,k)
 (each of the above are for time instant n)
 Δt = FDTD time step
 Δx_{tw} = 'corrected' length of thin-wire segment in x-direction
 L = 'In-cell' inductance per unit length of the wire

The 'in-cell' inductance per unit length of the wire, L , ensures accurate treatment of the inductive fields close to the wire. It is given by [9]:

$$L = \frac{\mu_0}{2\pi} \left(\ln\left(\frac{R}{a}\right) - \frac{1}{2} + \frac{a^2}{2R^2} \right) \quad (2)$$

where a is the wire radius, R is the effective radius of an FDTD cell and $a < R$.

The 'corrected' segment length is found by multiplying the standard FDTD cell size in the x-direction by a correction factor to reduce the 'staircased' conductor length to equal the correct wire length. Elements parallel to the y or z-axes have analogous advance equations. The wire charges are similarly advanced, using:

$$Q(m)^{n+1/2} = Q(m)^{n-1/2} - \frac{\Delta t}{\Delta x_{tw}} (I(m)^n - I(m-1)^n) \quad (3)$$

The electric fields are then updated by the currents, after their normal FDTD advance, by using:

$$E_x(i,j,k)^{n+1/2} = E_x(i,j,k)^{n-1/2} - \frac{\Delta t}{\epsilon_0 \Delta y \Delta z} I(m)^n \quad (4)$$

where Δy and Δz are the standard (not 'corrected') FDTD cell sizes in the y and z directions, Equation (4) being for the case where the wire segment is in the x-direction.

3. IMPLEMENTATION OF ROTATABLE HANDSET

To represent a generic mobile telephone handset, an antenna driven as a monopole and located on a dielectric-coated rectangular box was used. The cell at the base of the antenna was excited by a current of the form $I_0 \sin(\omega t)$ and the charge in this cell was zeroed at each time step. The condition for the cell at the tip of the antenna was that the current be zeroed at each time step.

For a general-purpose model of the interaction between a handset and the human body it is normally most convenient to keep the body components fixed in the co-

ordinate system and vary the orientation of the handset to simulate realistic usage. It is thus necessary to be able to generate a new, arbitrarily rotated, dataset from an existing handset geometry dataset. To define the handset structure it is usually most convenient to commence with the antenna oriented parallel to an axis of the FDTD mesh system (chosen to be the x-axis in the present work). It is convenient to define the origin to be at the base of the antenna: orientation is then defined as a pair of angles, first that for rotation about the z-axis, α , and then that for rotation about the y-axis, β (see Figure 1). This can readily be extended to include an additional rotation about the x-axis if required. The handset problem can then be separated into two distinct areas: rotating the antenna and rotating the handset body.

3.1 Rotatable Antenna

To overcome the problem of excessive electrical antenna length in a 'staircased' FDTD representation, a correction factor was introduced, in which the values of Δx_{tw} (and similarly Δy_{tw} and Δz_{tw}) used in Equations (1) and (3) were modified from the basic FDTD cell size by multiplication by a constant fractional factor f_w :

$$\begin{aligned} \Delta x_{tw} &= f_w \cdot \Delta x \\ \Delta y_{tw} &= f_w \cdot \Delta y \\ \Delta z_{tw} &= f_w \cdot \Delta z \end{aligned}$$

$$\text{where } f_w = \frac{\text{Physical distance from antenna base to tip}}{\text{Staircased distance from base to tip}}$$

In this way the length of the antenna, as used in these equations, was independent of rotation angle.

The 'thin wire' technique requires the use of the above set of time-advance equations (in addition to the standard FDTD time-marching equations) for each cell through which the wire passes. The following algorithm generates the necessary parameters for use in Eqns (1), (3) and (4).

If the base of the antenna is defined as the origin (0,0,0), the end point, $(x_{end}, y_{end}, z_{end})$ is calculated thus:

$$\begin{aligned} x_{end} &= R \cos(\alpha) \cos(\beta) \\ y_{end} &= R \sin(\alpha) \\ z_{end} &= -R \cos(\alpha) \sin(\beta) \end{aligned}$$

where α is the angle rotated about the z-axis, β is the angle then rotated about the y-axis and R is the antenna length. The FDTD cell indices of the base and end of the antenna may then be ascertained.

It is next necessary to calculate the shortest continuous 'staircased' path of electric fields between the two ends, this path following the electric field components in the Cartesian grid of FDTD cells. This may be performed by noting the indices of each new cell traversed by a straight line from base to tip of the antenna. The following examples show how the components and positions of electric fields required to form such a thin wire may be deduced.

If two consecutive cells are denoted by (i,j,k) and $(i+1,j,k)$, then the E_x component located in cell $(i+1,j,k)$ is required to link the two cells. Similarly, the E_x component located in cell (i,j,k) is required to link the consecutive cells $(i-1,j,k)$ and (i,j,k) (see Figure 2). In the cases where two indices change between consecutive cells, the corresponding two electric field components will be needed. For example, a step from cell (i,j,k) to cell $(i+1,j+1,k)$ requires the E_x field component of cell $(i+1,j,k)$ and then the E_y field component of cell $(i+1,j+1,k)$ (see Figure 3). A list of lattice positions and components of the electric fields necessary to step from base to tip of the antenna may thus be deduced. These can then be used directly in Equations (1), (3) and (4) above.

It was found that the formulation of Equations (1) and (4) fails if the chosen direction of conventional positive current flow in the wire segment under consideration is antiparallel to the corresponding unit vector of the co-ordinate system. To cover such cases these equations had to be modified as follows:

$$I(m)^n = I(m)^{n-1} + \delta(m)\Delta t \left\{ \frac{E_x(i,j,k)^{n-1/2}}{L} - \frac{Q(m+1)^{n-1/2} - Q(m)^{n-1/2}}{\epsilon_0 \mu_0 \Delta x_{tw}} \right\} \quad (5)$$

$$E_x(i,j,k)^{n+1/2} = E_x(i,j,k)^{n-1/2} - \delta(m) \frac{\Delta t}{\epsilon_0 \Delta y \Delta z} I(m)^n \quad (6)$$

where $\delta(m) = +1$ if the defined direction of positive current flow in element 'm' is parallel to the unit x-vector, and $\delta(m) = -1$ if the positive current flow direction is defined to be antiparallel to the unit vector.

3.2 Rotatable Handset Body

As shown by Luebbers *et al* [7], the electrical properties of many practical handsets may be realistically represented by an antenna on a metal chassis surrounded by a dielectric (plastics) case. Consider first the metal

chassis oriented with its principal axis parallel to the x-axis as in Figure 1: let the point at which the antenna and chassis meet be defined as position $(0,0,0)$ and let an arbitrary point on the metal chassis be (x_m, y_m, z_m) with reference to this origin. As was the case for the antenna, this point can be rotated by α about the z-axis and then β about the y-axis to get the position after rotation $(x_{rot}, y_{rot}, z_{rot})$. This position is given by calculating the intermediate position (x_1, y_1, z_1) after rotation by α about the z-axis, then calculating the position after a further rotation by β about the y-axis, viz.:

$$\begin{aligned} x_1 &= r_0 \cos(\theta_0 + \alpha) \\ y_1 &= r_0 \sin(\theta_0 + \alpha) \\ z_1 &= z_m \end{aligned}$$

$$\begin{aligned} \text{where } \theta_0 &= \tan^{-1}(y_m/x_m) \\ \text{and } r_0 &= (x_m^2 + y_m^2)^{1/2} \end{aligned}$$

Then:

$$\begin{aligned} x_{rot} &= r_1 \sin(\theta_1 + \beta) \\ y_{rot} &= y_1 \\ z_{rot} &= r_1 \cos(\theta_1 + \beta) \end{aligned}$$

$$\begin{aligned} \text{where } \theta_1 &= \tan^{-1}(z_1/x_1) \\ \text{and } r_1 &= (x_1^2 + z_1^2)^{1/2} \end{aligned}$$

Each point represents a location on the metal chassis after rotation. The lattice cell indicated by each such point is easily calculated and its position must be stored for later use during time stepping. At each time step, the tangential electric field components on the metal surface must be zeroed. In a staircased representation this is achieved by zeroing all three orthogonal components in any cell deemed to contain metal.

Similarly, the dielectric case of the handset may be rotated. In this case it is necessary only to set correct electrical properties for the indicated lattice cells. In general, any dielectric or perfectly conducting metal shape may be rotated in this manner.

4. RESULTS

Numerical tests were undertaken with an FDTD program based on THREDE [11], but using Fang-Mei superabsorbing boundary conditions as the interface to free space [12]. In addition, a near-to-far field transformation algorithm (see below) and the modifications described above were incorporated into the program. The computer was a Sun Sparcstation 10 with 96Mbyte main memory.

4.1 Near Fields

A battery-powered transmitter simulating the generic shape of typical commercial handsets was constructed. This radiated 1.8GHz CW from a $\lambda/4$ monopole located on the top surface of a rectangular case. The case was made of plastics material (with $\epsilon_r=2.0$, as in [7]) with a conducting inner coating. This was placed in an anechoic chamber, and near-field measurements of the x-component of the electric field were made over the volume shown in Figure 4. An FDTD representation of a handset with the same dimensions was constructed and the same field component was calculated. Figure 5 shows the electric field intensity in a series of planes at regular intervals away from the handset. The measured results can be seen to compare very closely with results from FDTD analysis in the region close to the handset. The discrepancy appears to increase somewhat at larger distances (maximum error within 3dB), but the agreement can still be said to be good, given the difficulties of representing the exact structure of a simulated handset assembled from commercial components, and errors inherent in field strength measurements with a small dipole probe. The results can be said to demonstrate the validity of Luebbers' model of an antenna on a plastic coated metal chassis [7] in the near field.

Figure 6 shows the total electric field magnitude, as calculated by the FDTD method, in the arrangement described above. Also shown are the results calculated by rotating the FDTD handset model by 45° about the z-axis. The results for the rotated handset are seen to give excellent agreement with those for the axially-aligned handset.

The far field was also calculated for the axially aligned and rotated handsets using the near-to-far field transformation method described by Taflov & Umashankar [13]. Figure 7 shows the far-field radiation pattern in the x-y plane for both orientations: the results from the rotated handset have been rotated back by 45° to enable direct comparison to be made. The amplitudes are in good agreement, with a slight angular offset. Empirically, the angle of error has been found to be of the order of $1/N$ radians, where N is the number of cells in the FDTD antenna. This indicates that quantization is the cause of the angular error: use of finer FDTD meshes reduces it.

4.2 Output Power

The power radiated by the FDTD handset model was measured for a range of orientation angles. Although

the radiation patterns were in excellent agreement for all orientation angles, it was found that the actual power radiated was dependent upon orientation. Let the angle β now be defined as the angle between the antenna and the x-axis in the x-z plane (see Figure 1). The FDTD handset model was set to a number of values of β between 0 and $\pi/2$ and the radiated power was computed in each case. The power calculation was performed by summing the outgoing component of the Poynting vector over a closed surface surrounding the handset. Figure 8 shows the power transmitted as a function of angle when the monopole was fed with 1A peak CW at 1.8GHz. The FDTD cells were cubes with side lengths of 2.5mm, corresponding to approximately $\lambda/33$ in free space.

The radiated power can be seen to vary by around 20% as the angle is varied. The power output is symmetrical about the $\pi/4$ orientation as would be expected in a cubic FDTD mesh. It was suspected that the variation might be due to quantization errors in the length of the antenna and the handset body. The antenna is required to be terminated by zeroing the current in its end segment. As different orientations imply differing values of Δx_{tw} , Δy_{tw} and Δz_{tw} the 'thin wire' antenna may be expected to be a source of error, since end segments of varying lengths would be partially excluded from the electrical length.

Fig. 9 shows the currents along the antenna for orientations between 0 and 45° . The results are symmetrical about 45° so results from 45° to 90° are not shown. The currents follow a similar pattern, but with discrepancies of up to 10%, which might account for the 20% variation in total power. To study this phenomenon further, the same problem was re-computed using a reduced cell size of 1.25mm ($\lambda/67$). Figures 10 and 11 show the power and current for a range of orientation angles at this resolution. The variation in power (Figure 10) is reduced to 6% maximum, and the variation in current (Figure 11) is nowhere higher than 7% along the lengths of the wires. The relatively large drop in power variation, compared with the result for $\lambda/33$ resolution, suggests that the handset body may be equally responsible for power variations. The finer cell size enables the representation of a rotated body to be electrically more exact. The marked improvement in correlation of both power outputs and currents, as resolution improves, indicates that the small discrepancies originate from quantization errors, not errors in the method. It is important to note that, when field patterns are normalised to 1 Watt output (as is normal in the Specific Absorption Rate (SAR) calculations, for which the rotatable handset model has

been developed), both near and far-field patterns are in excellent agreement at all orientation angles.

5. CONCLUSION

It has been shown that the 'thin wire' technique can be used as a basis for modelling an arbitrarily-oriented handset (or some other structure made of dielectrics and metal) in an FDTD lattice. Both near and far fields are in good agreement with the results for a handset in the 'conventional' orientation, i.e. with principal dimensions parallel to the Cartesian axes, and the near fields also agreed well with physical measurements. This technique has particular application to the calculation of the interaction between realistically-oriented portable handsets and the human body. The technique for rotating a solid object in an FDTD lattice has broad application to problems involving two or more physical entities that may be re-positioned in relation to each other (e.g. helicopter rotors and microwave oven interiors). One or more of the objects can be positioned, and repositioned, relative to others without significant restructuring of the program or input data.

REFERENCES

- [1] P.J. Dimbylow and O.P. Gandhi, 'Finite-Difference Time-Domain Calculations of SAR in a Realistic Heterogeneous Model of a Head for Plane Wave Exposure from 600MHz to 3GHz', *Phys. Med. Biol.*, Vol. 36, No. 8, pp 1075-1089, 1991
- [2] P.J. Dimbylow, 'FDTD Calculations of the SAR for a dipole closely coupled to the head at 900MHz and 1.9GHz', *Phys. Med. Biol.*, Vol. 38, pp 361-368, 1992
- [3] P.J. Dimbylow and S.M. Mann, 'SAR calculations in an anatomically realistic model of the head for mobile communication transceivers at 900MHz and 1.8GHz', *Phys. Med. Biol.*, Vol. 39, pp 1537-1553, 1994
- [4] J. Toftgard, S.N. Hornsleth and J.B. Andersen, 'Effects on Portable Antennas by the Presence of a Person', *IEEE Trans. Antennas & Propagation*, Vol.41, No. 6, pp 739-746, 1993
- [5] H.N. Kritikos and H.P. Schwan, 'Hot Spots Generated in Conducting Spheres by Electromagnetic Waves and Biological Implications', *IEEE Trans. Biomed. Eng.*, Vol. BME-19, No. 1, pp 53-58, 1972
- [6] A.R. Shapiro, R.F. Lutomirski and H.T. Yura, 'Induced Fields and Heating Within a Cranial Structure Irradiated by an Electromagnetic Plane Wave', *IEEE Trans. Microwave Theory & Tech.*, Vol. MTT-19, No. 2, pp 187-196, 1971
- [7] R. Luebbers, L. Chen, T. Uno and S. Adachi, 'FDTD Calculation of Radiation Patterns, Impedance and Gain for a Monopole Antenna on a Conducting Box', *IEEE Trans. Antennas & Propagation*, Vol. 40, No. 12, pp 1577-1583, 1992
- [8] M.A. Jensen and Y. Rahmat-Samii, 'EM Interaction of Handset Antennas and a Human in Personal Communications', *Proc. IEEE*, Vol. 83, No. 1, pp 7-17, 1995
- [9] R. Holland and L. Simpson, 'Finite Difference Analysis of EMP Coupling to Thin Struts and Wires', *IEEE Trans. Electromag. Compat.*, Vol. EMC-23, No. 2, pp 88-97, 1981
- [10] K.S. Yee, 'Numerical Solution of Initial Boundary Value Problems involving Maxwell's Equations in Isotropic Media', *IEEE Trans. Antennas & Propagation*, Vol. AP-14, pp 302-307, 1966
- [11] R. Holland, 'THREDE: A Free-Field EMP Coupling and Scattering Code', *IEEE Trans. Nucl. Sci.*, Vol. NS-24, No. 6, pp 2416-2421, 1977
- [12] K. K. Mei and J. Fang, 'Superabsorption - A Method to Improve Absorbing Boundary Conditions', *IEEE Trans. Antennas & Propagation*, Vol. 40, pp 1001-1010, 1992
- [13] A. Taflove and K. Umashankar, 'Radar Cross Section of General Three-Dimensional Scatterers', *IEEE Trans. Electromag. Compat.*, Vol. EMC-25, No.4, pp 433-440, 1983

Acknowledgement

This work was supported by the UK SERC/DTI 'LINK' Personal Communications Programme and a consortium of nine companies. Purchase of THREDE source code from EMA Inc. was funded by a grant from the University of Bradford Research Committee.

APPENDIX 1

Quantitative Accuracy Statements

1. An estimate of the accuracy of the results presented here can be made from examination of the comparisons

presented in Figs 5, 6, 7, 9 and 11, and from a comparison of Figs 8 and 10.

In Fig. 5, it is seen that the shapes of the computed near-field distributions agree well with the measured results (normalised to equality at identical central points) and the maximum magnitude discrepancy is within 3dB. Experience suggests that this discrepancy is partly caused by the limitations of the quantised FDTD representation of the handset structure and partly by measurement uncertainty. Fig. 6 indicates that computed near field results are stable to within 1dB under rotational transformation with respect to the FDTD mesh.

Fig. 7 indicates stability in the peak far field gain of better than 0.5dB under rotational transformation. Errors of the order of 10dB may occur in deep nulls, but this is a common problem which could be reduced by using a smaller cell size.

Comparison of Figs 8 and 10 shows that the cell size of $\lambda/33$ used to produce the above results also leads to variations of about $\pm 0.5\text{dB}$ in the radiated power under rotational transformation, but that halving the cell size reduces this to $\pm 0.12\text{dB}$.

Fig. 9 indicates maximum variations of about $\pm 0.2\text{dB}$ in the antenna current distribution under rotational transformation with a cell size of $\lambda/33$, reducing to $\pm 0.13\text{dB}$ with $\lambda/67$ cells (Fig.11).

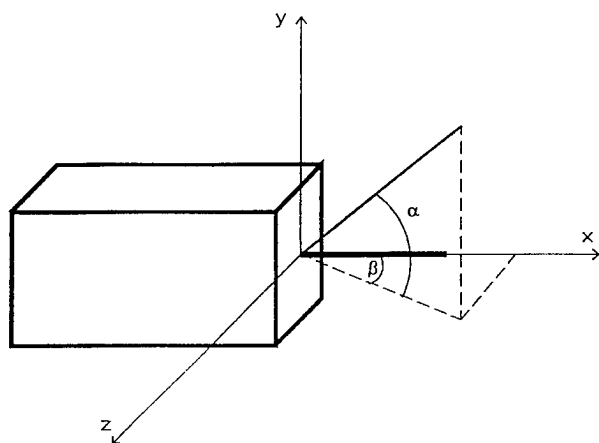


Fig.1 The simulated generic handset, associated co-ordinate system and rotation angles.

2. These estimates are based on measurement (Fig. 5), co-ordinate transformation and variation of discretisation intervals.

3. The kinds of problems for which the above error/accuracy statements can be made for this program include the modelling of current distributions, near and far fields for arbitrary structures of conductor and dielectric, with maximum dimensions up to about a wavelength.

4. Nominal sampling densities required to achieve these estimated accuracies are $\lambda/33$ in most cases ($\lambda/67$ where indicated).

5. The operation count needed to exercise the model reported here is estimated nominally to be of the order of $10^{12}f^1$, where f is in Hz.

6. The variable storage needed to exercise this model is estimated nominally to be 1Mword for $\lambda/33$ sampling density (8Mwords for $\lambda/67$). This is based on the modelling of a simulated handset at 1.8GHz, where $\lambda/33 = 5\text{mm}$. The model, with the same absolute dimensions and sampling interval, could be used down to about 1GHz, below which the free-space margin between conductors and the absorbing boundary would have to be increased; it should also remain stable up to about 4GHz (based on sampling interval considerations), although substantial errors would begin to appear in some parameters.

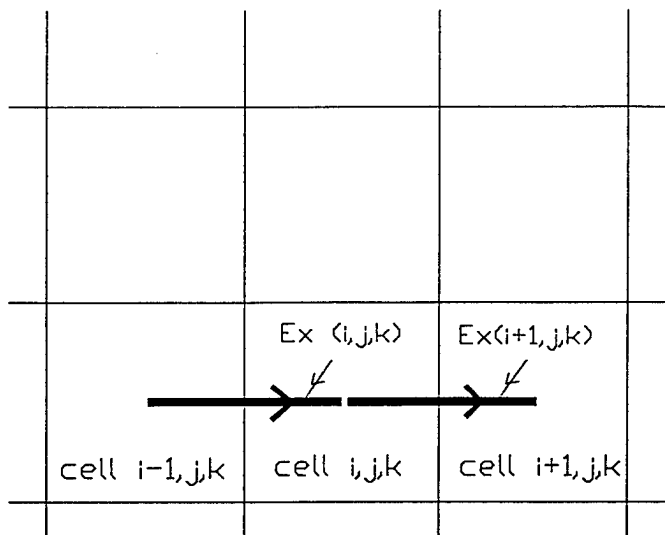


Fig.2 Rectilinear linkage of electric field components between adjacent FDTD cells: a continuous sequence of such links is needed to represent a thin wire.

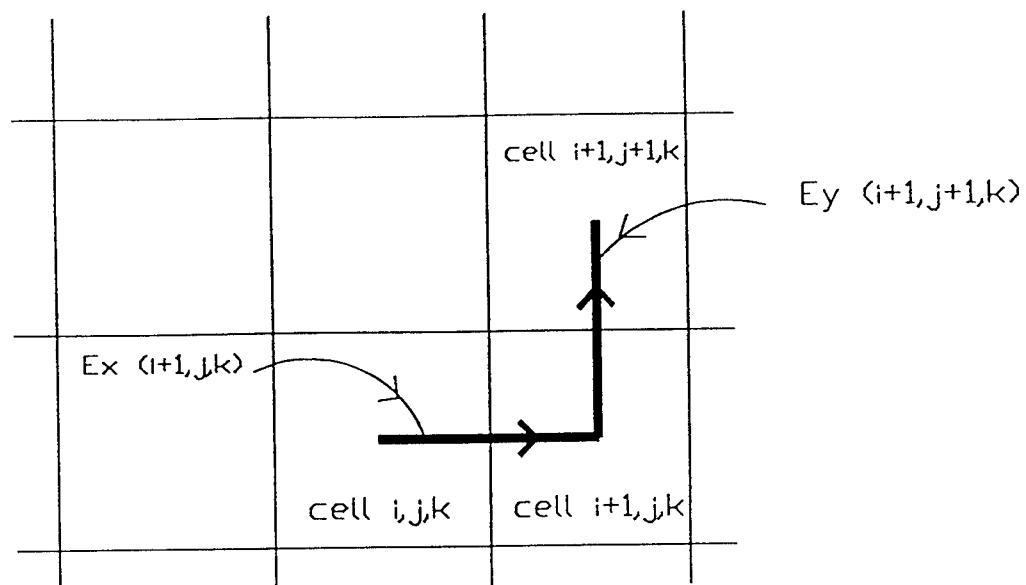


Fig.3 Angled linkage of electric field components between non-rectilinear sequences of FDTD cells.

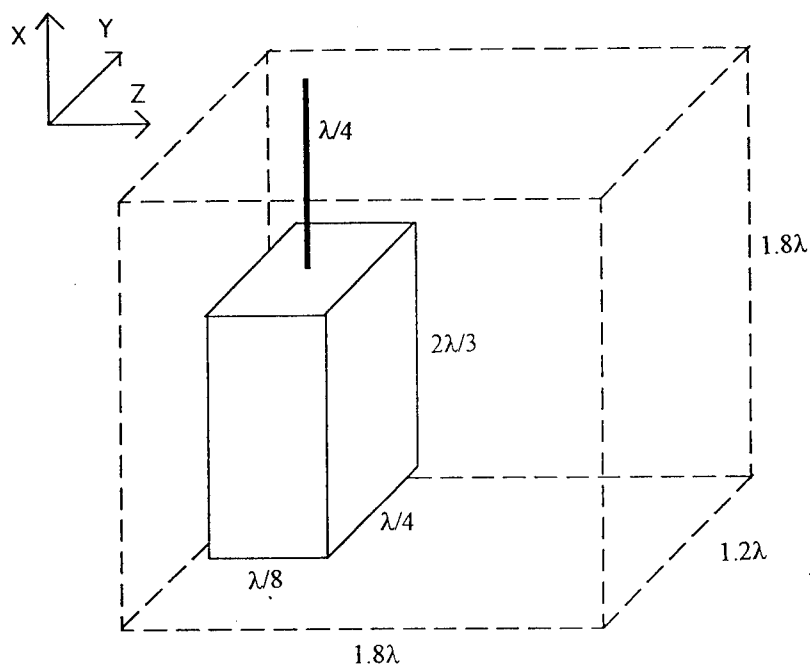


Fig.4 Dimensions of handset and volume over which fields were computed and measured. Dimensions are given in free-space wavelengths at 1.8GHz.

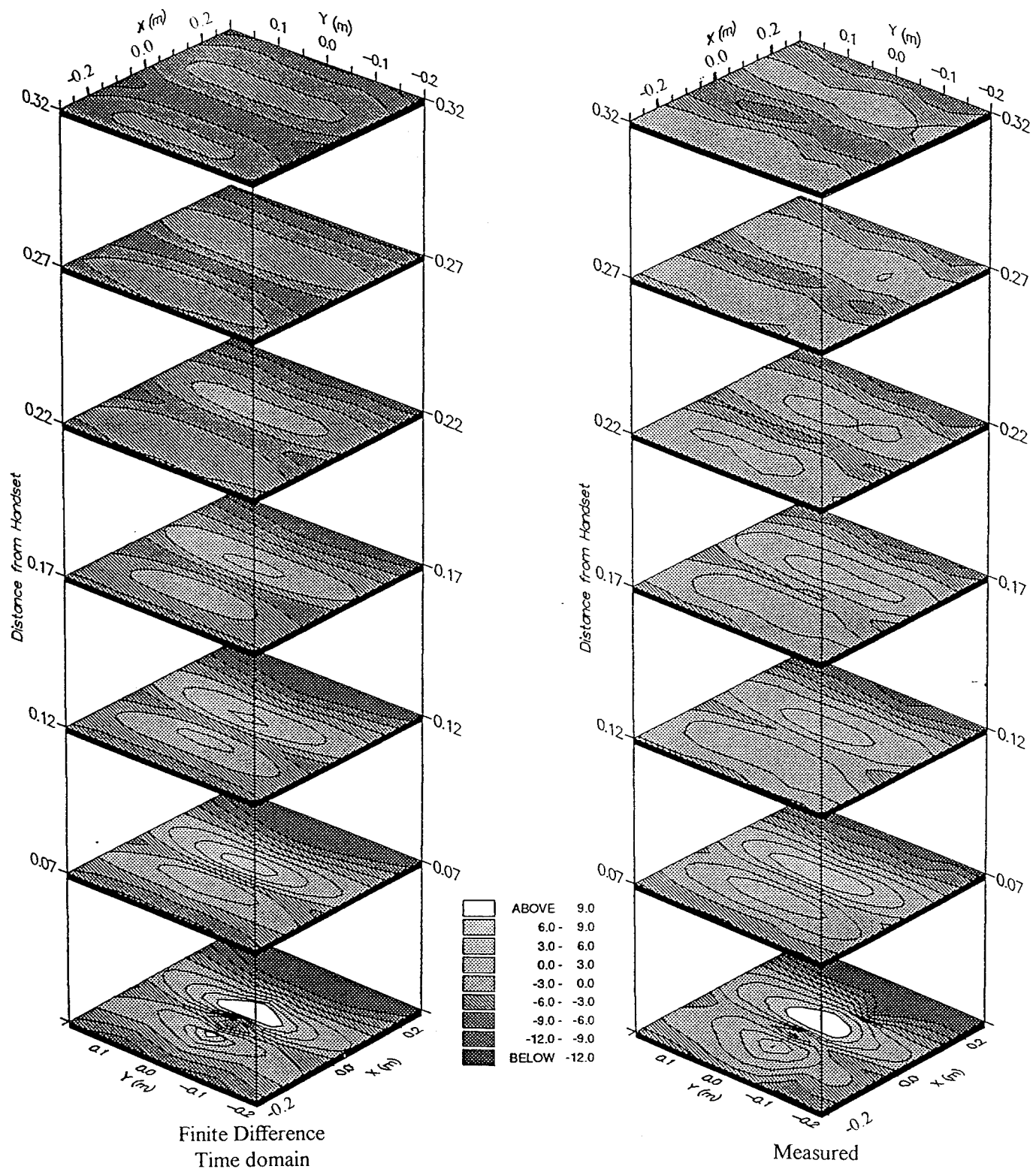


Fig.5 Magnitude in dB of the x-component of the electric field over several planes normal to the z-axis: (a) as computed by FDTD; (b) as measured. Both plots are normalised to their respective amplitudes at the centre of the plane 0.17m from the handset.

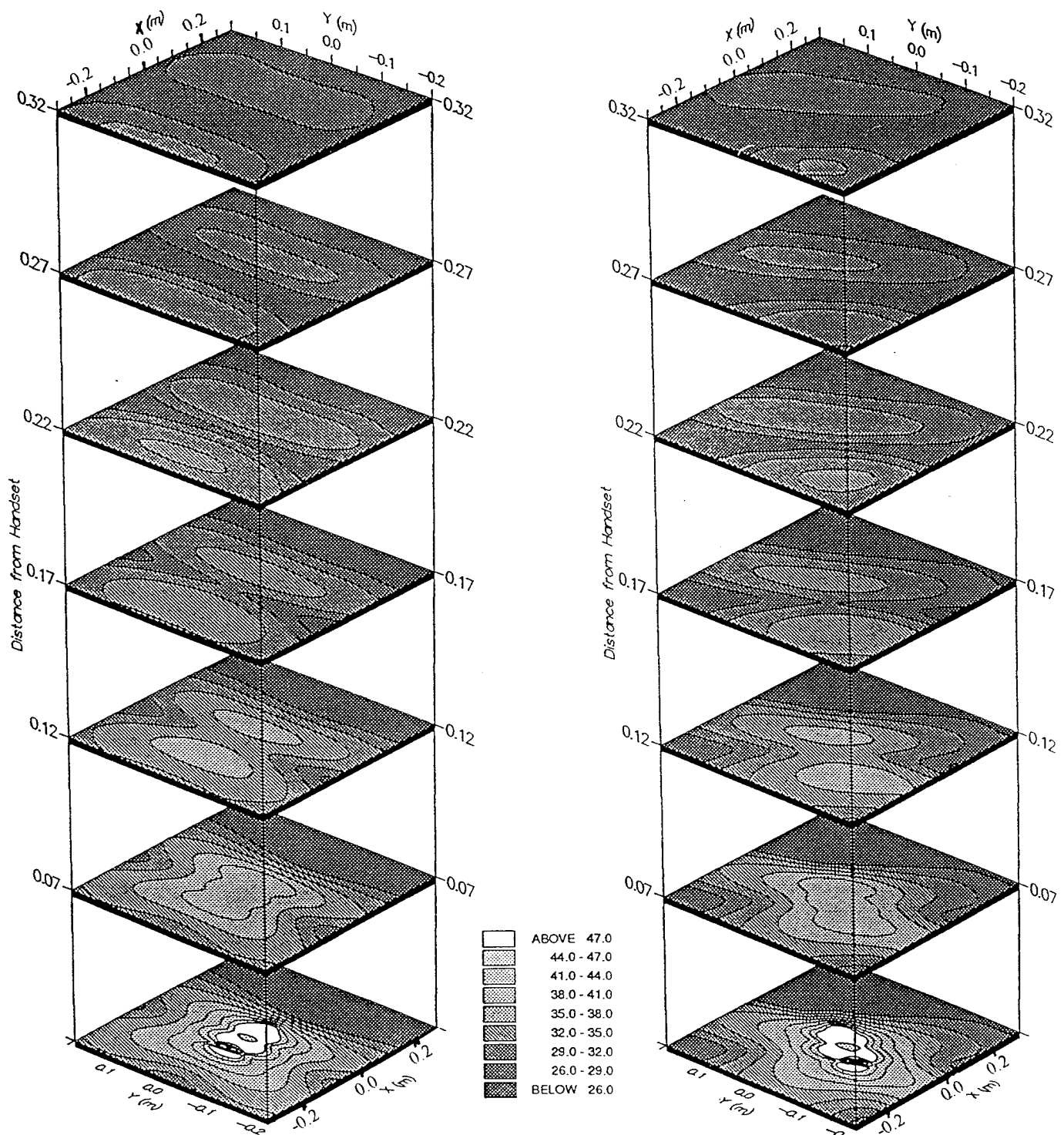


Fig.6 Magnitude (in un-normalised dB) of the total electric field ($|E|$) over several planes normal to the z-axis as computed by FDTD: (a) handset axially-aligned; (b) handset rotated 45° about z-axis.

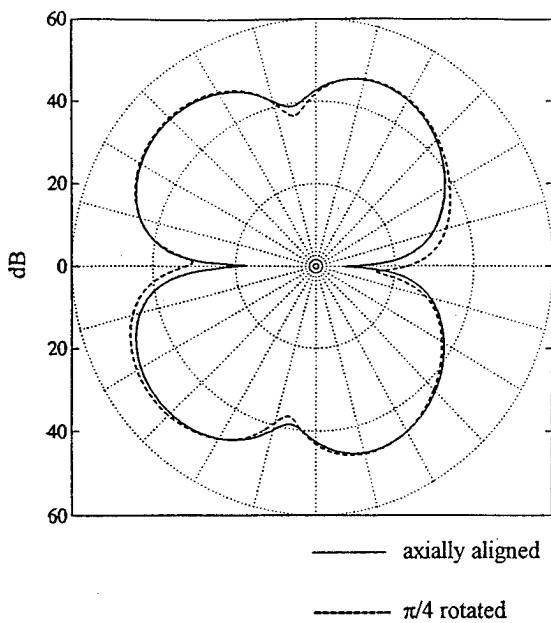


Fig.7 Far-field pattern in plane $z=0$, as computed by FDTD with handset axially oriented (solid curve) and rotated 45° about z -axis (the broken curve shows the result as rotated back by -45° to facilitate comparison). Scale is in dB relative to the same reference level, with a constant offset added to make all results positive.

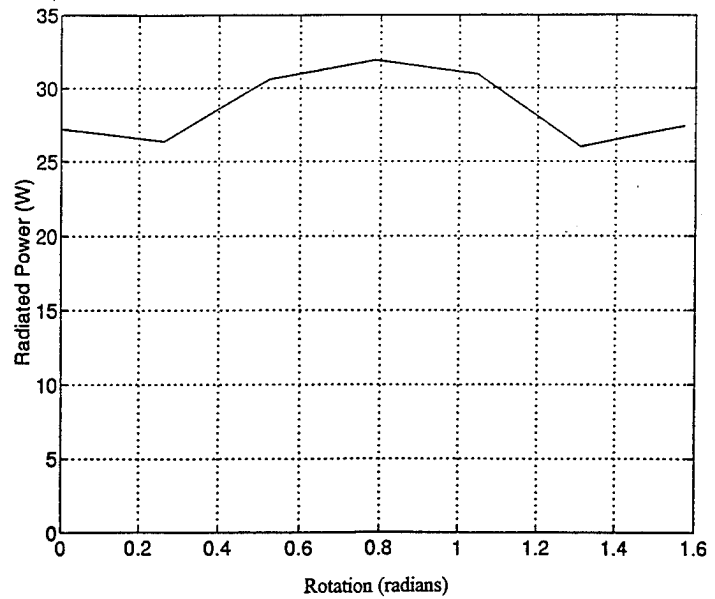


Fig.8 Total radiated power predicted by FDTD (mesh interval $= \lambda/33$), for constant antenna feedpoint current, as a function of handset rotation angle.

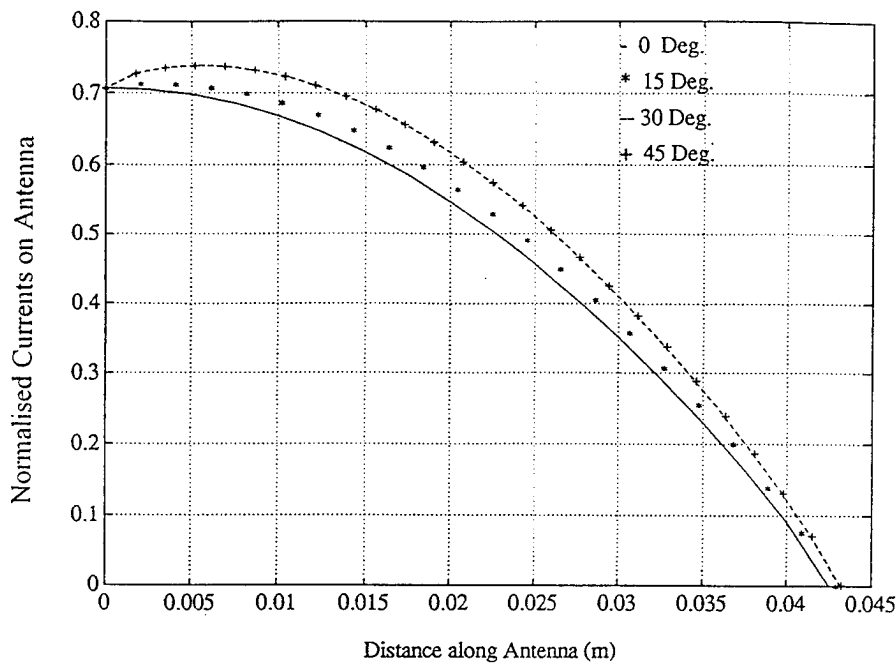


Fig.9 Variation of computed current distribution in the monopole with rotation of the handset, for FDTD mesh interval of $\lambda/33$. Normalised current is displayed as the ratio of local r.m.s. value to peak driving current at base of antenna.

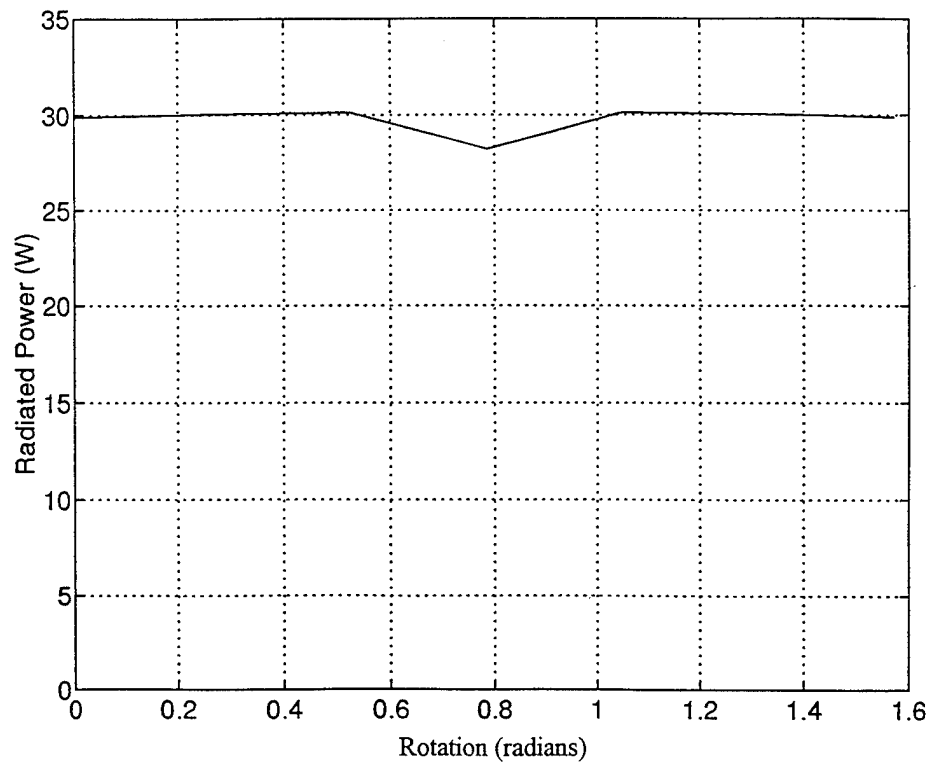


Fig.10 Total radiated power as a function of orientation angle, for FDTD mesh interval of $\lambda/67$.

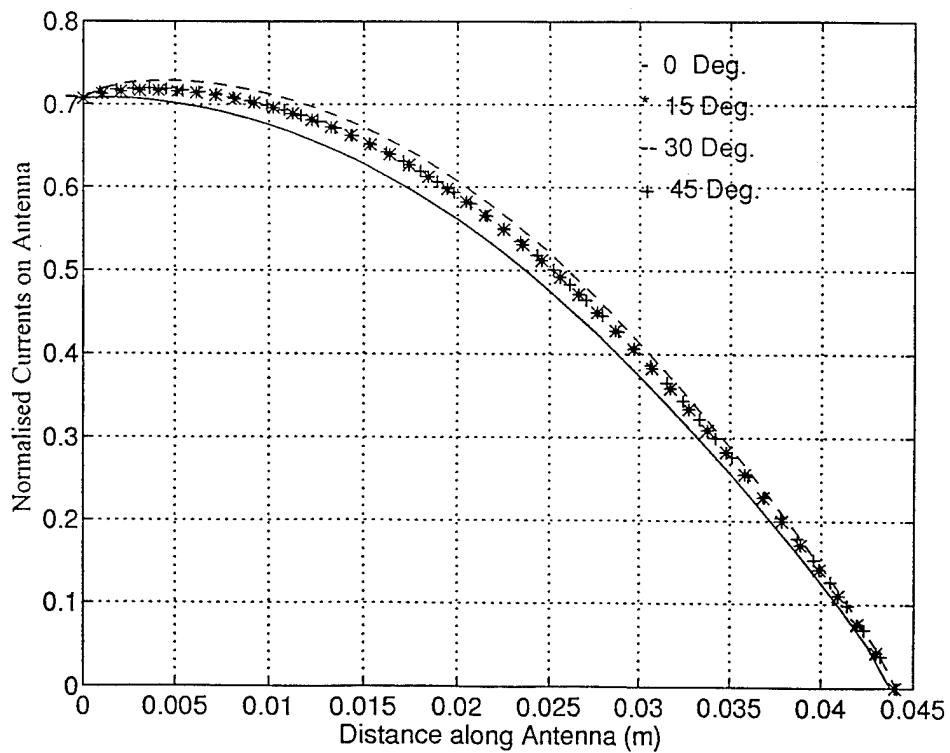


Fig.11 Variation of computed current distribution in the monopole with rotation of the handset, for FDTD mesh interval of $\lambda/67$ (Current normalised as in Fig. 9).

A MAGNETIC FIELD ITERATIVE TECHNIQUE FOR IMPROVING HIGH FREQUENCY PREDICTION METHODS

Daniel D. Reuster and Gary A. Thiele
Department of Electrical Engineering
University of Dayton
Dayton, OH 45469-0226

Paul W. Eloë
Department of Mathematics
University of Dayton
Dayton, OH 45469-2316

Abstract

A Magnetic Field Iterative Technique (MFIT) is developed as a technique for improving the results from high frequency based prediction methods. The technique combines the accuracy of low frequency methods with the speed of high frequency methods to develop a contraction mapping based, iterative solver, which is directly parallelizable on current massively parallel processing machines. In this paper, the MFIT is developed from a Magnetic Field Integral Equation (MFIE) and its contraction mapping properties are discussed. Results obtained using the technique and illustrations of the technique's convergence properties are presented for both two and three dimensional perfect electrically conducting (PEC) targets.

Introduction

High frequency based numerical prediction methods such as Physical Optics - Physical Theory of Diffraction (PO-PTD) [1] and Geometrical Optics - Geometrical Theory of Diffraction (GO-GTD) [2] have been shown to be successful at approximating the induced current distributions on electrically large targets (e.g., three dimensional bodies with at least one dimension greater than approximately ten wavelengths). For these electrically large bodies, the high frequency series expansion associated with their scattering properties converges quickly and scattering centers located about the bodies can be easily identified. However, as the electrical size of these perfect electrically conducting (PEC) bodies begin to decrease, the ability to clearly define the required scattering centers becomes difficult and the convergence rate of the associated series expansions decreases rapidly. Most often, more exact numerical methods such as the Method of Moments (MoM) [3,4] and the Finite Element Method (FEM) [5] have been utilized for these particular situations. While these methods (MoM and FEM) have been proven to be both accurate and reliable for

PEC bodies which are less than approximately three wavelengths on a side, these methods become difficult to implement for much larger bodies. Large memory requirements coupled with long execution times, make the utilization of these methods difficult for large bodies.

The Magnetic Field Iterative Technique (MFIT) is developed here for those PEC bodies whose electrical size falls into the awkward gap which exists between the two groups of numerical methods. Currently, there are few options that exist for efficiently calculating the induced current distributions on these particular PEC bodies. The following method is a hybrid numerical technique which takes advantage of the desired features from both the high frequency and nearly exact solution methods. The method is an extension of previous research performed by Thiele et al. [6-8] on hybrid and iterative methods for solving electrically large problems.

Mathematical Development

For closed volumetric PEC bodies, a Magnetic Field Integral Equation (MFIE) may be stated in terms of the total magnetic field as [3]:

$$\bar{H}^T(\bar{r}) = \frac{1}{4\pi} \int_S (\hat{n} \times \bar{H}^T(\bar{r}')) \times \nabla' G(\bar{r}, \bar{r}') ds + \bar{H}^I(\bar{r}) \quad (1)$$

$$\text{where } \lim_{\bar{r} \rightarrow \bar{r}'} \frac{1}{4\pi} \int_S (\hat{n} \times \bar{H}^T(\bar{r}')) \times \nabla' G(\bar{r}, \bar{r}') ds \\ = \frac{1}{2} (\bar{H}^T(\bar{r}) - \hat{n}(\hat{n} \cdot \bar{H}^T(\bar{r}))) \quad (2)$$

S is the closed volumetric PEC surface, G is the standard free space Green's function, T is the total field, and I is the incident field. Equations 1 and 2 are in the form of a contraction mapping [9,10], and it may be shown that direct

incident field. Equations 1 and 2 are in the form of a contraction mapping [9,10], and it may be shown that direct iteration of these equations will yield monotonic mean-square convergence provided that the integral operator is bounded by unity. If the integral operator does satisfy this bound, then the above convergence is guaranteed independent of the initial guess. While this unity bound may be shown for explicit geometries, a general proof does not yet exist. Extensive discussion regarding the guarantee of convergence may be found in references [11-14].

Since equations 1 and 2 are normally implemented in discretized form, it is best to discuss the issue of convergence in terms of the discretized equations. Applying a pulse-basis point-matching expansion to the above MFIE results in the following discretized equation where delta is the area of the discretized facets (see Figure 1):

$$\bar{H}_m^T = \sum_{n \neq m} \Delta_n G(\bar{R}_{mn}) \left[\frac{1}{|\bar{R}_{mn}|} + jk \right] \bar{J}_n + \frac{1}{2} \bar{J}_m + \bar{H}_m^I \quad (3)$$

$$\text{where } \bar{J}_n = \frac{\bar{H}_n^T (\bar{R}_{mn} \cdot \hat{n}) - \hat{n} (\bar{R}_{mn} \cdot \bar{H}_n^T)}{|\bar{R}_{mn}|} \quad (4)$$

$$\text{and } \bar{J}_m = \bar{H}_m^T - \hat{n} (\bar{H}_m^T \cdot \hat{n}) \quad (5)$$

Expressing the discretized MFIE in matrix form transforms the problem of establishing convergence from bounding the integral operator to determining the spectral radius of the reaction matrix $[Z_{mn}]$ (Equation 6). If the spectral radius of the reaction matrix is less than unity, then the discretized MFIE is a true contraction mapping and direct iteration of the discretized equation will guarantee monotonic mean square convergence.

$$\begin{bmatrix} H_m^T \end{bmatrix} = \begin{bmatrix} Z_{mn} \end{bmatrix} \begin{bmatrix} H_n^T \end{bmatrix} + \begin{bmatrix} H_m^I \end{bmatrix} \quad (6)$$

For cases where the spectral radius is not less than unity, it is possible to shift the spectral radius of the matrix $[Z_{mn}]$ by using a relaxation parameter [11-14]. The implementation of the relaxation parameter α is given in Equation 7 and its numerical value is a function of the largest eigenvalue of the $[Z_{mn}]$ matrix. Thus, for all given reaction matrices, it is possible to obtain the desired solution through direct iteration with the guarantee of monotonic mean-square convergence if α is properly chosen as required by the

following equation where L is the linear operator used in Equation 6:

$$H^{k+1} = \omega L(H^k) + (1-\omega)H^k \quad \omega < 1 \quad (7)$$

While the guarantee of convergence is independent of the initial guess, the rate of convergence is not; and thus, for the MFIE to serve as an efficient method to obtain the induced current distributions on volumetric PEC bodies, the iterative procedure must be initiated with the best guess available such that the computation time associated with the calculation of the initial guess is small compared to the computation time associated with the iterative procedure. For this reason, high frequency techniques such as GO-GTD and PO-PTD are used to generate the initial guess. Both of these techniques have negligible computer run times and are capable of producing approximations for the induced current distributions which are in the realm of rapid convergence. It is the use of the high frequency prediction methods' results, as an initial guess to the iterative process, which creates the hybrid method. By initiating the iterative process with these results, the large amount of computational work associated with calculating the principle current distributions using the more exact methods is removed from the solution process, leaving the iterative process to fine tune the results rather than regenerating the first order solutions which constantly reoccur. In essence, a high frequency prediction method is used to quickly obtain the general portion of the solution and the iterative solution method is used to fine tune the general solution to the particular PEC body.

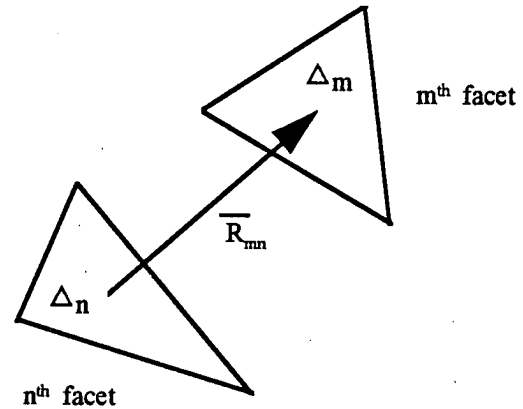


Figure 1 Discretized Geometry

2-Dimensional Example

For the 2-dimensional transverse electric (TE) case, the previous vector MFIE (Equations 1 and 2) simplifies to the following scalar integral equation [6].

$$H_x^T(\bar{r}) = -\frac{jk}{4} \int_C H_z^T(\bar{r}') G(\bar{r}, \bar{r}') \cos(\theta) d\ell + H_z^I(\bar{r}) \quad (8)$$

Applying a pulse-basis point-matching expansion to the above integral operation results in the following series expansion [3].

$$H_m^T = -\frac{jk}{4} \sum_{m \neq n} \Delta_n H_n^T G(|\bar{R}_{mn}|) \cos(\theta_{mn}) + \frac{1}{2} H_m^T + H_m^I \quad (9)$$

This 2-dimensional series expansion was applied to a 1 wavelength diameter PEC cylinder (see Figure 2). The 2-dimensional contour was discretized at twenty points per wavelength, and the iterative procedure was initiated with its high frequency Physical Optics approximation [1]. Figure 4 shows the converging currents for the circular cylinder starting with the initial guess, then the current after 1, 5, and 10 iterations ending with the “converged” current. For this example, convergence was based upon a tight mean-square error norm of 0.001. The converged solution was obtained after 19 iterations and the vast improvement after only 5 iterations should be noted. As can be seen, the monotonic mean square convergence associated with contraction mappings is present in the converging iterative solution.

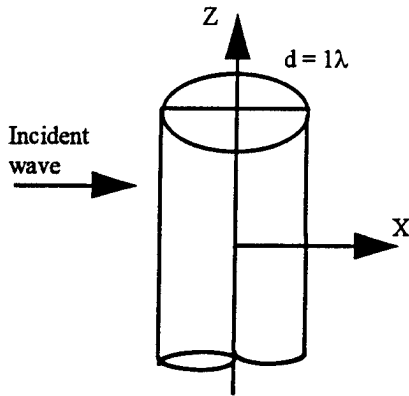


Figure 2 One Wavelength PEC Cylinder Geometry

3-Dimensional Example

A 1 wavelength PEC cube, with a normally incident transverse electric (TE) plane wave is shown as a 3-

dimensional example (see Figure 3). The cube geometry was selected because of the non-uniform and singular current distributions that exist about its sharp edged structure. These particular current distributions have been traditionally difficult to calculate and would serve as a rigorous test on the contraction mapping properties of the MFIE formulation. The cube surface was facetized with approximately 1,300 triangular facets and Xpatch [15], a high frequency ray based prediction code, was used to provide the initial current distribution (see Figure 5a). As can be seen from Figure 5a, while the high frequency prediction does a good job of predicting the current distribution on the front face of the cube, it fails to predict any current distributions on the remaining five faces of the cube.

Performing a single iteration on the high frequency predicted current distribution (Figure 5b) results in a non-zero current distribution on all faces of the cube surface. Further iterations (Figures 5c and 5d) again illustrate the contraction like mapping properties of the MFIE formulation and the convergence of the induced current distributions along the surfaces of the PEC cube. Comparing the high frequency predicted current distribution (Figure 5a) with the converged current distribution obtained after 20 iterations (Figure 5d) shows a substantial difference in all but the front face of the cube. Finally, it should be noted that all of the non-uniform and singular current distributions are present and observable in the converged current distribution, and that these difficult current distributions had no detrimental effect on the convergence of the iterative procedure.

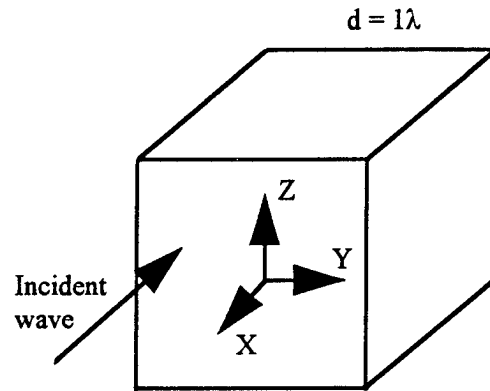


Figure 3 One Wavelength PEC Cube Geometry

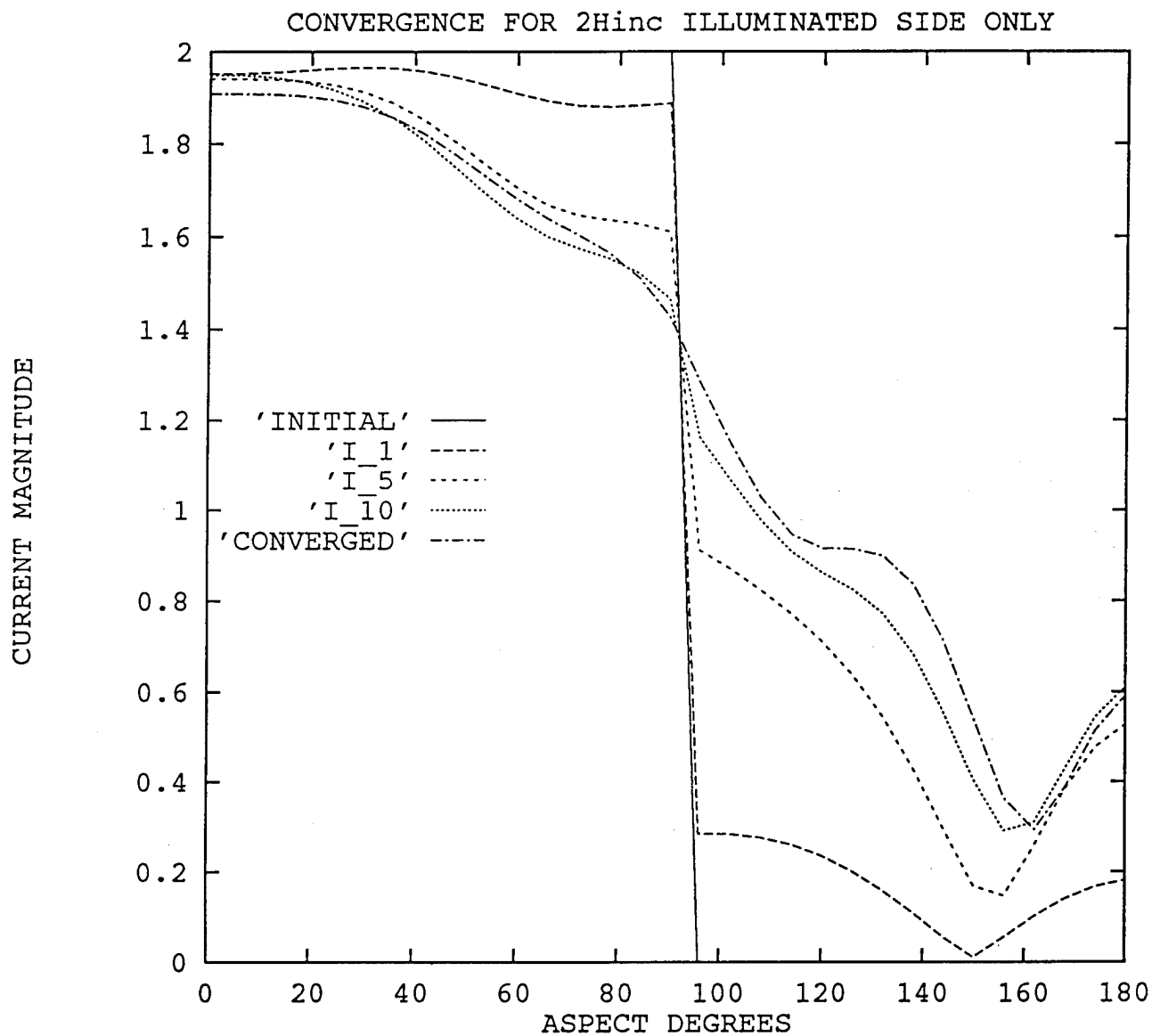
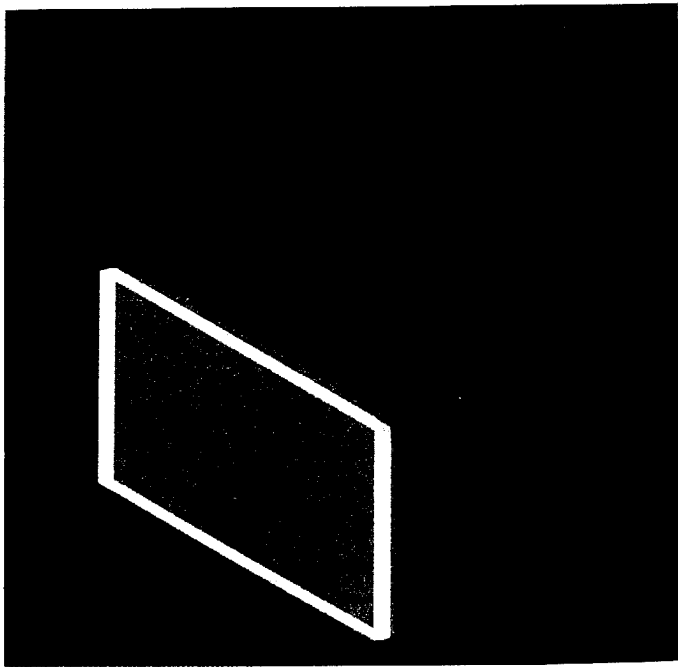
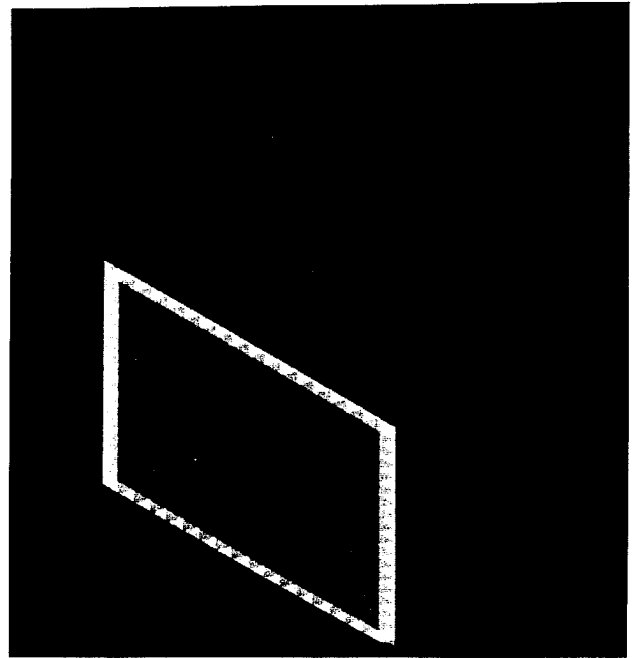


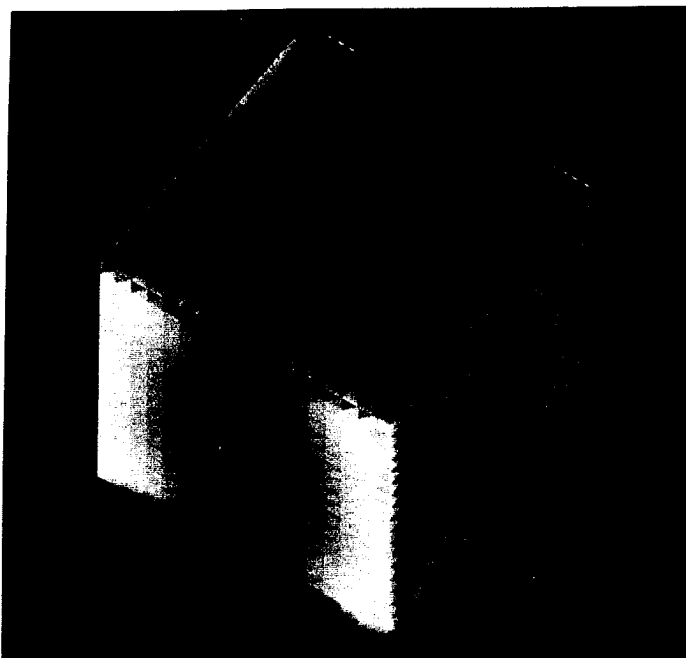
Figure 4 The current magnitudes after 1, 5, 10, and 19 iterations starting with the Physical Optics current distribution on a circular cylinder of 1 wavelength in diameter.



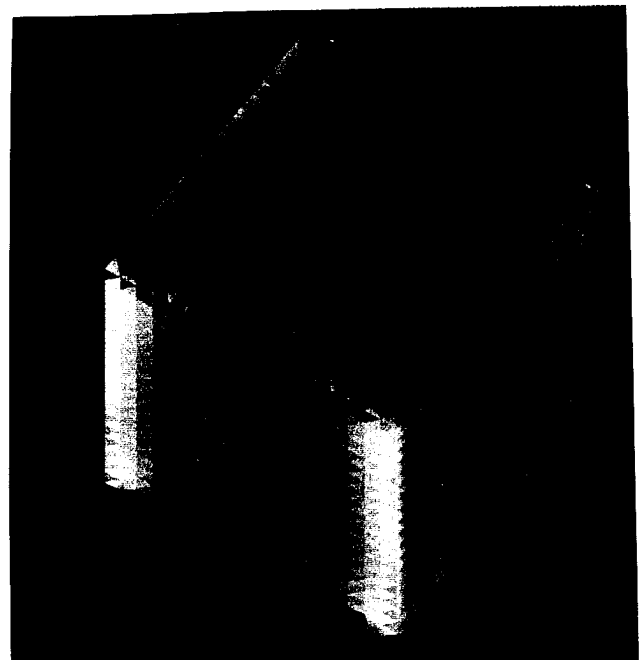
(a) Xpatch Only



(b) 1 Iteration



(c) 10 Iterations



(c) 20 Iterations

Figures 5a-d Current Magnitudes on a 1 Wavelength Cube

Conclusions and Comments

Based upon the results presented, the MFIT shows promise as an efficient method for bridging the gap between traditional high frequency and low frequency numerical techniques. Although this hybrid method is designed for bodies which are 3 to 10 wavelengths in size, the 1 wavelength bodies selected in the examples were chosen because of their ability to compactly illustrate the fundamental principles underlying the MFIT. The use of high frequency methods to provide an initial guess to an iterative solution formulation of low frequency methods allows the combination of the best of both techniques. The information readily obtained using high frequency methods greatly reduces the run time associated with the low frequency methods. Hence, the low frequency portion of this hybrid method is used solely to obtain the desired solution accuracy and valuable computer time is not wasted on obtaining portions of the solution which are well known or more readily obtainable. Furthermore, iterative solvers for systems of linear equations are highly parallelizable on current massively parallel processing machines, thus further reducing the run times associated with the low frequency portion of the hybrid technique.

The contraction mapping principle, associated with the formulation of the MFIT presented, removes many of the dangers commonly encountered when working with iterative solvers [9-10]. The use of the relaxation parameter α allows generic reaction matrices to be quickly reformulated into contraction mapping based systems. For more information on the use of relaxation parameters to ensure contraction mapping properties, the authors recommend references [11-14] and the references therein.

In summary, a procedure has been presented which uses a magnetic field integral equation in an iterative process. The MFIE is discretized and a relaxation parameter is used to ensure the spectral radius of the reaction matrix is less than unity. The discretized MFIE has contraction mapping properties such as guaranteed monotonic mean square convergence. The iterative process starts with a first order approximation to the current by using a high frequency technique such as physical optics or geometrical optics (shooting and bouncing rays) rather than starting at zero current. The use of a high frequency technique as a starting point in the iterative process significantly speeds up the iterative convergence but is not necessary to obtain a converged result since that is guaranteed by the contraction mapping. A future paper will deal with two MFIE formulations in the MFIT and explore their convergence properties in more detail.

References

1. Lo, Y. T. and Lee, S. W., Antenna Handbook, New York: Van Nostrand Reinhold Company, 1988.
2. James, G. L., The Geometrical Theory of Diffraction for Electromagnetic Waves, Institute of Electrical Engineers, London, 1986.
3. Harrington, R. F., Field Computation by Moment Methods, Macmillan, New York, 1968.
4. Wang, J. H., Generalized Moment Methods in Electromagnetics, Wiley, New York, 1991.
5. Silvester, P. P., and Ferrari, R. L., Finite Elements for Electrical Engineers, Cambridge, University Press, Cambridge, 1983.
6. Kaye, M., Murthy, P. K., and Thiele, G. A., "An Iterative Method for Solving Scattering Problems," IEEE Trans. Ant. Prop., Vol. AP-33, No. 11, pp. 1272-79, Nov. 1985.
7. Murthy, P. K., Hill, K. C., and Thiele, G. A., "A Hybrid-Iterative Method for Scattering Problems," IEEE Trans. Ant. Prop., Vol. AP-34, No. 10, pp. 1173-80, Oct. 1986.
8. Penno, R. P., Thiele, G. A., and Murthy, P. K., "Scattering from a Perfectly Conducting Cube Using HIM," Special Issue of IEEE Proceedings on Radar Cross-Section, Vol. 77, No. 5, pp. 815-23, May 1989.
9. Conte, S. D., and Boor, C., Elementary Numerical Analysis, An Algorithmic Approach, McGraw-Hill, New York, 1980.
10. Varga, R. S., Matrix Iterative Analysis, Prentice-Hall, Inc., New Jersey, 1962.
11. Reuster, D. D., Thiele, G. A. and Eloë, P. W., "On the Convergence of the Electric Field Integral Equation," Appl. Math. Lett., Vol 8, No. 6, pp. 43-49, Aug. 1995.
12. Kleinman, R. E., "Some Applications of Functional Analysis in Classical Scattering", Mathematical Methods and Applications of Scattering Theory, DeSanto, J. A., Saenz, A. W., and Zachary, W. W. ed., Lecture Notes in Physics 130, Springer-Verlag Berlin Heidelberg, NY, 1980.
13. Reuster, D. D., Thiele, G. A., and Eloë, P. W., "General Conditions for the Convergence of Iterative Solutions to Magnetic Field Integral Equations," Proceedings - 1995 URSI Inter. Sym. on Electromagnetic Theory, St. Petersburg, Russia, May 23-26, 1995.
14. Reuster, D. D., Thiele, G. A., "A Field Iterative Method for Computing the Scattered Electric Fields at the Apertures of Large Perfectly Conducting Cavities," IEEE Trans. Ant. Prop., Vol. AP-43, No. 3, pp. 286-90, Mar. 1995.
15. Ling, H., Chou, R. and Lee, S. W., "Shooting and Bouncing Rays: Calculating the RCS of an Arbitrary Cavity," IEEE Trans. Ant. Prop., Vol. AP-37, No. 2, pp. 194-205, Feb. 1989.

Modeling of Remote Field Eddy Current transient phenomena

M. Raugi

Dipartimento di Sistemi Elettrici ed Automazione, Università di Pisa,
Via Diotisalvi 2, 56100 Pisa.

N. Ida

Department of Electrical Engineering, The University of Akron
Akron, OH 44325, USA

Abstract - An integral formulation is presented and used for the analysis of the Remote Field Eddy Current (RFEC) transient phenomena. The model presented allows simple and accurate modeling of RFEC systems in the presence of axisymmetric defects.

The method has been validated first by comparison of the computed results with results obtained with an analytical model. Then the method was used to show that the Remote Field effect is mainly due to a direct induction effect rather than propagation effects.

The Remote Field effect phenomena are usually analysed using a steady state domain. However, the results obtained here have shown that detection of defects is not due to a steady state phenomenon, but depends mainly on the transient signal.

1. INTRODUCTION

The remote field effect is a Non Destructive Test method used for the testing of thick ferromagnetic materials for deep defects and in particular corrosion effects on the outer surface of tubes. This is particularly useful for gas lines but also for water lines and other thick walled tubes like oil well casings. The method relies on the use of very low intensity, low frequency electromagnetic fields which, unlike other types of tests are equally sensitive to defects on the outer surface of the tubes as on the inner surface. Thus, testing of thick materials can be easily performed from the accessible inner surface [1]. The RFEC testing probe is made of two coils separated at a distance of about two coil diameters and moving as a unit.

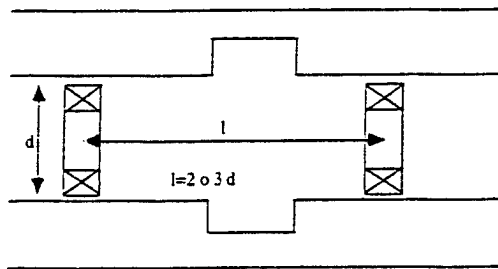


Fig. 1 RFEC probe configuration

One coil (the exciting coil) is driven with a sinusoidal current, and induces an output signal in the second coil (the pick-up coil). The probes move inside the tube at a constant velocity and the exciting current frequency is normally below 100 Hz. The theoretical basis of the remote field effect is not well established. In particular, some models [2-4] call for propagation effects to explain the equal sensitivity to

defects on either surface of the tubes. This model is not supported by experimental data or by the basic electromagnetic theory for low frequency fields. Existing models for the far field effect assume that all testing is done at such low speeds that the motion of the probe does not affect the signal obtained. This is far from being realistic. At low frequencies the speed effects on the signal are large and, in some cases, may even dominate. In this paper, we propose an integral model that incorporates speed effects, to correctly analyse the influence of speed on the calculated data.

2. MODEL

Due to the axial symmetry of the system, we divide the tube into elementary rings in which a uniform current is assumed.

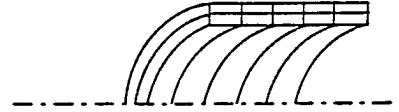


Fig 2 Subdivision of the tube into concentric rings

We write the Ohm's law at a point inside a generic ring as:

$$\frac{J}{\sigma} = -\nabla V - \frac{\partial A}{\partial t} \quad (1)$$

and then integrate both sides of this equation over the volume of the ring to obtain the integral equation [5]:

$$M_{je} \frac{\partial I_e}{\partial t} + \nu I_e \frac{\partial M_{pe}}{\partial x} + R_j I_j + \sum_{k=1}^{n-1} M_{jk} \frac{\partial I_k}{\partial t} + L_j \frac{\partial I_j}{\partial t} = 0 \quad (2)$$

This can be viewed as the electric equilibrium equation of the equivalent circuitual loop made of a resistance R , a self inductance L due to the ring itself and the mutual inductances M between the ring and all other rings that make up the tube and the coils. In Eq. (2) the subscripts k identifies the rings 1 through n , e identifies the exciting coil, I_k the current in the k -th loop of the network and I_e the current in the exciting coil.

To calculate the signal we consider only the n significant rings close to the coils. Writing this equation inside every ring, we obtain a system of n equations, that can be viewed as the equilibrium equations of the equivalent network shown in fig. 3. The equations thus obtained can be easily integrated using a classical Runge-Kutta method.

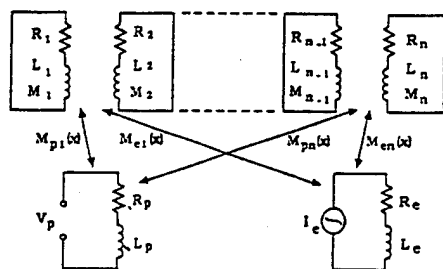


Fig. 3 Equivalent electric network

Axisymmetric defects in the tube are modeled by simply removing the rings corresponding to the volume of the defects. The corresponding loops in the equivalent network are also removed. The output signal V_p is:

$$V_p = \sum_{k=1}^n M_{pk} \frac{\partial I_k}{\partial t} + v I_k \frac{\partial M_{pk}}{\partial x} + M_{pe} \frac{\partial I_e}{\partial t} \quad (3)$$

The currents I_k are found from the solution of the system of equations for the equivalent network in fig. 3.

3. RESULTS

The model presented above has been tested by analyzing the geometry of TEAM Problem 9 [6], shown in fig. 4. The results for the tube without defects were compared with results obtained from an analytical solution.

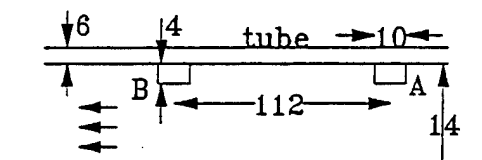


Fig. 4 Geometry of the Team problem 9

We first analyze the behaviour of results using a discretization of 150 x 3 rings, and varying the length of the tube.

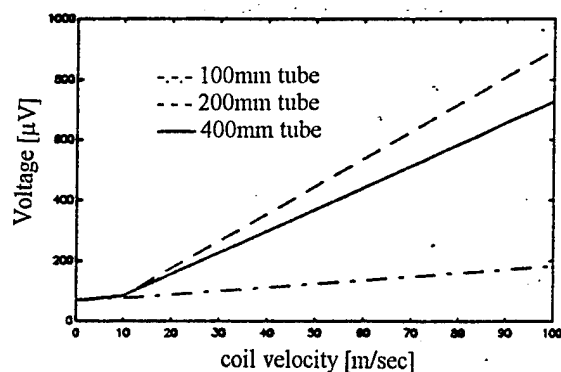


Fig. 5 Induced voltage vs. coil velocity, tube without defect

Fig. 5 shows the calculated and analytical voltage on the pick-up coil for different coil velocities and three different tube lengths. The results show that the length of the tube has

considerable influence on the correctness of the calculated data. To obtain good results, the distance between the exciting coil and the edge of the tube must be at least twice the distance between the exciting and pick-up coils. Next, we analyze the effect of discretization on the calculated data using a 400mm tube and three levels of discretization. Fig. 6 shows that the calculated results agree well with the analytical results even for a coarse discretization of 50 x 3 rings.

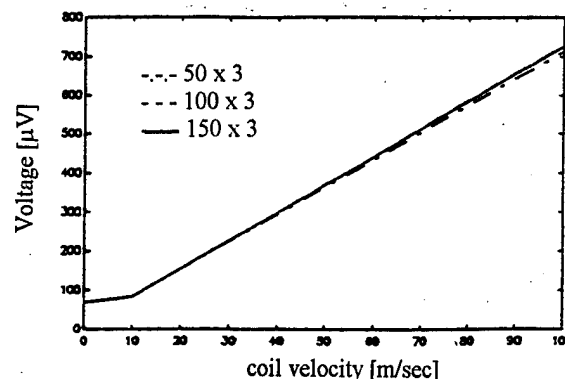


Fig. 6 Induced voltage vs. coil velocity, tube without defect

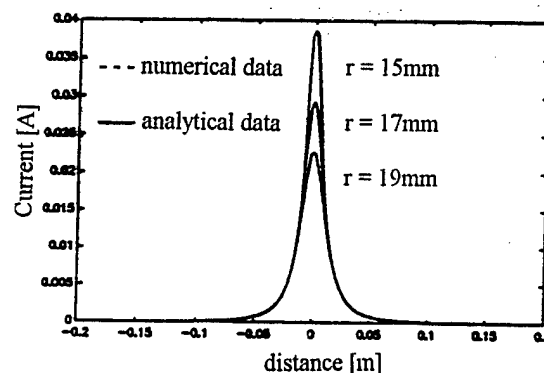


Fig. 7 Induced current modulus in the tube vs. distance from the exciting coil on three radii, for $v = 0$.

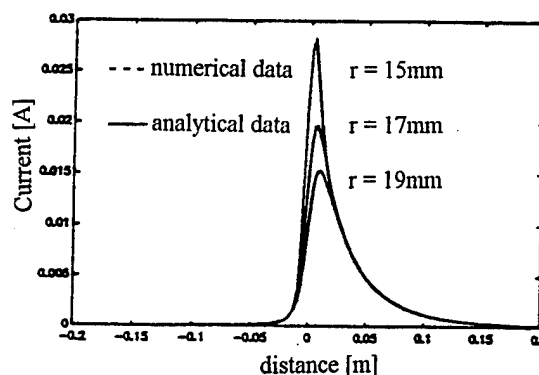


Fig. 8 Induced current modulus in the tube vs. distance from the exciting coil on three radii, for $v = 100$ m/sec.

The effects of velocity are clearly shown by comparison of the analytically and numerically calculated induced currents in the tube. Fig. 7 and 8 show the induced currents at

three different radii in the tube for $v=0$ and $v=100$ m/sec for the previous geometry and discretization level.

Next, we study the geometry shown in fig. 9 considering a conductivity $\sigma = 2 \cdot 10^9$ (S/m) and a constant relative permeability $\mu_r = 1000$, the exciting signal frequency is 50 Hz. For configurations which includes an axisymmetric defect, there is an analytical solution only for a non ferromagnetic tube [5], or for a ferromagnetic tube at zero coils velocity [7].

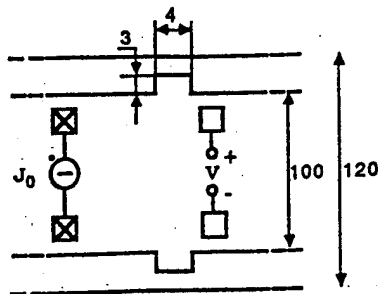


Fig. 9 RFEC geometry with an axisymmetric defects.

Fig. 10 and 11 show good agreement between the computed and analytical induced voltage and phase for a defect size of 2×4 mm and different relative positions between the defect and the coils. In the following figures distance zero means that the pick up coil is exactly under the defect.

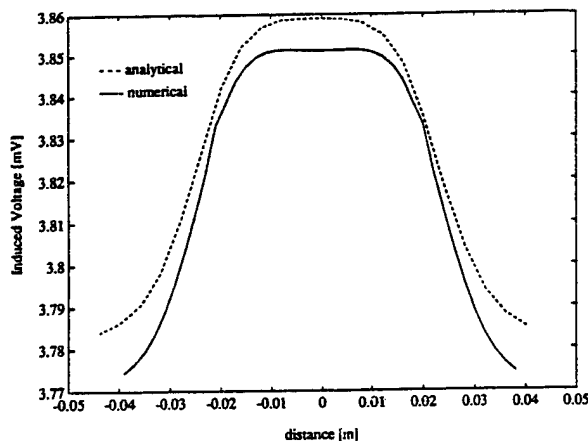


Fig. 10 Induced voltage vs coil position, tube with defect

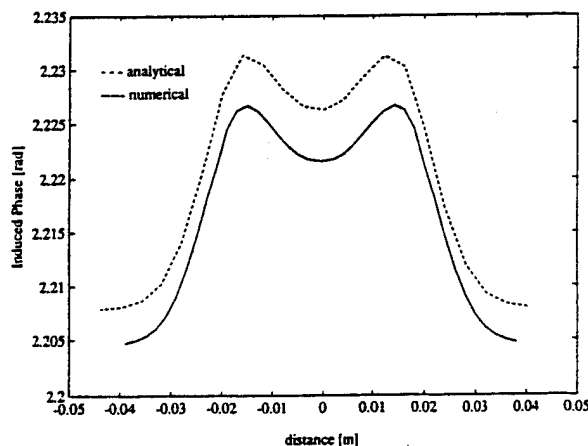


Fig. 11 Phase of the induced voltage vs. coil position, tube with defect

As a conclusion from the tests above, we observe that the characteristic "double bump" signal was only clearly detectable if the tube material has a high conductivity; copper for instance. The influence of tube length and discretization level on the results calculated for the cases shown in figures 7, 8, 10 and 11 is not shown here but these show the same trends as the results in fig. 4 and 5. The influence of the tube length is more pronounced than that due to discretization. This means that the proposed method does not require fine discretization for good results, even in presence of defects. One purpose of this method was to show that the RFEC is a direct induction effect. To do so we calculated the induced voltage for tubes with wall thickness of 7 cm. and 12 cm.

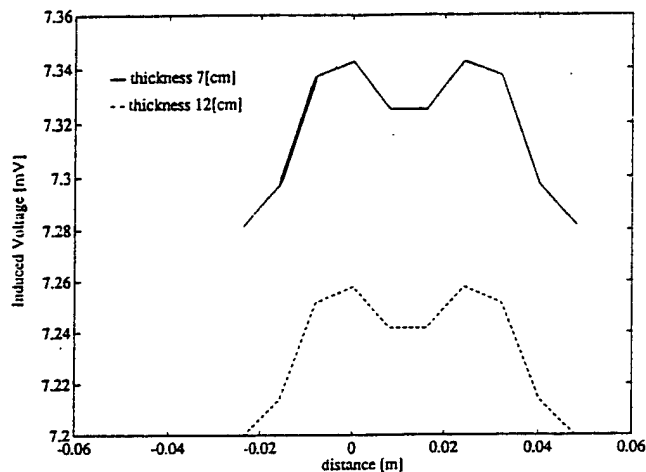


Fig. 12 Induced voltage vs coil position, thick tube with inner defect

Figure 12 shows that the induced voltage is still sensitive to the presence of an internal defect as the pick-up coil passes under the defect. In addition, the magnitude of the induced voltage is nearly equal for the two thicknesses tested, indicating that sensitivity is unrelated to wall thickness. Figures 13, and 14 show the transient induced voltage for different frequencies and probe velocity.

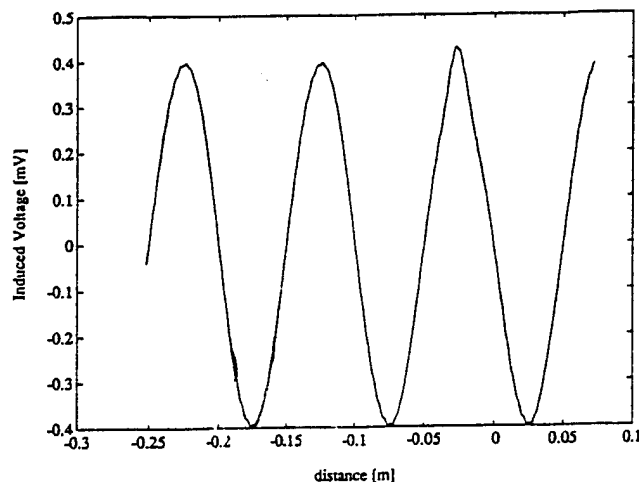


Fig. 13 Induced voltage vs. coil position, $f=50$ Hz, $v=5$ m/sec

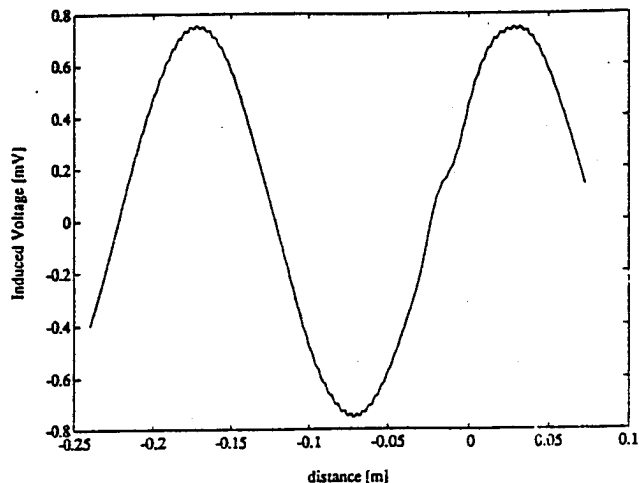


Fig. 14 Induced voltage vs. coil position, $f=50$ Hz, $v=10$ m/sec

The induced voltage has a typical transient behaviour, even for the lower velocities considered here. This behaviour cannot be related to steady state parameters. Furthermore, there is also a dependence between coil velocity and excitation frequency and detectability of the defect. In fact, at a frequency of 50 Hz, and a velocity of 10 m/sec, the pick-up signal is distorted, as shown in fig. 12, while at a velocity 5 m/sec the amplitude variation is clearer, and the defect can be discerned. Therefore, the conclusion is that there must be a high frequency/velocity ratio for clear defect detection. This is also pointed out in the figures 15 and 16.

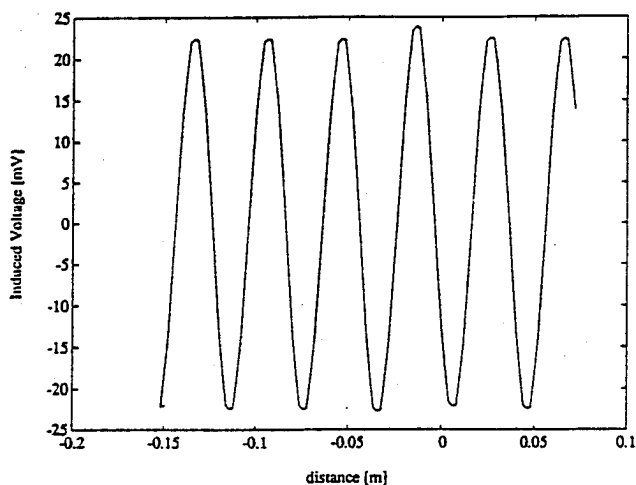


Fig. 15 Induced voltage vs. coil position, $f=785$ Hz, $v=5$ m/sec

Figure 15 shows a clearer variation of the pick-up signal in comparison with Fig. 12. This is accomplished by increasing the frequency from 50 Hz to 785 Hz. Fig. 16 shows that the sensitivity is unchanged if the frequency/velocity ratio is kept constant but with a frequency and velocity 10 times higher.

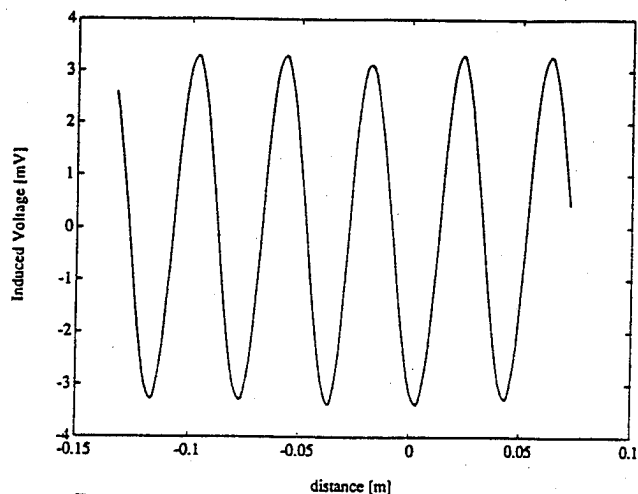


Fig. 16 Induced voltage vs. coil position, $f=7850$ Hz, $v=50$ m/sec

4.

CONCLUSIONS

The integral formulation presented here allows simple modeling of RFEC tests, including defects. Computation time is relatively short even in the presence of moving objects. The method has been validated first by comparison with analytical results. Application of the formulation for the analysis of the response of a RFEC testing apparatus has highlighted the importance of several aspects of the transient phenomena.

In particular, the output signal must be transient for complete understanding of defect detection process. Also, the importance of the relation between frequency of the exciting signal and coil velocity was pointed out.

REFERENCES

- [1] T.R.Schmidt, "The remote field eddy current inspection technique" *Materials Evaluations*, Vol. 42, no. 42, pp 225-230, 1984.
- [2] W. Lord, .S.Sun, S.S.Udpa, S.Nath, "A finite element study of the remote field eddy current phenomenon" *IEEE Trans on Mag.* Vo 24, p435, 1988
- [3] D.L.Atherton, B. Stamm, S. Sullivan, "The remote field through-wall electromagnetic inspection technique for pressure tubes" *Material Evaluation*, Vol. 44, p. 1544, 1986.
- [4] Y.S.Sun, " Finite element study of diffusion energy flow in low frequency eddy current field" *Materials Evaluations*, Vol. 47, pp 87, 1989.
- [5] N. Ida, M. Raugi, " Theoretical models for the Remote Field effect" *IEEE Trans. on Mag.* Vol 29, n. 2, March 1993.
- [6] "Problem 9 Velocity effects and low level fields in axisymmetric geometries" *Proc. of the European TEAM workshop and International Seminar on Electromagnetic field analysis*, Oxford, England, 23-25 April 1990, p323
- [7] N. Esposito, M. Raugi, A. Tellini: "A Quasi-Analytical Procedure for Magnetic Fields Analysis in Bounded Domains via Magnetization Currents" *IEEE Trans. on Mag.* Vol 31, n. 2, March 1995

LETTER FROM THE EDITOR

This issue of the *ACES Journal* marks our first venture in the area of color printing with the publication of the paper by D.D. Reuster, G.A. Thiele, and P.W. Elo. The venture also signifies the continued commitment of the Editorial Board to serve the best interests of the members of *ACES*, and the authors who have contributed significantly to the success of the *Journal*. Our Managing Editor, Dick Adler, first addressed the question of color printing in notes published in the *ACES Journal*, and *Newsletter* Vol. 9, No. 2, of 1994 on pages 178, and 86 respectively. Dick and I would appreciate feedback from readers on the question of color printing. Intending authors who have a need for color printing in their papers must contact Dick Adler for further information.

In addition to our regular panel of reviewers, we are indeed fortunate that many of our esteemed colleagues have over the years been prepared to assist the Editorial Board with the essential process of peer review. Papers submitted for publication are reviewed by at least three colleagues before any decision is made, and the authors advised of the results of this process. Accordingly it is my privilege and pleasure to thank the colleagues listed below who have over the past year or so given generously of their time, and assisted with this important activity. If I have omitted anyone, I apologize in advance for any inconvenience and/or embarrassment caused, and request that the matter be brought to my attention for correction.

B.A. Baertlein, Ohio State U., USA
L.H. Bomholt, Eidgenossische Technische Hochschule, SWITZERLAND
Q. Chen, Brown Technology Inc., CANADA
J.C. Cloete, U. of Stellenbosch, S. AFRICA
M. Gyimesi, U. of Toronto, CANADA
F.J. Harchiewicz, Southern Illinois U., USA
K.H. Joyner, Telecom Australia Research Labs., AUSTRALIA
Y. Leviatan, Technion-Israel, Inst. of Technology, ISRAEL
F.J.C. Meyer, U. of Stellenbosch, S. AFRICA
K.D. Paulsen, Dartmouth College, USA
C.E. Smith, U. of Mississippi, USA
E. Tomer, Applied Mathematics and Computing, USA
H. Tsuboi, Fukuyama U., JAPAN
E.T. van Deventer, U. of Toronto, CANADA
F.E. Vermeulen, U. of Alberta, CANADA
D.H. Werner, Pennsylvania State U., USA
Jo-Yu Wu, Ohio State U., USA

Lastly, I again thank all the authors who have contributed to the success of the *ACES Journal*.

Respectfully yours,
Duncan Baker

1996 INSTITUTIONAL MEMBERS

THE AEROSPACE CORPORATION
PO Box 92957
Los Angeles, CA 90009-2957

ANDREW CANADA INC.
606 Beech Street
Whitby, ON, CANADA L1N 5S2

ANDREW CORPORATION
10500 W. 153rd Street
Orland Park, IL 60462

ATEA
Raleigh Road, Private Bag 12
Ascot Vale, VIC, AUSTRALIA 3032

ATOMIC WEAPONS ESTAB. UK
Bldg. E3, Awe Aldermaston
Reading, BERKS, UK RG7 4PR

BRITISH AEROSPACE
Wharton Aerodrome, Nr. Wharton
Preston, LANCS. UK PR4 1AX

BRITISH AEROSPACE
FPC 267 PO Box 5
Filton, BRISTOL, UK BS12 7QW

BRITISH BROADCASTING CO.
Kingswood Warren
Tadworth, SURREY, UK KT20 6NP

CAMBRIDGE CONSULTANTS LTD
Milton Road, Science Park
Cambridge, CAMBS, UK CB5 4DW

CHALMERS UNIV OF TECHNOLOGY
Dept. of Microwave Technology
Gothenburg, SWEDEN S 412 96

CSC PROFESSIONAL SERVICES GP.
10101 Senate Drive
Lanham, MD 20706-4368

CSELT
Via Guglielmo Reiss Romoli 274
Turin, ITALY 10148

CSIRO, CENTER FOR ADV. TECH.
PO Box 883
Kenmore, QLD, AUSTRALIA 4069

CUBIC COMMUNICATIONS INC.
PO Box 85587
San Diego, CA 92186-5587

CULHAM LAB
UK Atomic Energy Authority
Abingdon, OXFORD, UK OX14 3DB

D.L.R. OBERPFAFFENHOFEN
Zentralbibliothek
Wessling, OBB, GERMANY 8031

DEFENCE TECH & PROCUREMENT
Nemp Lab - AC Zentrum
Spiez, SWITZERLAND CH 3700

DEFENSE RESEARCH ESTAB. LIB.
3701 Carling Avenue
Ottawa, ON, CANADA K1A 0Z4

DERA INFORMATION CENTRE
Q4 Building
Hants, UK GU14 6TD

DSTO LIBRARY
Box 1500
Salisbury, SA, AUSTRALIA 5108

DYNETICS, INC.
PO Box B
Huntsville, AL 35814-5050

ELECTRICAL COMM. LAB/LIBRARY
1 2356 Take Yokosuka Shi
Kanagawa, KEN, MZ, JAPAN 238

ERICSSON RADAR ELEC/ANT SYS.
Bergfotsgatan 2
Molndal, SWEDEN S-43184

ESCUELA TRANSMISIONES
EJERCITO DEL AIRE
Ctr. Extremadura, Km 10, 200
Madrid, SPAIN 28024

FANFIELD LTD.
Braxted Park
Witham, ESSEX, UK CM8 3XB

FELDBERG LIBRARY
Dartmouth College
Hanover, NH 03755

FGAN/FHP
Neuenahr Strasse 20
Wachtberg-Werthoven, GERMANY
53343

FOKKER AIRCRAFT B.V.
PO Box 7600
Schiphol, THE NETHERLANDS 1117 ZJ

GEC MARCONI RESEARCH CTR, LIB.
W. Hanningfield Road
Gt. Baddow, CHLMSFRD, UK CM2 8HN

HKUST LIBRARY
Clear Water Bay Road
Kowloon, HONG KONG

HOKKAIDO DAIGAKU
Nishi 8, Kita 13
Sapporo, JAPAN 060

HUGHES RESEARCH LIBRARY
3011 Malibu Canyon Road
Malibu, CA 90265-4737

HUNTING ENGINEERING LTD
Reddings Wood, Ampthill
Bedford, UK MK45 2HD

IABG
Einsteinstrasse 20
Ottobrunn, GERMANY D-85521

IIT RESEARCH INSTITUTE
185 Admiral Cochrane Drive
Annapolis, MD 21401-7396

IMAGINEERING LIMITED
95 Barber Greene Road, Suite. 112
Toronto, ON, CANADA M3C 3E9

IPS RADIO & SPACE SVC., LIBRARY
PO Box 5606
W. Chatswood, NSW, AUSTRALIA 2057

KATHREIN-WERKE KG
Postbox 100 444
Rosenheim, GERMANY D-83004

KERSHNER, WRIGHT & HAGAMAN
5730 Gen. Washington Drive
Alexandria, VA 22312

LIBRARY, IREQ
1800 Montee Ste.- Julie
Varenes, QC, CANADA J3X 1S1

LINDA HALL LIBRARY
5109 Cherry Street
Kansas City, MO 64110-2498

MATRA DEFENSE
37 Av. Louis Breguet BP 1
Velizy, Cedex, FRANCE 78590

MISSISSIPPI STATE UNIV LIBRARY
PO Box 9570
Mississippi State, MS 39762

MITRE CORPORATION LIBRARY
202 Burlington Road
Bedford, MA 01730-1407

MONASH UNIVERSITY
900 Dandenong Road, Caulfield East
Melbourne, VIC, AUSTRALIA 3145

MOTOROLA CSGR
600 N. US Hwy 45
Libertyville, IL 60048

MPB TECHNOLOGIES INC.
151 Hymus Blvd.
Pointe-Claire, QC, CANADA H9R 1E9

NATIONAL AEROSPACE LAB, LIB.
Anthony Fokkerweg 2, PO Box 153
Emmeloord,
THE NETHERLANDS CM 1059

NATIONAL RADIOLOGICAL PROT. BD.
Chilton
Didcot, OXON, UK OX11 0RQ

NAVITALIA
5301 Wisconsin Avenue, N.W.
Washington, DC 20015

NIKSAR
35/45 Gilbey Road
Mt. Waverley, VIC, AUSTRALIA 3149

NORTEL TECHNOLOGY
London Road
Harlow, ESSEX, UK CM17 9NA

OXFORD INSTRUMENTS PLC
Osney Mead
Oxford, OXON, UK OX2 ODX

PARAGON TECHNOLOGY, INC
200 Innovation Blvd., Suite 240
State College, PA 16803

PENN STATE UNIVERSITY
Pattee Library
University Park, PA 16802

QUEEN MARY & WESTFIELD COLL.
Mile End Road
London, UK E14NS

RADIO FREQUENCY SYSTEMS. PL
36 Garden Street
Kilsyth, VIC, AUSTRALIA 3137

RADIO FREQUENCY SYSTEMS, PL
12 Waddikee Road
Lonsdale, SA, AUSTRALIA 5600

RES. INST. OF IND. SCIENCE LIB.
17 Haengdang-Dong
Sungdong-Ku, SEOUL,
S. KOREA 133-791

ROCKWELL INTL.
1745 Jefferson Davis Hwy. Suite 1107
Arlington, VA 22202

ROCKWELL/COLLINS AVIONIC
350 Collins Road, N.E.
Cedar Rapids, IA 52498

ROYAL MILIT COLL OF SCIENCE
Cranfield University
Swindon, WILTS, UK SN6 8LA

SAAB-SCANIA AB
Saab Military Aircraft
Linköping, SWEDEN S-58188

SERCO SERVICES
Cheeseman's Lane
Hambrook, W. SUSSEX, UK PO18 8U

SYRACUSE RESEARCH CORP.
Merrill Lane
Syracuse, NY 13210-4080

TASC-LIBRARY
55 Walkers Brook Drive
Reading, MA 01867-3297

TECHNION
PO Box 830701
Birmingham, AL 35283

TECHNISCHE UNIVERSITEIT DELFT
Mekelweg 4
Delft, HOLLAND
THE NETHERLANDS 2628 CD

TELEBRAS - CPQD LIBRARY
CP 1579
Campinas, SP, BRAZIL 13088-061

TELSTRA, LIBRARY
Private Bag 37, 770 Blackburn Road
Clayton, VIC, AUSTRALIA 3168

UNIV OF CENTRAL FLORIDA LIB.
PO Box 162440
Orlando, FL 32816-2440

UNIV OF MISSOURI-ROLLA LIB.
Periodicals
Rolla, MO 65401

UNIVERSITY OF SURREY
Center for Satellite Research
Guildford, SURREY, UK GU2 5XH

UNIV. DER BUNDESWEHR MÜNCHEN
Werner Heisenberg Weg 39
Neubiberg, GERMANY D-85577

US COAST GUARD ACADEMY
15 Mohegan Avenue
New London, CT 06320-4195

VISTA RESEARCH INC.
PO Box 998
Mountain View, CA 94042

VIT, TECH RESEARCH CENTER
PO Box 1202
Espoo, FINLAND FIN-02044

WATKINS-JOHNSON CO. LIB.
700 Quince Orchard Road
Gaithersburg, MD 20878-1794

YORK ELECTRONICS CENTRE
University of York
Heslington, YORK, UK YO1 5DD

ACES COPYRIGHT FORM

This form is intended for original, previously unpublished manuscripts submitted to ACES periodicals and conference publications. The signed form, appropriately completed, MUST ACCOMPANY any paper in order to be published by ACES. PLEASE READ REVERSE SIDE OF THIS FORM FOR FURTHER DETAILS.

TITLE OF PAPER:

AUTHORS(S)

PUBLICATION TITLE/DATE:

RETURN FORM TO:

Dr. Richard W. Adler
Naval Postgraduate School
Code EC/AB
833 Dyer Road, Room 437
Monterey, CA 93943-5121 USA

PART A - COPYRIGHT TRANSFER FORM

(NOTE: Company or other forms may not be substituted for this form. U.S. Government employees whose work is not subject to copyright may so certify by signing Part B below. Authors whose work is subject to Crown Copyright may sign Part C overleaf).

The undersigned, desiring to publish the above paper in a publication of ACES, hereby transfer their copyrights in the above paper to The Applied Computational Electromagnetics Society (ACES). The undersigned hereby represents and warrants that the paper is original and that he/she is the author of the paper or otherwise has the power and authority to make and execute this assignment.

Returned Rights: In return for these rights, ACES hereby grants to the above authors, and the employers for whom the work was performed, royalty-free permission to:

1. Retain all proprietary rights other than copyright, such as patent rights.
2. Reuse all or portions of the above paper in other works.
3. Reproduce, or have reproduced, the above paper for the author's personal use or for internal company use provided that (a) the source and ACES copyright are indicated, (b) the copies are not used in a way that implies ACES endorsement of a product or service of an employer, and (c) the copies per se are not offered for sale.
4. Make limited distribution of all or portions of the above paper prior to publication.
5. In the case of work performed under U.S. Government contract, ACES grants the U.S. Government royalty-free permission to reproduce all or portions of the above paper, and to authorize others to do so, for U.S. Government purposes only.

ACES Obligations: In exercising its rights under copyright, ACES will make all reasonable efforts to act in the interests of the authors and employers as well as in its own interest. In particular, ACES REQUIRES that:

1. The consent of the first-named author be sought as a condition in granting re-publication permission to others.
2. The consent of the undersigned employer be obtained as a condition in granting permission to others to reuse all or portions of the paper for promotion or marketing purposes.

In the event the above paper is not accepted and published by ACES or is withdrawn by the author(s) before acceptance by ACES, this agreement becomes null and void.

AUTHORIZED SIGNATURE

TITLE (IF NOT AUTHOR)

EMPLOYER FOR WHOM WORK WAS PERFORMED

DATE FORM SIGNED

PART B - U.S. GOVERNMENT EMPLOYEE CERTIFICATION

(NOTE: If your work was performed under Government contract but you are not a Government employee, sign transfer form above and see item 5 under Returned Rights).

This certifies that all authors of the above paper are employees of the U.S. Government and performed this work as part of their employment and that the paper is therefore not subject to U.S. copyright protection.

AUTHORIZED SIGNATURE

TITLE (IF NOT AUTHOR)

NAME OF GOVERNMENT ORGANIZATION

DATE FORM SIGNED

PART C - CROWN COPYRIGHT

(Note: ACES recognizes and will honor Crown Copyright as it does U.S. Copyright. It is understood that, in asserting Crown Copyright, ACES in no way diminishes its rights as publisher. Sign only if ALL authors are subject to Crown Copyright.

This certifies that all authors of the above Paper are subject to Crown Copyright. (Appropriate documentation and instructions regarding form of Crown Copyright notice may be attached).

AUTHORIZED SIGNATURE

TITLE OF SIGNED

NAME OF GOVERNMENT BRANCH

DATE FORM SIGNED

Information to Authors

ACES POLICY

ACES distributes its technical publications throughout the world, and it may be necessary to translate and abstract its publications, and articles contained therein, for inclusion in various compendiums and similar publications, etc. When an article is submitted for publication by ACES, acceptance of the article implies that ACES has the rights to do all of the things it normally does with such an article.

In connection with its publishing activities, it is the policy of ACES to own the copyrights in its technical publications, and to the contributions contained therein, in order to protect the interests of ACES, its authors and their employers, and at the same time to facilitate the appropriate re-use of this material by others.

The new United States copyright law requires that the transfer of copyrights in each contribution from the author to ACES be confirmed in writing. It is therefore necessary that you execute either Part A-Copyright Transfer Form or Part B-U.S. Government Employee Certification or Part C-Crown Copyright on this sheet and return it to the Managing Editor (or person who supplied this sheet) as promptly as possible.

CLEARANCE OF PAPERS

ACES must of necessity assume that materials presented at its meetings or submitted to its publications is properly available for general dissemination to the audiences these activities are organized to serve. It is the responsibility of the authors, not ACES, to determine whether disclosure of their material requires the prior consent of other parties and if so, to obtain it. Furthermore, ACES must assume that, if an author uses within his/her article previously published and/or copyrighted material that permission has been obtained for such use and that any required credit lines, copyright notices, etc. are duly noted.

AUTHOR/COMPANY RIGHTS

If you are employed and you prepared your paper as a part of your job, the rights to your paper initially rest with your employer. In that case, when you sign the copyright form, we assume you are authorized to do so by your employer and that your employer has consented to all of the terms and conditions of this form. If not, it should be signed by someone so authorized.

NOTE RE RETURNED RIGHTS: Just as ACES now requires a signed copyright transfer form in order to do "business as usual", it is the intent of this form to return rights to the author and employer so that they too may do "business as usual". If further clarification is required, please contact: The Managing Editor, R.W. Adler, Naval Postgraduate School, Code EC/AB, Monterey, CA, 93943, USA (408)656-2352.

Please note that, although authors are permitted to re-use all or portions of their ACES copyrighted material in other works, this does not include granting third party requests for reprinting, republishing, or other types of re-use.

JOINT AUTHORSHIP

For jointly authored papers, only one signature is required, but we assume all authors have been advised and have consented to the terms of this form.

U.S. GOVERNMENT EMPLOYEES

Authors who are U.S. Government employees are not required to sign the Copyright Transfer Form (Part A), but any co-authors outside the Government are.

Part B of the form is to be used instead of Part A only if all authors are U.S. Government employees and prepared the paper as part of their job.

NOTE RE GOVERNMENT CONTRACT WORK: Authors whose work was performed under a U.S. Government contract but who are not Government employees are required to sign Part A-Copyright Transfer Form. However, item 5 of the form returns reproduction rights to the U.S. Government when required, even though ACES copyright policy is in effect with respect to the reuse of material by the general public.

July 1996

ACES MEMBERSHIP - NEWSLETTER & JOURNAL SUBSCRIPTION FORM

please print

MIDDLE INITIAL

DEPARTMENT/MAIL STATION

PLEASE LIST THE ADDRESS YOU WANT USED FOR PUBLICATIONS

MAILING ADDRESS**ZIP/POSTAL CODE****AMATEUR RADIO CALL SIGN**

NO

NO

CURRENT SUBSCRIPTION PRICES

AREA	INDIVIDUAL SURFACE MAIL	INDIVIDUAL AIRMAIL	ORGANIZATIONAL (AIRMAIL ONLY)
U.S. & CANADA	() \$ 65	() \$ 65	() \$115
MEXICO, CENTRAL & SOUTH AMERICA	() \$ 68	() \$ 70	() \$115
EUROPE, FORMER USSR TURKEY, SCANDINAVIA	() \$ 68	() \$ 78	() \$115
ASIA, AFRICA, MIDDLE EAST & PACIFIC RIM	() \$ 68	() \$ 85	() \$115

FULL-TIME STUDENT RATE IS \$25 FOR ALL COUNTRIES

***THIS SECTION IS TO BE USED ONLY IF PAYING BY CREDIT CARD & CARD IS NOT YOUR OWN.
IT IS NOW MANDATORY THAT THE CARD HOLDER PRINTS AND SIGN HIS/HER NAME AND
LIST HIS/HER COMPLETE ADDRESS***

SIGNATURE OF CARD HOLDER

MAILING ADDRESS

MAILING ADDRESS(cont)

☐ A bank check for the total amount is enclosed.⁽¹⁾

☐ Traveler's checks for the total amount are enclosed.⁽²⁾

☐ International Money Order is enclosed.⁽³⁾

☐ Charge to: ☐ MasterCard ☐ Visa. ☐ Discover ☐ Amex.⁽⁴⁾

[illegible]

Mo. _____ Year _____

**MAKE PAYABLE TO "ACES" and send to: RICHARD W. ADLER, EXEC. OFFICER,
NAVAL POSTGRADUATE SCHOOL, ECE DEPT., CODE EC/AB, 833 DYER ROAD, ROOM 437, MONTEREY, CA 93943-5121**

Non-USA participants may remit via (1) **Bank Checks**, if (a) drawn on a U.S. Bank, (b) have bank address, (c) contain series of (9) digit mandatory routing numbers; (2) **Traveler's Checks** (in U.S. \$\$); (3) **International Money Order** drawn in U.S. funds, payable in U.S.; (4) **Credit Cards**: Visa, Master Card, Discover Card, Amex.

Total Remittance (U.S. Dollars Only) \$

July 1996

ADVERTISING RATES		
	FEE	PRINTED SIZE
Full page	\$200.	7.5" x 10.0"
1/2 page	\$100.	7.5" x 4.7" or 3.5" x 10.0"
1/4 page	\$ 50	3.5" x 4.7"
<p>All ads must be camera ready copy.</p> <p>Ad deadlines are same as Newsletter copy deadlines.</p> <p>Place ads with Ray Perez, Newsletter Editor, Martin Marietta Astronautics, MS 58700, PO Box 179, Denver, CO 80201, USA. The editor reserves the right to reject ads.</p>		

ACES NEWSLETTER AND JOURNAL COPY INFORMATION	
<u>Issue</u>	<u>Copy Deadline</u>
March	January 13
July	May 25
November	September 25

APPLIED COMPUTATIONAL ELECTROMAGNETICS SOCIETY JOURNAL

INFORMATION FOR AUTHORS

PUBLICATION CRITERIA

Each paper is required to manifest some relation to applied computational electromagnetics. **Papers may address general issues in applied computational electromagnetics, or they may focus on specific applications, techniques, codes, or computational issues.** While the following list is not exhaustive, each paper will generally relate to at least one of these areas:

1. Code validation. This is done using internal checks or experimental, analytical or other computational data. Measured data of potential utility to code validation efforts will also be considered for publication.

2. Code performance analysis. This usually involves identification of numerical accuracy or other limitations, solution convergence, numerical and physical modeling error, and parameter tradeoffs. However, it is also permissible to address issues such as ease-of-use, set-up time, run time, special outputs, or other special features.

3. Computational studies of basic physics. This involves using a code, algorithm, or computational technique to simulate reality in such a way that better or new physical insight or understanding is achieved.

4. New computational techniques, or new applications for existing computational techniques or codes.

5. "Tricks of the trade" in selecting and applying codes and techniques.

6. New codes, algorithms, code enhancement, and code fixes. This category is self-explanatory but includes significant changes to existing codes, such as applicability extensions, algorithm optimization, problem correction, limitation removal, or other performance improvement. **Note: Code (or algorithm) capability descriptions are not acceptable, unless they contain sufficient technical material to justify consideration.**

7. Code input/output issues. This normally involves innovations in input (such as input geometry standardization, automatic mesh generation, or computer-aided design) or in output (whether it be tabular, graphical, statistical, Fourier-transformed, or otherwise signal-processed). Material dealing with input/output database management, output interpretation, or other input/output issues will also be considered for publication.

8. Computer hardware issues. This is the category for analysis of hardware capabilities and limitations in meeting

various types of electromagnetics computational requirements. Vector and parallel computational techniques and implementation are of particular interest.

Applications of interest include, but are not limited to, antennas (and their electromagnetic environments), networks, static fields, radar cross section, shielding, radiation hazards, biological effects, electromagnetic pulse (EMP), electromagnetic interference (EMI), electromagnetic compatibility (EMC), power transmission, charge transport, dielectric and magnetic materials, microwave components, MMIC technology, remote sensing and geophysics, communications systems, fiber optics, plasmas, particle accelerators, generators and motors, electromagnetic wave propagation, non-destructive evaluation, eddy currents, and inverse scattering.

Techniques of interest include frequency-domain and time-domain techniques, integral equation and differential equation techniques, diffraction theories, physical optics, moment methods, finite differences and finite element techniques, modal expansions, perturbation methods, and hybrid methods. This list is not exhaustive.

A unique feature of the Journal is the publication of unsuccessful efforts in applied computational electromagnetics. Publication of such material provides a means to discuss problem areas in electromagnetic modeling. Material representing an unsuccessful application or negative results in computational electromagnetics will be considered for publication only if a reasonable expectation of success (and a reasonable effort) are reflected. Moreover, such material must represent a problem area of potential interest to the ACES membership.

Where possible and appropriate, authors are required to provide statements of quantitative accuracy for measured and/or computed data. This issue is discussed in "Accuracy & Publication: Requiring quantitative accuracy statements to accompany data", by E.K. Miller, *ACES Newsletter*, Vol. 9, No. 3, pp. 23-29, 1994, ISBN 1056-9170.

EDITORIAL REVIEW

In order to ensure an appropriate level of quality control, papers are refereed. They are reviewed both for technical correctness and for adherence to the listed guidelines regarding information content. Authors should submit the initial manuscript in draft form so that any suggested changes can be made before the photo-ready copy is prepared for publication.

APPLIED COMPUTATIONAL ELECTROMAGNETICS SOCIETY JOURNAL

INFORMATION FOR AUTHORS

STYLE FOR CAMERA READY COPY

The ACES Journal is flexible, within reason, in regard to style. However, certain requirements are in effect:

1. The paper title should NOT be placed on a separate page. The title, author(s), abstract, and (space permitting) beginning of the paper itself should all be on the first page. The title, author(s), and author affiliations should be centered (center-justified) on the first page.

2. An abstract is REQUIRED. The abstract should state the computer codes, computational techniques, and applications discussed in the paper (as applicable) and should otherwise be usable by technical abstracting and indexing services.

3. Either British English or American English spellings may be used, provided that each word is spelled consistently throughout the paper.

4. Any commonly-accepted format for referencing is permitted, provided that internal consistency of format is maintained. As a guideline for authors who have no other preference, we recommend that references be given by author(s) name and year in the body of the paper (with alphabetical listing of all references at the end of the paper). Titles of Journals, monographs, and similar publications should be in boldface or italic font or should be underlined. Titles of papers or articles should be in quotation marks.

5. Internal consistency shall also be maintained for other elements of style, such as equation numbering. As a guideline for authors who have no other preference, we suggest that equation numbers be placed in parentheses at the right column margin.

6. The intent and meaning of all text must be clear. For authors who are NOT masters of the English language, the ACES Editorial Staff will provide assistance with grammar (subject to clarity of intent and meaning).

7. Unused space should be minimized. Sections and subsections should not normally begin on a new page.

MATERIAL, SUBMITTAL FORMAT AND PROCEDURE

The preferred format for submission and subsequent review, is 12 point font or 12 cpi, double line spacing and single column per page. Four copies of all submissions should be sent to the Editor-in-Chief. Each submission must be accompanied by a covering letter. The letter should include the name, address, and telephone and/or fax number and/or e-mail address of at least one of the authors.

Only camera-ready original copies are accepted for publication. The term "camera-ready" means that the material is neat, legible, and reproducible. The preferred font style is Times Roman 10 point (or equivalent) such as that used in this text. A double column format similar to that used here is preferred. **No author's work will be turned down once it has been accepted because of an inability to meet the requirements concerning fonts and format.** Full details are sent to the author(s) with the letter of acceptance.

There is NO requirement for India ink or for special paper; any plain white paper may be used. However, faded lines on figures and white streaks along fold lines should be avoided. Original figures - even paste-ups - are preferred over "nth-generation" photocopies. These original figures will be returned if you so request.

While ACES reserves the right to re-type any submitted material, this is not generally done.

PUBLICATION CHARGES

ACES members are allowed 12 pages per paper without charge; non-members are allowed 8 pages per paper without charge. Mandatory page charges of \$75 a page apply to all pages in excess of 12 for members or 8 for non-members. Voluntary page charges are requested for the free (12 or 8) pages, but are NOT mandatory or required for publication. A priority courtesy guideline, which favors members, applies to paper backlogs. Full details are available from the Editor-in-Chief.

COPYRIGHTS AND RELEASES

Each primary author must sign a copyright form and obtain a release from his/her organization vesting the copyright with ACES. Forms will be provided by ACES. Both the author and his/her organization are allowed to use the copyrighted material freely for their own private purposes.

Permission is granted to quote short passages and reproduce figures and tables from an ACES Journal issue provided the source is cited. Copies of ACES Journal articles may be made in accordance with usage permitted by Sections 107 or 108 of the U.S. Copyright Law. This consent does not extend to other kinds of copying, such as for general distribution, for advertising or promotional purposes, for creating new collective works, or for resale. The reproduction of multiple copies and the use of articles or extracts for commercial purposes require the consent of the author and specific permission from ACES. Institutional members are allowed to copy any ACES Journal issue for their internal distribution only.